NTNU – Trondheim
Norwegian University of
Science and Technology

NANOMECHANICAL TESTING OF DIATOMS

Sindre Hove Bjørnøy

Nanotechnology
Submission date: June 2012
Supervisor: Christian Thaulow, IPM

Norwegian University of Science and Technology
Department of Engineering Design and Materials

Preface

Mechanical testing of samples with geometries in the micro- and nanometer range are becoming increasingly popular in the scientific community. The combination of focused ion beam-instruments (FIB), used to create test specimens at a small scale, and stress induced by nanoindenters or atomic force microscopes (AFM) serve as a powerful platform for investigating the properties of materials at the micro- an nanoscale. A large part of this project work has been to gain knowledge about and experience with such equipment. The FIB-nanoindenter technique has in this project been brought into the complex world of diatoms, where perfect spheres and straight lines do not exist, in spite of beautiful three dimensional patterns resembling man-made structures. Nature is bursting with interesting composite materials and advanced geometries just waiting to be discovered by scientists. The complexity of such structures make them inherently hard to analyze, but with the aid of computational models the secrets of nature are slowly being unraveled.

I would like to thank PhD candidates Bjørn Rune Søråas Rogne and Adina Basa for a lot of help with the nanoindenter and for always answering my questions when I came knocking on their door.

The researchers at Solbiopta have been a great help when it comes to the diatoms and answered many questions. A special thanks to Dr. Matilde Chauton for providing the pre-cleaned *Coscinodiscus* sp. samples and Dr. Julien Romann for his advice and interesting inputs on my work.

In my lack of knowledge about modeling and simulations, I am grateful for the inspiring and educational conversations with Markus Buehler and Leon Dimas at the Center for Computational Engineering at MiT, and to my fellow master student Are Moa Gausen for creating the FEM-models of the diatoms.

A large thanks also goes to my supervisor Christian Thaulow for encouraging conversations and his confidence in success.

Finally thanks to Julie for enduring my ramblings of algae and ions.

Trondheim, June 2012. Sindre H. Bjørnøy

THE NORWEGIAN UNIVERSITY
OF SCIENCE AND TECHNOLOGY
DEPARTMENT OF ENGINEERING DESIGN
AND MATERIALS

MASTER THESIS SPRING 2012
FOR
STUD.TECHN. SINDRE HOVE BJØRNØY

NANOMECHANICAL TESTING OF DIATOMS
Nanomekanisk prøving av diatoms

Almost anywhere in nature, from flower surfaces and insect feet to structural components like bone and spider silk, nanostructures and hierarchical design emerges when they are examined closely.The similarity found everywhere in nature suggest that a universal principle lies behind, and that hierarchical design is a viable method to design structures. Biomimetics is a field of science which these materials are studied and imitated. With the help of advanced electron- and probing microscopes in combination with ever-growing computer power, the secrets of nature are slowly revealed. Modeling of advanced biomaterials like spider silk and nacre has been done and the results have been compared with experiments. Hierarchical structures are also found in the amorphous silica shell, the frustule, created by a series of plankton species known as diatoms. The frustule consist of several porous layers made from silica nanoparticles.

Diatoms have, in combination with sea-sponges, acted as inspiration for atomistic models. But in spite of increased interest there are rather few experimental data for the mechanical properties of diatom frustules. The Master Thesis builds upon the experiences gained during the project work, and includes the following tasks:

AFM-study. The frustules should be characterized with an AFM in order to get more accurate measures of the surface of the different layers, and also measure the size of silica-particles.

Further development of the test scheme. In the project work, a simple and straightforward method of cutting beams in diatom frustule and subsequently bending them in a nanoindenter was tested. Nanoindentation on the different frustule parts should be performed in order to obtain hardness and stiffness values for the different layers. From this the reduced E-modulus can be calculated and in turn be compared with literature values, both theoretical and experimental values. Further improvement on this method is needed since it seems very difficult to extract any quantitative values from this test scheme. It has been experienced that the frustule is not stiff enough to give good bending test results. In order to overcome the problem with valve-response a different test-method is proposed to be investigated. With the use of the gas injection system and a micro-manipulator it should be possible to cut the beams completely out from the frustule and transfer them to a test rig made from a much stiffer material. A micro-manipulator such as the OmniprobeTM, which is available in the FIB, can

be brought down to the beam and "welded" with platinum by use of the gas injector system. The beam can then be cut free from the frustule and moved and fastened to a pre-fabricated mound. The beam can then be tested in a nanoindenter. This method of testing would eliminate the frustule response from the test results and avoid problems with different curvature. If this test scheme is deemed functional it might also be possible to perform toughness measurements on samples with pre-cracks.

Larger test specimens. Testing on larger specimens should be performed in order to capture the effects of the hierarchical structure. The small specimens used in the project work are sensitive to local differences in the porous structure. Larger test specimens will have a better averaging of the porosity and the areola layer will be better tested then what has been performed here.

Smaller test specimens. Testing of the cribellum layer was difficult to perform with the nanoindenter equipment. The smallest tip available for the testing done here was 0.6 µm. The wall-size of the cribellum layer is in the 40-70 nm range. Nanoindenting or bending tests performed with an AFM-tip might prove a more useful technique for this layer and provide information which was not obtainable under the described test scheme.

Solbiopta. The close cooperation with the research project Solbiopta shall continue. When a reliable testing method is established, candidates to be tested should be selected in close cooperation with the project.

Modeling. The cooperation with MIT on comparing the test results from this Master Thesis with atomistic modeling results from MIT shall be investigated. The limitations in a 1:1 comparison shall be examined and discussed

The thesis should include the signed problem text, and be written as a research report with summary both in English and Norwegian, conclusion, literature references, table of contents, etc. During preparation of the text, the candidate should make efforts to create a well arranged and well written report. To ease the evaluation of the thesis, it is important to cross-reference text, tables and figures. For evaluation of the work a thorough discussion of results is appreciated.

Three weeks after start of the thesis work, an A3 sheet illustrating the work is to be handed in. A template for this presentation is available on the IPM's web site under the menu "Undervisning". This sheet should be updated when the Master's thesis is submitted.

The thesis shall be submitted electronically via DAIM, NTNU's system for Digital Archiving and Submission of Master's thesis.

Contact persons
Bjørn Rune Sørås Rogne, NTNU
Gabriella Tranell, NTNU

Torgeir Welo
Head of Division

Christian Thaulow
Professor/Supervisor

NTNU
Norges teknisk-naturvitenskapelige universitet
Institutt for produktutvikling og materialer

Abstract

A test scheme to test micro-beams from diatom frustule has been developed. The method is capable of testing both complete beams and beams made from the individual layers of the frustule. The biosilica is shown to be a very brittle material with an average fracture stress of 336 $\pm$ 73 MPa and a flexural modulus of 5.72 $\pm$ 2.9 GPa. A comparison of the mechanical properties of the different layers has been performed and shows that the different structural parts greatly influence the overall mechanical properties. Additionally the mechanical properties of frustules that have undergone different chemical treatments have been investigated. The initial results indicate that the softer chemical treatment yields a stiffer biosilica.

The challenges of computational modeling of biosilica has been discussed and initial FEM-modeling shows that the porous structure reduces the stiffness of the overall structure. Further development of a combined experimental and computational test scheme is suggested.

In addition an AFM-study and nanoindentation tests were performed on the frustules.

Sammendrag

En testmetode for å undersøke de mekaniske egenskapene til mikro-bjelker fra diatom-frustuler har blitt utviklet. Metoden kan teste hele bjelker og bjelker laget av individuelle lag i frustule-strukturen. Biosilikaen diatomene er laget av har vist seg å være et sprøtt materiale med en gjennomsnittlig bruddstyrke på 336 ± 73 MPa og en elastisk bøyemodul på 5.72 ± 2.9 GPa. En sammenligning av de mekaniske egenskapene til de forskjellige lagene har blitt utført, og resultatene viser at de forskjellige strukturene i stor grad påvirker de samlede mekaniske egenskapene. I tillegg har de mekaniske egenskapene til frustuler som har blitt utsatt for ulike kjemiske rensemetoder blitt undersøkt. De foreløpige resultatene indikerer at den mildere kjemiske behandlingen fører til økt stivhet for biosilikaen.

Utfordringer med datamodellering av biologisk silika har blitt diskutert og innledene FEM-modeller har vist at den porøse strukturen til diatomene redusere stivheten til strukturen. Videre utvikling av testmetoden, ved hjelp av kombinert datamodellering og eksperimentell testing, er foreslått.

Det er også blitt utført en AFM-studie og nanoindenterings-tester på frustulene.

Contents

1 Introduction

Nature continues to fascinate scientists all over the world, even after thousands of years of examination. The complexity and beauty of the intricate structures found in biological systems are under constant inspection in the effort to elucidate the secrets of nature. Biomimetics is one the fields in which biosynthesized materials are studied and duplicated in laboratories. Structures such as bone, nacre, spider silk and diatom frustules are examples of hierarchically designed composites where nature uses clever design principles to make superior materials of inferior building blocks.[1, 2, 3, 4, 5]

The work described here is a further development of the test scheme which was developed in the project work.[6] The goal is to be able to test the mechanical properties of the silica shell of diatoms. Diatom is the name of a large group of unicellular algae, which gets their name from the structure of the cell wall. The diatoms makes an exoskeleton of silica which consists of two separated valves connected by one or several girdle bands, one of these valves connected to a girdle band can be seen in Figure 1. The diameter of the diatom *Coscinodiscus* sp., the diatom used in this work, is about 200-400 μm, which makes it one of the largest diatom species.

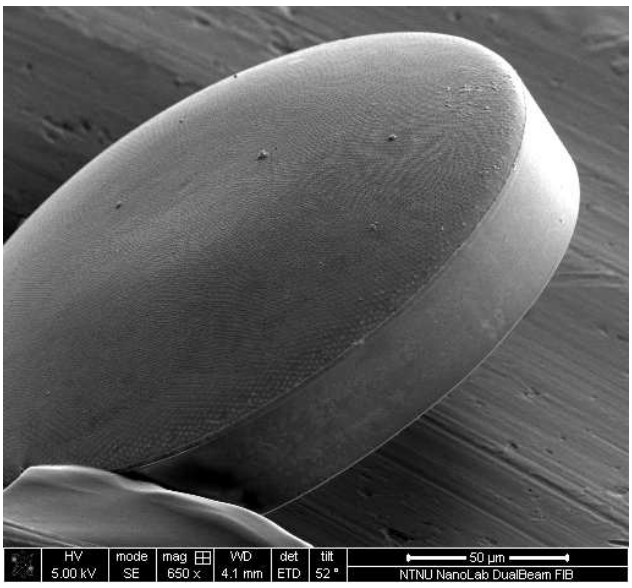

Figure 1: A low-resolution SEM-image showing a *Coscinodiscus* sp. valve and girdle band.

At NTNU, researchers in the project Solbiopta is investigating the possibility to use diatoms to increase the efficiency of solar cells.[7] As the diatoms rely on photosynthesis, the frustule has evolved not only to provide mechanical protection, but also to capture sunlight efficiently. The frustules exhibit

both light-channeling effects and anti-reflective capabilities.[8, 9] The idea is to use diatoms, or similar types of structures, as either anti-reflective coating, diffractive coating, conversion layers or as other types of optical enhancement.

The Solbiopta group has done some interesting observations of their frustule samples. They use three different cleaning procedures with increasing chemical strength. The first is a soft SDS-cleaning where a rather large amount of organic matter is left after the treatment. This is confirmed by fluorescent microscopy of the different samples. Fluorescence microscopy is a technique which can be used to detect organic matter. The frustules that have undergone this treatment are largely intact and only a small amount of broken frustules are observed when samples are inspected with an SEM. The second treatment consist of cleaning the frustules in near boiling H_2SO_4. These frustules have less signal from the fluorescent microscopy and a larger part of the frustules are broken and fractured when observed in an SEM. The final cleaning procedure involves cleaning the frustules with H_2O_2. This removes even more of the organic matter and yields almost zero signal in the fluorescent microscopy. This cleaning method leaves very few frustules intact when the samples are observed in an SEM. This is a strong indication that the mechanical properties are influenced by the organic constituents in the biosilica, as the frustules experience close to similar mechanical stress during the different cleaning methods. A more detailed description of these cleaning methods are found in Appendix C.

At MiT, Markus Buehler and his group at the Center for Computational Engineering, have also taken interest in nature's secrets, including the diatoms. With the help of atomistic simulations, they have investigated the effect that pores have on silica-structures.

Part of the work performed here is aimed to investigate the difference between the mechanical properties of frustules that have undergone the different cleaning processes, as well as to investigate the effects of geometry on the mechanical properties. The main goal is to develop a test method which is able to not only investigate the mechanical properties of diatoms, but the mechanical properties of individual parts of the diatom structure.

2 Theory

The theory section starts with an introduction of the diatom species used in this work. A short introduction to the hierarchical structure and what is known of the chemical composition is provided for the reader. Furthermore, some of the work of modeling bio-inspired silica by the group of Markus Buehler is presented. The focus is then shifted to describe the equipment used in the work. The description of the FIB can be found in the project work.[6] The following provides the reader with information about the gas-injection system and the sample transfer system which was not covered in the project work. A more thorough description of the nanoindenter system is also given. Finally, a short description of the beam theory used to analyze the experimental results is given.

2.1 *Coscinodiscus* sp.

The diatoms used in this study are the same as in the project work, the *Coscinodiscus* genus.[6] This diatom features a silica shell, called frustule, which has a hierarchical porous structure. A schematic figure and SEM-images of the structure can be seen in Figure 2. The schematic figure is taken from Losic et al.[10]

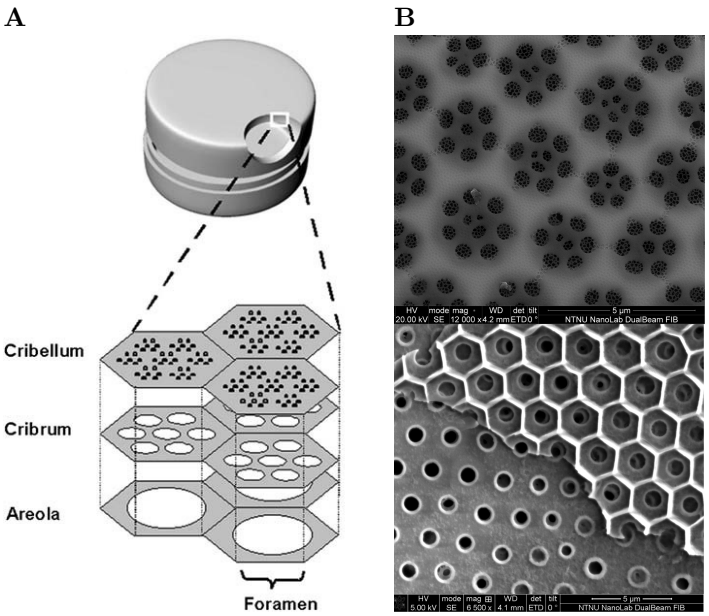

Figure 2: A schematic drawing and comparative SEM-images of the structure of the *Coscinodiscus* sp. diatom. The two top layers, cribellum and cribrum, are visible on the top SEM-image, while the areola and the foramen are visible on the bottom image.

The structure can be divided into four main structural parts. These parts are called, from the outside and in: cribellum, cribrum, areola and foramen. The cribellum is a very thin layer ($\sim$ 50 nm) with pores arranged in a hexagonal manner. The diameter of these pores are 40-60 nm. Literature suggests that this layer does not provide mechanical strength, but rather acts as a sieve to keep viruses and other harmful objects out and let nutrients in.[10, 11] The low thickness of this layer supports this theory, as well as the initial testing done in the project work, where beams made of the cribellum and cribrum layers fractured at very low loads.[6]

The cribrum layer is another thin ($\sim$200 nm) porous layer, where the pores are 200-600 nm in diameter. These pores are arranged in clusters resembling flowers. These flower-like patterns are again arranged in a hexagonal pattern. The clusters make domes connecting this layer to the areola below, a structure which is known to carry and distribute loads efficiently.

The areola is a hexagonally structure with thin walls, often described as a honeycomb-structure. The corner-to-corner distance in these hexagons are 2-3 μm and the wall thickness is about 300-400 nm. The height, or thickness, of this layer is 2-3 μm which makes it the main structural part in terms of thickness. The walls have a strikingly similar profile as an I-beam, another structural element known for its excellent load-bearing abilities.

Finally the structure is completed by a perforated plate with a thickness of 500-800 nm. The pores consists of circular holes with a diameter of 0.8-1.1 μm. These holes are also arranged in a hexagonal manner. An elevated edge, a kind of lip, surrounds the holes on both sides of this inner plate.

2.1.1 Chemical Composition

The formation of inorganic structures by living organisms is a widespread phenomenon in nature. Biomineralization, which the process is called, is found in near all classes of organism. Mammals and molluscs make bones and shells based on calcium carbonate, while the protists, including diatoms , form cell walls of silica or calcium carbonate.[12] The intricately patterned cell walls of the diatoms are made of amorphous, hydrated siliciumdioxide, termed silica. According to the literature, the silica in diatom frustules are produced inside the cell in a specialized vesicle called the silica deposition vesicle (SDV). During cell division, an SDV is formed in each of the two valves. The SDV enlarges and deposits increasingly amounts of silica until two new valves are formed within the dividing cell in order to protect the two daughter cells when they separate. A schematic of the process taken from Kröger and Sumper is shown in Figure 3.[12]

More than 40 years ago, it was discovered by Volcani that the frustules contain different organic components, indicating that biosilica is a composite material.[13] By acid hydrolysis of purified cell walls, the existence of amino acids derivatives was revealed. The source of these derivatives was later discovered by the purification and characterization of the silaffins, a family of polypeptides covalently bound to long-chain polyamines.[14] Studies of silaffins showed that

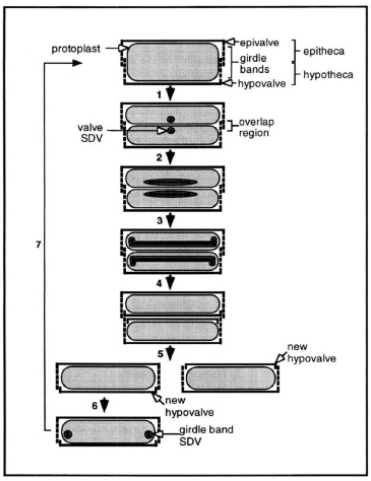

Figure 3: A schematic figure of the diatom cell division process.[12]

these components mediates the formation of silica nanospheres *in vitro* from silicic acid solutions. Different types of silaffins were added to a silicic acid solution and silica co-precipitated with the silaffins in to create a composite with poly-disperse silica spheres with diameter ranging from less than 50 nm to several μm depending on the silaffin type and concentration.[14, 15, 16] It has been shown by Schmid et al. and Losic et al., among others, that the biosilica of diatoms consists of spherical silica units which aggregates into larger spheres or nodules. Schmid et al. has observed silicaspheres as small as 12-30 nm with transmission electron microscopy (TEM) while Losic et al. observed silica nodules with a diameter of 20-35 nm in their AFM-study.[10, 17] It is likely to assume that the biosilica in diatom frustules consists of aggregates of these silica spheres closely related to polyamines and silaffins, perhaps in the form of inorganic spheres embedded in an organic matrix. The exact structure is not yet known, but Sumper has proposed a model which may explain the pattern formation of the frustules of the *Coscinodiscus* genus.[18] The model proposes that long-chain polyamines do not only aid in the precipitation of silica, but also in the pattern formation. When the organic compounds of this genus was studied, only polyamines were found. Silaffins seems to be absent in *Coscinodiscus*-diatoms. The length of the polyamines is species specific, which could help explain differences in the frustule patterns of the different species.

The model assumes that amphiphilic long-chain polyamines can form different phases in aqueous solutions in the SDV. The polyamines might make droplets or micelles with organic content in the aqueous environment of the SDV. These micelles or droplets can self-assemble into a hexagonally close-packed monolayer. In the region between the polyamine droplets and the aqueous phase, which contains hydrophilic silicic acid, precipitation of silica can occur, forming a hexagonal honeycomb pattern. The holes in the bottom plate might originate

from larger droplets in the SDV that excludes the aqueous phase. As silica is precipitated, a defined fraction of the polyamines is consumed. This is assumed to cause a dispersion of the original droplets, segregating smaller droplets. This leads to new interfaces between the aqueous and polyamine phases and precipitation occurs again at these newly formed interfaces. This leads to another segregation into smaller droplets and the process is repeated, leaving ever smaller droplets. A schematic drawing and a comparison with SEM-images of *Coscinodiscus wailesii* in statu nascendi can be seen in Figure 4

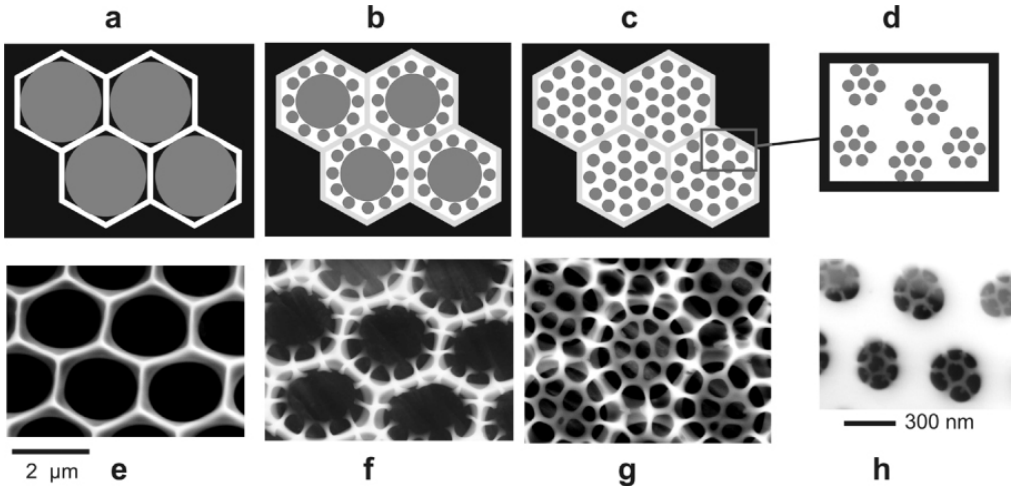

Figure 4: A comparison of schematic drawings of the proposed model and actual SEM-images of the mineralization process.[18]

The driving force of the segregation of droplets is assumed to be the consumption of polyamines and the creation of negatively charged silica surface with a high affinity for the positively charged polyamine-containing droplets. Both these events favor a surface expansion of the droplets. Is is also speculate that the absence of silaffins and the simple structure of the polyamines result in the symmetric patterns in *Coscinodiscus* species. More complex organic constituents could result in less symmetric frustule patterns.[18]

Understanding the details in such a biomineralization process, where patterning is performed simultaneously as the mineralization, would be a giant leap forward in biomimetics. The ability to control the morphology of materials at the nanoscale by self-assembly processes is one of the most efficient ways to increase production of nano-structured materials.

2.2 Modeling of bio-inspired silica

This work is partly done to compare the results of the experimental testing to the works of Markus Buehler's group at MiT. A hierarchical model inspired from the porous structure of diatoms has been developed. The model is based on

atomistic modeling performed by Buehler, Garcia and Sen of a silica honeycomb structure.[19] Using a reactive inter-atomic potential called ReaxFF, a silica crystal with ordered rectangular voids is loaded in uniaxial tension.[20] The voids in the crystal are 76 Å in length and 30 Å in height. The wall width of the model is varied from 5 Å to 72 Å. Figure 5 shows the model setup. The results from the simulations show an increase in ductility for smaller wall widths. In the simulations with smallest wall size, the model geometry changed from rectangular voids to hexagonal voids at maximum stress. This results in a more homogeneous stress distribution and also explains the larger plastic deformation (in fact up to 80 % for the smallest wall sizes). For the larger wall size, the material behavior resembles that of bulk silica. The stress is more heterogeneously distributed with stress concentrations around the corners. The original shape is also maintained up to maximum stress, limiting the plastic deformation. For a more detailed description of the simulations and results, see the work of Garcia.[21] A remarkable result of these simulations is that it is possible to influence material properties such as toughness and stiffness just by altering the geometrical properties of the material, not the material itself. The thinner the walls, the more ductile the system behaves, even if the material is inherently brittle. This increase in ductility, however, comes at a price of loss in stiffness. This geometrical effect has so far only been observed in computational simulations at extremely small size-scales, and it is not known whether the hierarchical structures found in nature takes advantage of such an effect.

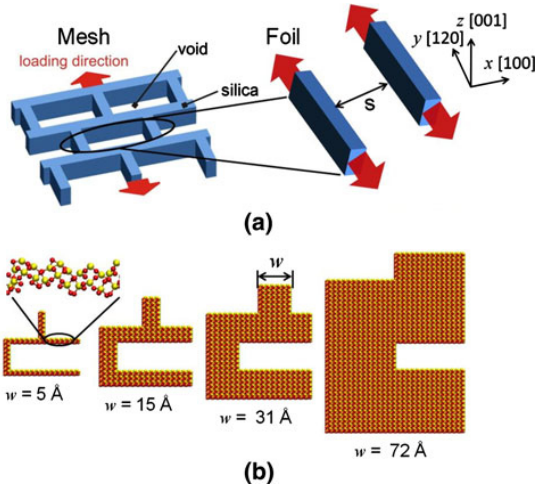

Figure 5: **a)** The model geometry and loading direction. The model has periodic boundaries in the x, y and z-directions. **b)** A selection of the diferent wall sizes used in the model.

Buehler and Sen were later able to extract information from the atomistic model and develop a mesoscale particle and spring model where a composite of brittle bulk silica and ductile nanoporous silica was modeled.[22] The particle-

spring model ensures that larger systems can be modeled over longer time. One of the great challenges with atomistic modeling is the restriction in both size of the system, and how long a simulation can run. Often an entire simulation is on the order of a few ns. A geometry with fibers of ductile phase incorporated in a brittle matrix and vice versa was subjected to uniaxial loading, as seen in Figure 6. The spring constants and inter-particle distance were determined and fitted based on the results from the atomistic simulations. The mesoscale model showed that by clever design of a brittle-ductile composite, it is possible to increase the toughness of silica by 440 % while retaining 70 % of the bulk stiffness. Although the size of the pores in the model geometry are an order of magnitude smaller than the smallest pores observed in the diatom structure, a comparison between these results and the experiments are performed to see whether the biosilica exhibit some of the ductile behavior observed in the model.

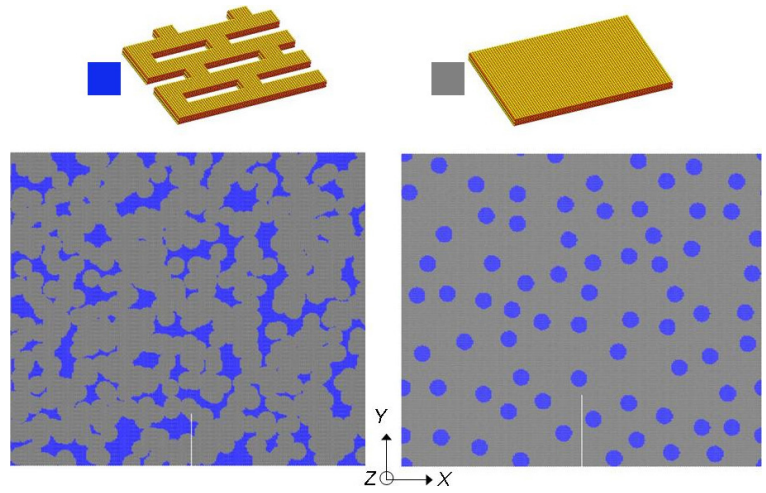

Figure 6: An overview of the fiber-composite meso-scale model. To the left is a model with bulk-silica fibers embedded in a ductile matrix, while the right image shows ductile fibers in a brittle matrix.[22]

2.3 Gas Assisted FIB Induced Deposition

The DualBeam FIB located at the NTNU Nanolab is equipped with a gas-injection system. This provides the ability to deposit different types of material with very high (nanometer range) spatial resolution on almost any solid surface. Gaseous precursors containing the wanted deposition material is injected close to the sample via a needle-shaped gas nozzle. The precursor needs to fulfill two criteria: The gas needs to have sufficient sticking probability in order for enough molecules to stick to the sample surface, and the rate of decomposition caused by the energy from the ion beam must be higher than the sputter rate. The total deposition yield is then determined by the sum of the decomposition yield

and the sputtering yield on the surface:

$$Y_{dep} = Y_{decomp} - Y_{sputt} \tag{1}$$

The two criteria for the precursor leads to the two steps in the deposition-process. First a layer of the precursor adsorbs on the surface of the sample. Then, by scanning the ion beam over the area where deposition is wanted, the adsorbed gas molecules are decomposed into non-volatile and volatile products by the incident energetic ion beam. The non-volatile products make up the deposited layer, while the volatile products are removed by the vacuum system. The deposited material can produce thin or thicker films and create 3D-structures with overhang which are not possible to produce with conventional etching techniques or even FIB-milling techniques.

The deposition conditions have to be optimized, as the surface is sputtered by the ion beam at the same time as material is deposited. The deposition rate is influenced by parameters such as the beam current, dwell time, beam shape and overlap, scanning patterns, gas flux and gas properties. The shape and size of the beam spot is determined by the acceleration voltage, focus and astigmatism. These are controlled by the operator. The resulting beam spot is then scanned over an area determined by the pattern chosen. This pattern has a certain number of pixels. The ion beam is pointed towards each of these pixels and kept there for an amount of time called the dwell time. The beam is then blanked out and moved to the next pixel. The overlap determines how many pixels are within a pattern. If the overlap is set to 50 %, the pixels will be put so that the distance between pixels is half the diameter of the beam spot. If the distance between pixels is larger than the beam spot diameter we get negative beam overlap. If the dwell time is to long, the deposited material will be sputtered away as well as the underlying substrate. This happens because the ion beam deposits and subsequently mills away material faster than new gas molecules can adsorb. A time-dependent model describing the deposition based on these parameters has been developed by Overwijk and van den Heuvel.[23]

The most commonly deposited materials are tungsten (W), platinum (Pt), carbon (C) and aluminum (Al). These are used for editing IC circuits and to deposit protective layers for further micromachining with FIB in especially TEM-sample preparation. In addition to these, gold, copper, iron, silicon dioxide, PMMA and TEOS (insulator) have been successfully deposited with FIB.

For a more detailed description see [24, 25].

2.4 Scanning Probe Microscopy

The atomic force microscope (AFM) is part of a family of microscopes named scanning probe microscopy. Most people associate the word microscopy with optical or electron microscopy, where the probe creating the image signal consist of electro-magnetic light or high energy electrons. In scanning probe microscopy, this probe is replaced by a sharp, needle-shaped, solid probe. This needle is brought into close proximity of or into contact with the sample surface. Under

optimal conditions, this type of microscopes can image individual atoms. To understand this, a short introduction to surface forces are given here.

2.4.1 Surface Forces

When two solid surfaces approach each other, we can differentiate between three different interaction zones: the non-contact region, the intermittent region and the contact region. We have both long-range and short-range forces acting on the surfaces. The long-range forces, usually attractive, are the only forces experienced in the non-contact region. The strongest long-range force is the Coloumbic electrostatic forces, which may be both attractive or repulsive, depending on the charge of the two surfaces. Equal charge gives rise to a repulsive force. At shorter distances the surfaces experience van der Waals forces. These are forces due to polarization, which can be caused by either permanent dipole moments that creates electric fields or fluctuations in the electric fields of polarizable atoms. Both the permanent and the polarizable electric field can induce polarizations of surrounding atoms attractive forces occur. These forces decay rapidly, usually as d^{-7}. At even shorter range, there are strong repulsive forces associated with the overlap of atomic inner electron shells. The forces between two solid surfaces will also be affected by the medium between them, whether a gaseous or a liquid environment, as well as surface roughness and local curvature. The result of these forces can be seen in Figure 7 which is a plot of the potential energy as a function of tip-surface distance. The figure is taken from Jalili et al.[26] This curve distinguish between three regions mentioned earlier. [27, Ch.7]

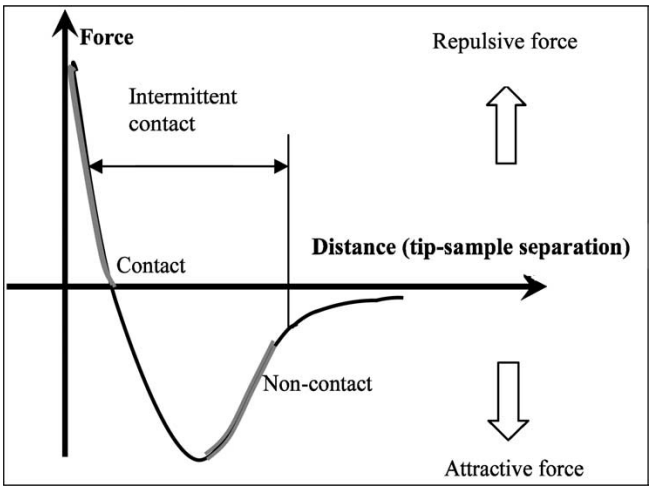

Figure 7: A plot of the potential energy versus the tip-surface distance for a surface probe microscope. The three different regions are marked in the figure.

2.4.2 Atomic Force Microscopy

The atomic force microscope (AFM) has a rather simple set-up. It consists of a sample stage, a tip holder with a cantilever, a laser beam and a detector. It was developed in the late half of 1980 and was commercially available from 1990. The reason that such a simple set-up was not developed earlier, is that in order to achieve the high resolution, one requires tips with very small curvature and a very high scanning accuracy. These enabling technologies, especially piezoelectric motors for moving the sample/tip, were not available until the late half of the twentieth century. Piezoelectricity is an electric response to a mechanical strain and vice versa, i.e. the contraction and expanding of certain materials due to an electric field. The effect is only seen in certain The movement of the tip has to be very precise in order to image small features. In some types of equipment it is the sample stage which is moving while the tip is stationary but the control of the movement is controlled in the same way. An array of piezo-electrodes form a tube which makes up the position control system. By applying a voltage across the length of the tube the walls will expand or contract according to the sign of the voltage. By applying voltages of opposite sign across diagonal segments, the tube will deflect by bending and movement in the x-y direction is achieved.

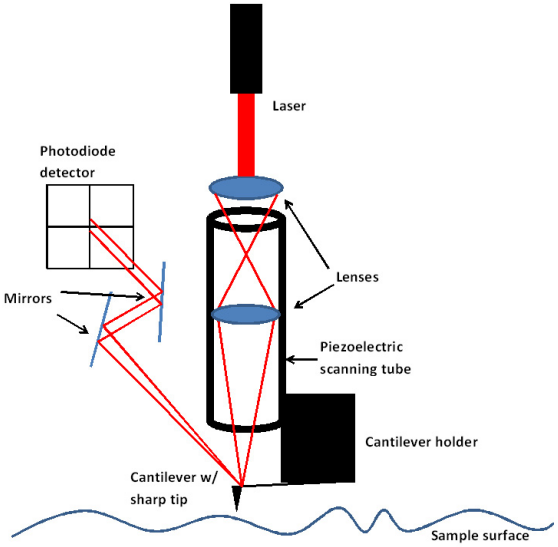

Figure 8: A schematic drawing of a basic AFM set-up.

A schematic figure of an AFM can be seen in Figure 8. The laser is pointed at the cantilever and reflected into the detector. When the tip on the end of the cantilever is brought into close proximity of the sample, forces will start to act on the tip bending the cantilever according to Hooke's law. The reflected

laser-beam will then shift its position on the detector and the signal can be interpreted as a height measure of the surface. The detector consists of an array of photo-diodes and can measure deflection in the two directions corresponding to bending and torsion of the cantilever. The AFM can be operated in different modes, where contact or static mode and dynamic or tapping mode is the two most common. In contact mode the tip is put very close to the sample surface. The forces acting on the tip are mostly repulsive and the forces are kept constant during scanning by ensuring a constant deflection of the tip. The topography of the surface can then be measured from the relative z-distance the piezo-motor has to travel to keep this deflection constant. In tapping mode, the cantilever is brought into the intermittent interaction region where the sum of repulsive and attractive forces are equal. The cantilever is oscillated just below its resonance frequency. This oscillation is dampened by the forces between the tip and the sample which will be repulsive when the tip is very close to the surface and attractive when the tip moves away from the sample. The feedback system of the equipment maintains a constant oscillation amplitude by adjusting the average tip-to-sample distance. The measures of the tip-to-sample distance is then used to create a topographical image of the surface. [27, Ch.7]

2.5 Sample Transfer

The FIB-system is equipped with an AutoProbe 200 from Omniprobe. This system provides a sharp needle which can be controlled in the XYZ-directions with step-size down to 100 nm. The most common use of such an instrument is the transfer of a FIB-thinned sample from the substrate to a TEM-grid. TEM-samples needs to be thinner than 100 nm in order for the electron beam to go through the entire sample. Such thin samples are not trivial to make, but with the aid of a FIB and a nanomanipulator, the process has become a lot easier during the last decades. In addition, both the quality and the through-put has been improved with the help of the FIB.

In order to transfer a sample from one substrate to another, the needle is put in close proximity or in contact with the sample, and with the help of the gas injection system described earlier, samples can be attached to the needle and transfered to another holder or substrate within the vacuum chamber. The sample can then be cut free by ion milling the deposited material between the sample and needle. Thus can very small and delicate samples be transfered and positioned very accurately on a different substrate or holder. The AutoProbe is equipped with a high resolution motor. As with all such motors, hysteresis is an issue. Hysteresis, when it comes to motors, can be described as the dependence between the movement and the incoming signal. The movement in the positive x-direction and the negavtive x-direction is not necessarily two opposite signals. And a signal yielding movement in the x-direction might give rise to some movement in the y-direction as well. This can lead to difficulties when operating the AutoProbe. The hysteresis of the motors must be taken into account when positioning the samples on the substrate.

2.6 Nanoindentation hardness test

Nanoindentation is a technique were the mechanical properties of a material is probed at the micro- or nanoscale. The process is similar to traditional indentation-techniques which can obtain information about the hardness and reduced E-modulus. The difference between nanoindentation and regular indentation is the size of the probe and the force used.

In conventional hardness testing, a tip with a known geometry is pressed into a material with a known load. The indent is then measured and the contact area is calculated from these measurements. The hardness is then given as the max load over the projected area. The projected area is calculated from direct measurements of the indent left by the test. These calculation vary between different hardness tests where Vickers, Brinell and Rockwell are typical tests used.

For nanoindentation it is not convenient to measure the area directly, as the indentation marks are often very small. Such a process would be both inaccurate and very time-consuming. Instead the area is calculated from the force-displacement curves and the indenter area function, the cross-sectional area of the indenter as a function of the distance from the tip, a method developed by Oliver and Pharr.[28] When the indentation is performed the material will deform according to the shape of the tip. However, the material will not follow the exact shape of the tip, as can be seen in Figure 9.

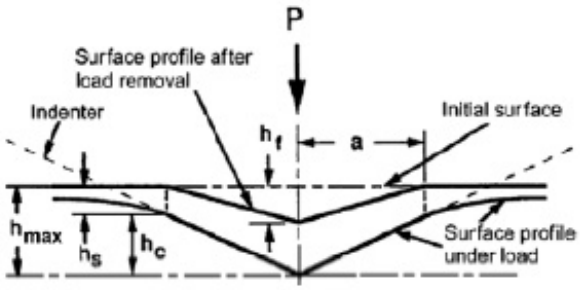

Figure 9: A schematic drawing showing different parameters used in indentation-analysis. Figure taken from Oliver & Pharr[28]

The indenter will only be in contact with the sample up to a certain height on the indenter, marked as h_c in Figure 9. h_c refers to the contact depth at max load. This is the point where the plastic deformation extends to. When the indenter is removed, the deformation outside a radius, shown as a in Figure 9, will recover elastically. In comparison of experimental data with generally accepted values for material properties, Oliver and Pharr found that this height, h_c, gave the most accurate calculations for the contact area. The tips used have a known geometry and based on the plastic deformation done in the test, the contact area between the tip and the test-material can be calculated. A list over

typical tips used and their shape functions are shown in Table 1.

Table 1: Table showing different areas for different tip geometries.[29, Ch.2]

Indenter type	Projected area	Semi angle (θ)	Effective cone angle (ϕ)	ϵ
Sphere	$2\pi R_i h_c$	-	-	0.75
Berkovich	$3\sqrt{3}h_c^2 tan^2\theta$	65.27^o	70.3^o	0.75
Vickers	$4h_c^2 tan^2\theta$	68^o	70.3^o	0.75
Knoop	$2h_c^2 tan\theta_1 tan\theta_2$	θ_1=86.25^o, θ_2=65^o	77.64^o	0.75
Cube corner	$3\sqrt{3}h_c^2 tan^2\theta$	35.26^o	42.28^o	0.75
Conical	$\pi h_c^2 tan^2\phi$	ϕ	ϕ	0.72

As seen in Table 1, when the tip geometry and the height is known h_c, the projected area can be calculated which again can be used to find the hardness and reduced elastic modulus through Equations 2 and 3.[28]

$$H = \frac{P_{max}}{A} \tag{2}$$

$$E_r = \frac{\sqrt{\pi}}{2}\frac{S}{\sqrt{A}} \tag{3}$$

2.6.1 Calculation of h_c

The projected area under the indenter, or the contact area, is an important factor in the analysis of indenter data. By using indenters with known geometries there is a relationship between the cross-sectional area of the indenter and the distance from the tip, described as F(h). As mentioned earlier, Oliver and Pharr discovered that the most accurate determinations of the contact area were done when analyzing the contact depth h_c, or in other terms A=F(h_c). To determine h_c from the experimental data, Figure 9 must be examined. Here it is seen that:

$$h_c = h_{max} - h_s \tag{4}$$

h_{max} is given directly from the indenter while h_s can be found from the experimental data as:

$$h_s = \epsilon\frac{P_{max}}{S} \tag{5}$$

where ϵ is a geometric factor for the tip shape (seen in Table 1), and S, or the stiffness, is the slope of the initial unloading curve. Combining Equations 4 and 5 results in:

$$h_c = h_{max} - \epsilon\frac{P_{max}}{S} \tag{6}$$

where all values can be found from the experimental data obtained from the indenter.[28, 29]

2.6.2 Determination of F(h_c)

For an ideal situation with a perfectly shaped tip, the area function could now be calculated from the formulas shown in Table 1. However, as it is known, the world is not ideal. Due to irregularities in the shape of the tip and compliance in the indenter hardware, the area calculated will deviate from the actual contact area. The compliance is the deflection in the system itself, not the sample material, during loading. In other words, a part of the contact depth measured by the transducer is a deflection in different parts of the instrument and not deformation in the sample. This can be determined by analyzing a set of indentations on a standard specimen of fused silica with known elastic modulus and hardness. Plots of E vs h should be a straight horizontal line with the given value of E and a plot of H vs h should be flat, with no change in H with increasing h. The compliance C_f, which can be incorporated in the area function, can be changed in order to fit these two plots. Re-analysis of the data set is required with the updated compliance value.

The area functions from Table 1 will also have to be corrected in order to use them practically. The tips will never have ideal shapes, and especially at low indentation depths, the tip will be somewhat blunted when compared to an ideal case. This is corrected by introducing a correction factor in the area function. This correction factor is given as A/A_i where A is the actual area of contact and A_i is the area as calculated from the ideal area function. The value of this factor is usually high at low contact depths and approaches unity as the contact depth increases, a consequence of inevitable bluntness of the tip. A popular correction expression for this is:

$$A = C_1 h_c^2 + C_2 h_c + C_3 h_c^{1/2} + C_4 h_c^{1/4} ... \tag{7}$$

Where the first term represents the area function for an ideal case. The ratio A/A_i can then be calculated and the corrected value for A can be found via measurements on standard samples with known hardness and elastic modulus and the following equations:

$$H = \frac{P}{A}\left(\frac{A}{A_i}\right) \tag{8}$$

$$E^* = \frac{dP}{dh}\frac{\sqrt{\pi}}{2\beta\sqrt{A}}\sqrt{\frac{A}{A_i}} \tag{9}$$

This method might require some iteration on the calculations of A and the compliance of the system, but the calculations can be performed on the same set of measurements until the calculated values of H and E correspond to the known values of the sample.

2.7 Beam Theory

As a continuation of the project work, the testing of the mechanical properties of the *Coscinodiscus* sp. will be performed as a three point bending test.[6] In

order to analyze the results from the bending tests, and convert the force and displacement into stress and strain, a simplification of the system is required. The cross-section of the beams will be simplified to an I-beam. The justification for this is that the structure of the diatom resembles such a system. The structure of the diatom can be described as a top and bottom layer separated by a honeycomb-structure. If we look at the cross-sections of a simplified beam with a row of single hexagons aligned with the beam-direction, as seen in Figure 10, we can see that the cross-section will vary from two extremes, an I-beam and a hollow rectangular-beam. The stress-distribution for a beam in bending can be found by

$$\sigma = \frac{My}{I} \tag{10}$$

where M is the internal moment of the beam, y is the distance from the neutral axis and I is moment of inertia. I is defined as:

$$I_x = \int_A y^2 dA \tag{11}$$

The moment of inertia for a rectangular beam with a centroidal axis is simply:

$$I_x = \int_{-h/2}^{h/2} bz^2 dz = \frac{b}{3}\left(\frac{h}{2}^3 - \frac{-h}{2}^3\right) = \frac{bh^3}{12} \tag{12}$$

To simplify the calculations, the diatom-beams are assumed to be symmetric along a central axis. The moment of inertia for an I-beam can then be calculated as the moment of inertia of a rectangular beam minus two smaller rectangles with centroidal axis a distance from the centroidal axis of the rectangular beam (parallel-axis theorem). The moment of inertia for the I-beam is then:

$$I_x = \frac{bh^3}{12} - 2\frac{b_i h_i^3}{12} \tag{13}$$

The exact same formula can be used to calculate the moment of inertia for the hollow-rectangular beam. The only difference will be the value of b_i, as the middle rectangle of the hollow-beam can be divided into two smaller rectangles as well.

The strain in a bending beam can be found by considering the distance from the neutral axis and the radius of a circle which will conform to the shape of the bending beam via the formula:

$$\epsilon = \frac{-y}{\rho} \tag{14}$$

The sign convention tells us that a part of the beam which is located above the neutral axis will experience contraction, while a part located below the neutral axis will experience elongation. The curvature of the beam can be found with the help of the Pythagorean theorem: Given the length of a chord, x, and the

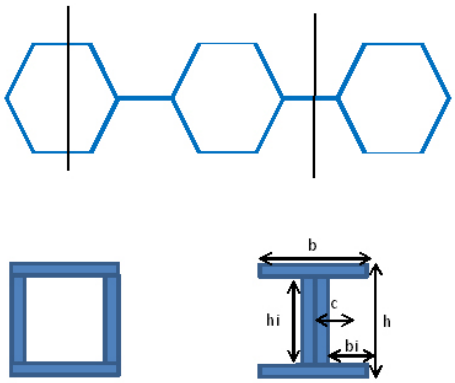

Figure 10: A schematic drawing showing the similarities of the beam-structure of the diatom-beams and an I-beam.

length of the sagitta, the normal line to a chord, y, the radius of a the circle which will fit these two values is given by:

$$r = \frac{x^2}{8y} + \frac{y}{2} \tag{15}$$

This radius corresponds to the radius of curvature in Equation 14

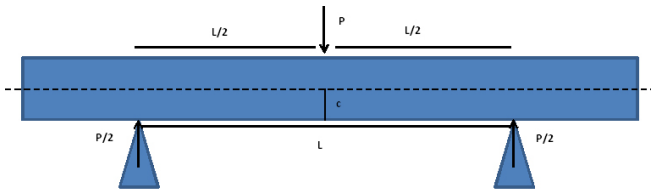

Figure 11: A schematic of the three-point bending test. The dotted line marks the neutral axis.

In order to investigate the fracture properties of the beam, it is convenient to consider the maximum tension stress the beam is experiencing. This will be at the point directly below the applied load on the far side from where the load is applied. To find the maximum stress, we simply insert the distance from the neutral axis to the lowest point on the beam for y, named c in Figure 11. We find M from the half maximum load just before fracture and the distance from the support point of the holder to the applied load, given as P/2 and L/2 in Figure 11.

$$\sigma_{max} = \frac{Mc}{I} = \frac{PLc}{4I} \tag{16}$$

The strain value is found by inserting the value of L from measurements of the beams, and the value for the vertical displacement given by the experiments into Equation 15 and obtain:

$$\epsilon_{max} = \frac{c}{\rho} \tag{17}$$

The negative sign disappears because the beam is in tension below the neutral axis, yielding a negative value of c.

If we assume that the system is elastic until fracture, we can use Hooke's law to find the elastic modulus of the beam, in this case the flexural modulus:

$$E = \frac{\sigma}{\epsilon} = \frac{PL\rho}{4I} \tag{18}$$

A more detailed description can be found in Chapter 6 and Appendix A of Hibbeler.[30]

3 Experimental

Thanks to the Biological Institute at NTNU, diatoms of the species *Coscinodiscus* were available for testing. The diatom frustules have undergone three different chemical treatments in order to remove the cell-material and other organic material. The treatments include a chemical washing treatment followed by centrifugation and rinsing in water. This process is repeated three times. The difference in the cleaning methods is the chemical agent used. For the mildest treatment, SDS, an anionic surfactant, was used. For the somewhat harsher treatment, sulfuric acid, H_2SO_4, was used. For the harshest treatment, hydrogenperoxide, H_2O_2, was used. See the Appendix for a detailed description of the SDS-treatment. The three treatments are very similar, the only difference is the aforementioned rinsing agents. The difference in organic content has been confirmed with fluorescence spectroscopy, and showed clearly that harsher treatments yields less organic matter. The cleaned frustules were stored in methanol until used. In this work, frustules from the SDS-treatment and the H_2O_2-treatment are studied. The H_2SO_4-cleaned frustules were omitted in order to save time, and it was believed that any effect on the mechanical properties would be observed between the two types with the largest difference in organic content.

The following section will describe the essentials of the experimental work starting with the AFM-study followed by a description of the nanoindentation test and finally the main test scheme developed in this work, from sample preparation to bending tests in the nanoindenter. The description of the procedures are presented in a short and concise manner with as little elaboration as possible to ensure that the procedures can be understood and repeated by consulting this section alone. While some important concepts and pitfalls are highlighted in this section, a more thorough discussion of challenges and improvements is given in Section 5.

3.1 AFM

The frustules were drawn from the methane they were stored in with a regular pipette and put on a standard steel sample holder with a small piece of double-sided tape. The tape wss to ensure better adhesion between the frustules and the substrate. This was important in order to avoid that the frustules stuck to the AFM-tip during imaging and to prevent movement and pivoting of the frustules. A Veeco diMultiMode V AFM was used in tapping mode for the frustule imaging. Standard silicon tips were used in combination with the E-scanner, which limits the scan to 12 x 12 μm.

In order to get a good image, the tip approach was crucial. The tip had to be brought onto an area of the frustule which had as little curvature as possible, preferably close to the center of the frustule. This was done to avoid that the scanner head had to move too much in the z-direction. The AFM is more accurate if the travel-distance in the z-direction is minimized. Too large variations in the z-direction can even cause loss of contact between the tip and

sample, or in worst case damage to the scanner head. Both the external and internal surface of the frustule was imaged. Topography and amplitude images were recorded for each sample.

3.2 Nanoindentation

Before testing, the tip was calibrated to the optics by performing a H-pattern of indents on a soft metal, in this case indium, or a piece of polycarbonate. A suited area with as little wear as possible was located on the calibration-sample. An image of the surface prior to the indents was saved for comparison with the surface after indents. The desired tip was installed in the nanoindenter and 7 indents in the shape of an H was performed on the sample. The load depended on the shape of the tip, and the material of the calibration sample. When the indents were made, the center of the optical view was positioned over the middle indent in the H. This calibration ensures that the tip will touch down on the same area as the optics are looking at.

Nanoindentations on the internal part of the frustules were performed. This was done in order to obtain data which can be compared to literature values, and to obtain additional information about the effects of the different cleaning procedures. Losic et al.[31] suggests that the internal part of the frustules, the foramen, is the main structural part when it comes to mechanical properties. In addition, this layer also features areas without pore-structure so that indentations will be performed on a more homogeneous part of material. The frustules were placed on a glass slide with a pipette and the methanol was evaporated in air. The H_2O_2 frustules were mostly split into two valves, which settled on the surface in either a convex or a concave manner. The SDS-cleaned frustules had a larger percentage of intact frustules, but it was possible to find separated valves here as well. The slide was observed in an optical microscope, capable of high magnification (100 X) and valves in the convex position (internal part upwards) were chosen for indents. These were again located with the microscope in the indenter and a scanning with the indenter tip was performed in order to confirm that the frustules were not moving around on the slide. The scanned images were used to place several indents and perform runs of 5-15 indents on each frustule. The surface was scanned afterwards as well to confirm that no movement occurred during indentation and to obtain an image of the indents.

Indents were performed on both sets of frustules with a cube-cornered tip. Indentation with a Berkovich tip was also performed on the H_2O_2-cleaned frustules. 5-15 indents with a set-force of 200 μN were performed with the cube-cornered tip on 6 different H_2O_2-cleaned frustules and 3 different SDS-cleaned frustules. In addition 14 indents were performed on one H_2O_2-cleaned frustule with the Berkovich tip with a set-fore of 200 μN.

3.2.1 Nanoindentation of steel substrate

In order to investigate whether the steel substrate was affecting the results of the bending tests, a series of 25 nanoindentations were performed with the conical

tip. The area function of this tip was not 100 % accurate, but the results gave an estimate of the hardness and the E-modulus of the steel substrate. 25 indents, ranging from 400 μN to 4000 μN, with an increase of 150 μN, were performed on a flat, clean part of the steel substrate. The substrate was scanned with the indenter-tip before and after the indents were made. This was done to confirm that the indents reach sufficient depth and to check the indent geometry.

3.3 Beam specimen fabrication

A large part of this work was to develop a method which can be used to test diatom frustules in a consistent way. The equipment available was a DualBeam FIB and a nanoindenter. These two instruments are located in different buildings on campus which involved transferring of the samples from the FIB to the indenter. The indenter is equipped with a low magnification (10X) optical microscope and the tip can be used to make scanning probe images of the sample surface. In normal use, the indenter would make indents on a flat surface. In this case the indenter was used to apply force on a beam in order to bend it, not perform an indentation. A major problem with the indenter was that due to the low magnification of the optical system, the positioning of the tip was not very accurate. In order to get the accuracy needed for exact placement of the tip a scanning of the area of interest had to be performed.

The experimental set-up described herein was a further development of the test-scheme described in the project work.[6] In the project work the beams were left as an integral part of the frustule and tested in a nanoindenter. The results indicated that the entire frustule flexed with the loading, leaving analysis of the data difficult. To avoid the response from the substrate a new method was developed. Instead of leaving the beams clamped within the entire frustule, the beams were transfered to a steel-holder made with the FIB.

Sample holder fabrication: The FIB was used to mill a rectangular ditch in a flat, polished steel substrate. The ditch measured 12 x 15 x 5 μm, w x h x d. An overlapping groove for the beam, measuring 24 x 4 x 5 μm was milled simultaneously. This ensures that the material in the area underneath the beam was milled 10 μm deep. See a schematic drawing in Figure 12. The reason for this design was that the beams should be free-hanging during the bending test. Also, the nanoindenter used in this work needed to scan the surface of the sample before applying the load to ensure that the load was applied to the middle of the beam. The nanoindenter has a height-difference limit of about 4 μm during such a scan, so the beams had to be lowered into the substrate. The dimensions of the sample holder were chosen so that the result would be a bending test of a 12 x h x d μm beam. The width and height (here given as h and d to keep the naming convention of this paragraph) of the samples might vary from beam to beam depending on the frustule itself. The height (not depth) of the sample holder was set to 15 μm. This was to ensure that the tip in the nanoindenter would be able to image the holder during scanning. The dimensions were kept as low as possible to keep the milling time down.

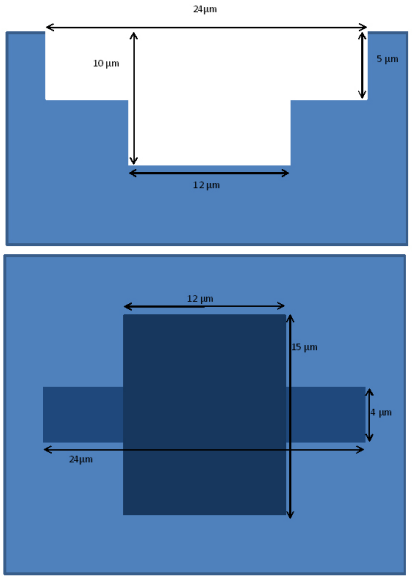

Figure 12: A schematic figure of the FIB-machined sample holder. The top image is a side-view cross-section while the bottom image is top-view.

Beam specimen fabrication: When the fabrication of the holder was done, the stage in the DualBeam FIB was shifted to the sample with diatoms. Care must be taken when switching between samples in the FIB. If there is a height difference between the samples, the working distance of the electron beam will change between the samples. This height difference will affect the focusing and beam-spot parameters, and if the difference is large, the highest sample might even touch vital parts inside the vacuum-chamber. Always lower the sample before moving large distances on the stage. The sample holder with diatoms was prepared as following: The diatoms were drawn from the methanol solution and put on an aluminum sample holder with a pipette. The methanol was evaporated in a stream of nitrogen for 1 min. The sample was covered with 5 nm of platinum using a Cressington 208 HR B sputter-coater. This layer will conduct the electrons away from the frustules, while being thin enough to not affect the mechanical properties in a large degree.

A suited diatom valve was found with the electron beam, and the sample was tilted to 52°. This is the angle between the beams in the FIB. Working at this angle ensures that the ion-beam is perpendicular to the sample surface. Care was taken that the sample-height was at the eucentric height. This is the plane in which the ion- electron beam cross each other. It was crucial that the sample is in the viewing area of both beams, as it was necessary to view the sample from both angles when positioning the sample-transfer needle. With the "cleaning cross-section"-tool two rectangles were milled away from a desired location on the frustule (top left in Figure 13). The cleaning cross-section has a milling

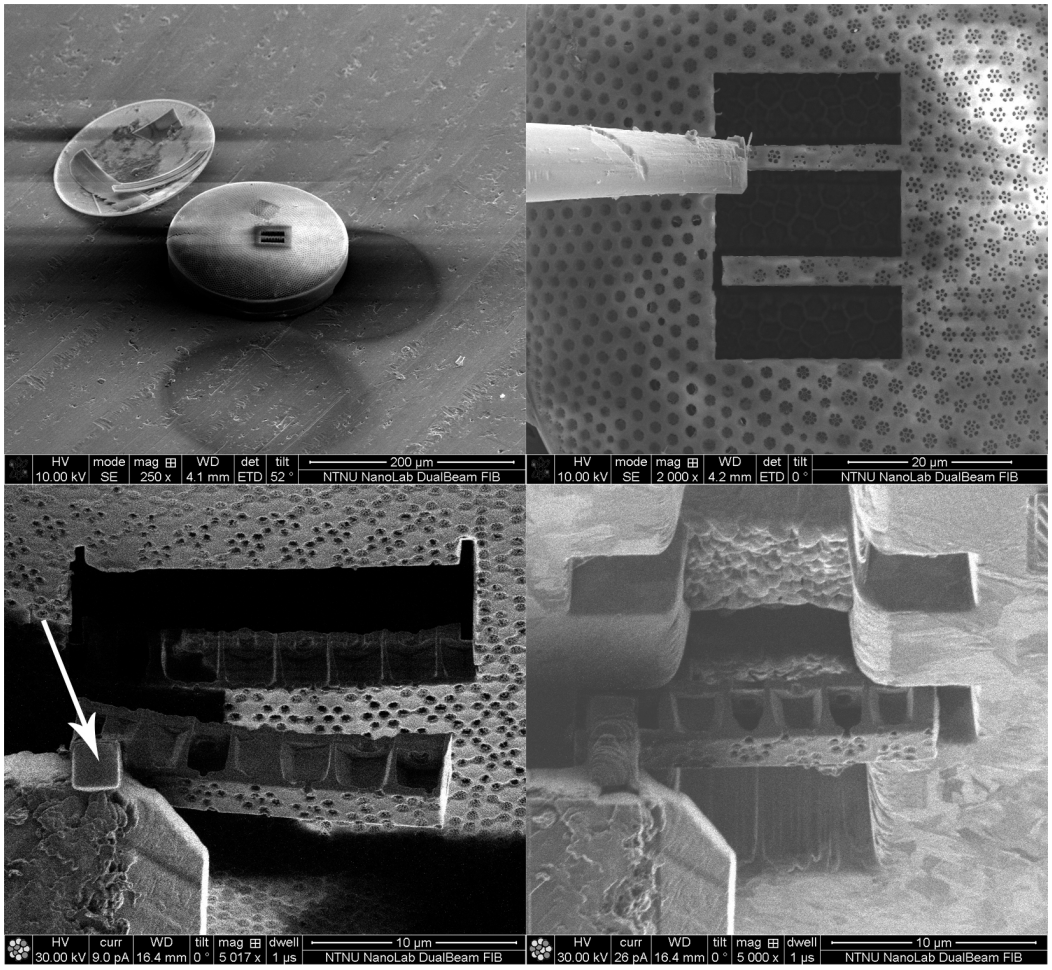

Figure 13: Four SE-images depicting the beam-fabrication process. **Top left:** A low-resolution image of a valve with two rectangles milled away. **Top right:** A close-up image of a valve with three rectangles milled away, leaving two beams. The tungsten needle is attached to the upper beam. **Bottom left:** An image taken with the ion-beam showing the lift-out process. The arrow points to deposited platinum. **Bottom right:** An ion-beam image of the beam being placed in the sample holder.

pattern which removes a single line of material before moving to the next line. At the end of the pattern, the beam-current was reduced so the ion-damage in the region of interest is reduced. The frustule beam was then the remaining material between the two rectangles. The beam was cut free at one end and the tungsten needle was inserted into the vacuum-chamber.

Sample transfer: At this point, the platinum source was heated to make sure it was ready for use. The tungsten needle was introduced into the chamber and lowered in large steps until it was situated $\sim$ 30 μm over the sample surface. As there is some hysteresis in the motors which move the needle, a combination of viewing the needle from directly above with the electron beam, and from the side with the ion beam, was used to position the needle at the end of the beam which was cut free from the rest of the frustule (see top right in Figure 13). This double-view approach is one of the many advantages with a dual-beam set-up. The latter approach was done with decreasing step size, and the final positioning, where the needle just touched the beam, was done with a step-size of 1 or 0.5 μm. The ion beam current was kept as low as possible (9-26 pA) during the imaging to reduce ion-damage. When the needle and beam was in contact, the gas-injection needle for the platinum was lowered to a few hundred μm above the sample surface. It is beneficial to wait until the actual deposition-step in the process before introducing the gas-injection needle. Although there should be no gas-flow when the vent is shut, some leakage may occur, and this can lead to unwanted deposition of material during regular imaging. A rectangular pattern of about 1.5 x 1.5 μm with a thickness of 1-2 μm was set to cover part of the needle and part of the beam. The deposition should be made as close to the edge of the beam as possible. The platinum was then deposited with an ion-beam current of 26 pA to 0.26 nA. See the bottom left image in Figure 13 for an example of a successful deposit.

After the beam and needle was connected with platinum, the other end of the beam was cut free with the ion beam and the needle was lifted carefully up from the frustule. This had to be done with several correctional steps due to the motor-hysteresis. At the initial part of a movement in the +z-direction the needle moves in the -x-direction. The needle therefore had to be moved as far in the +x-direction as possible before it was lifted up. As the deposited platinum is rather ductile, the beam can be bent out of the correct position if the sample touches the frustule when it is lifted up. When the beam was lifted successfully out of the frustule, both the gas-injection needle and the tungsten needle had to be retracted before moving the sample stage back to the sample holder. The process was then repeated in reverse: the tungsten needle was again inserted and lowered towards the sample surface. The double-view approach was used to correct for motor hysteresis and position the beam slightly off-center of the beam holder. The motor hysteresis was largest at the start of every movement and was repeated whenever movement in one direction was initialized. This meant that the final lowering of the beam into the sample holder would induce movement in the x-direction as well as the z-direction. The beam had to be

placed in a way that took the hysteresis into account for the final step of the sample positioning. When the sample was well in place, the beam was either fastened to the sample holder with platinum, before the needle was cut free, or the needle was cut free and the van der Waals forces kept the beam in place in the sample holder. An image of the final step can be seen at the bottom right in Figure 13.

3.4 Three point bending test

After the fabrication and placement of the frustule beams in the steel sample holders, the steel substrate were moved carefully to the nanomechanical lab located in a different building on campus. The specimens were examined in an optical microscope at 50-100 X magnification to verify that the beams were in place in the sample holders. The steel substrate was then placed in the Hysitron nanoindenter and the area with the sample holders were located with the optical microscope in the nanoindenter. For the three point bending tests, a conical tip with a measured tip radius of 0.6 μm was used. The microscope and tip position has to be calibrated as described in Section 3.2. The tip was brought down to the sample holder close to a beam and the exact position of the beam was located with a scanning image. The tip was then placed in the center of the beam, and a load was applied with a loading rate of 27 μN/s. The load applied started at 200 μN for the complete beams and was increased until the beam fractured. This was done both to observe the elastic response of the beams, and to ensure that the beams were situated at the bottom of the sample holder, and not stuck to the side walls due to van der Waals forces. A lower initial load was used for the beams made from the different layers, as these were expected to fracture at much lower loads.

The first tests were performed with free hanging samples, but 50 % of the samples were removed from the sample holder by the scanning tip, presumably due to the forces between the tip and the beam exceeding the van der Waals forces between the beam and the holder. This lead to a change in the set-up where the beams were attached to the sample holder with a small piece of deposited platinum. The intention of these attachments was that they would be strong enough to keep the beams in place during scanning with the indenter tip, and weak enough to break off during the initial part of the loading so that the beams would settle in the bottom of the sample holder.

For the SDS-cleaned samples, 4 successful bending tests were performed on complete beams in addition to tests of 1 foramen beam, 1 cribrum beam and a complete beam situated upside down. For the H_2O_2-cleaned samples, 8 complete beams, 2 foramen beams and 1 cribrum beam were successfully tested.

4 Results

In the Results section, the results from the different experiments will be presented. The results are presented in the same order as the previous section and interpretation and analysis of the data is limited to a minimum, as it will be thoroughly discussed in Section 5. Some discussion occur, however, in order to give the reader an understanding of certain parameters and origins of the data.

4.1 AFM-study

Four sessions with the AFM were performed during this work. The two first sessions were unsuccessful, as the images showed nothing but noise. The suspected reason for this was that the frustules that were being imaged did not lay still on the substrate, but moved along with the scanning tip. The third session was focused onto imaging the outer surface of the frustule, namely the cribellum and cribrum layers. The fourth session was focused on imaging the inner surface of the frustule, the foramen layer. For the two last sessions, more effort was put into locating frustules which seemed to be strongly attached to the adhesive tape. This strategy turned out to be successful, and images of both the inner and outer surface was obtained. The most valuable information from the AFM-study is the height-measurements of the different features on the frustule. These measurements show that the height of the lip around the foramen holes are on the order of 150-180 nm (see Figure 14). A 3D-image of the same surface is also shown in Figure 15 to give a more intuitive understanding of the AFM-image.

The cribellum surface is shown in Figure 16. The larger pores of the cribrum is also visible as larger dark areas, but the details of this layer is obscured by the overlaying cribellum. In this image it is apparent that the cribellum is the outermost layer of the frustule.

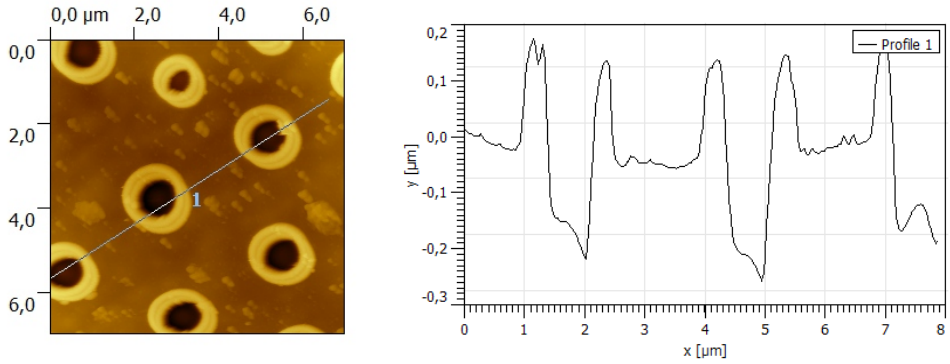

Figure 14: An AFM-image of the foramen-layer of an H_2O_2-cleaned frustule. The topography along the line is shown in the right image.

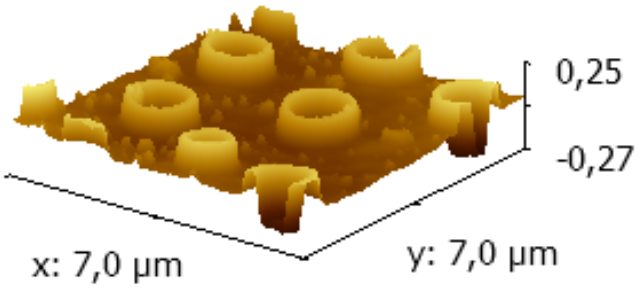

Figure 15: A 3D-representation of the AFM-image of the foramen surface.

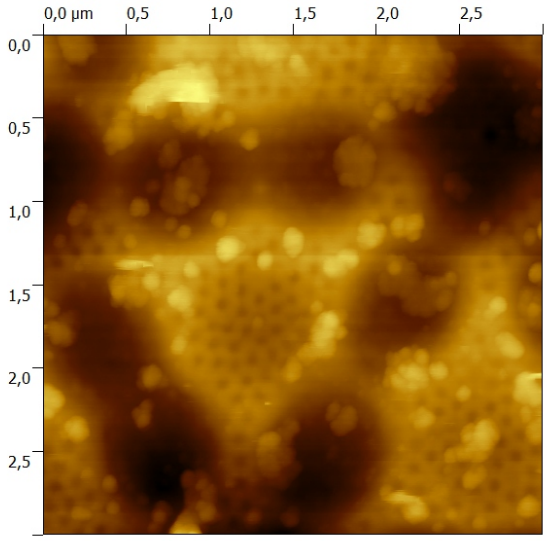

Figure 16: A topographical image of the cribellum with the larger pores of the cribrum visible as darker areas.

4.2 Nanoindentation

Nanoindentation experiments were performed on frustules cleaned with SDS and H_2O_2, as well as the steel substrate which the sample holders were made of. The nanoindentation on the frustules were performed with a cube-corner tip and a Berkovich-tip, while the nanoindentations tests on the steel substrate were performed with the same conical tip as used in the bending tests.

4.2.1 Nanoindentation of frustules

The nanoindentations with the cube-cornered tip showed very different results for the SDS-cleaned and H_2O_2-cleaned frustules. Indents were performed on the H_2O_2-cleaned samples with an open-loop control of the loading. The force was set to be 200 μN and 15 indents were performed on a single frustule. Figure 17 shows the force-displacement curves for such a set of indents. With the open-loop control there is no feed-back during the loading, so the indenter-system applies the load according to the load-rate for a certain time. It is clear to see from the graph that the load is reduced while the displacement is increased. One can also observe that most of the deformation is recovered in the unloading curve. This type of behavior is an indication that the frustules are pivoting during indentation. However, this was not discovered until after the tests on the H_2O_2-samples were analyzed, so all the indentations on H_2O_2-samples were done with the open-loop control. It was believed that a load-controlled feed-back would give results that were easier to compare, even with this pivoting, as each indent would be subjected to the same force. The indents on the SDS-samples were performed with load-control. This ensured that the same load was reached for every indent.

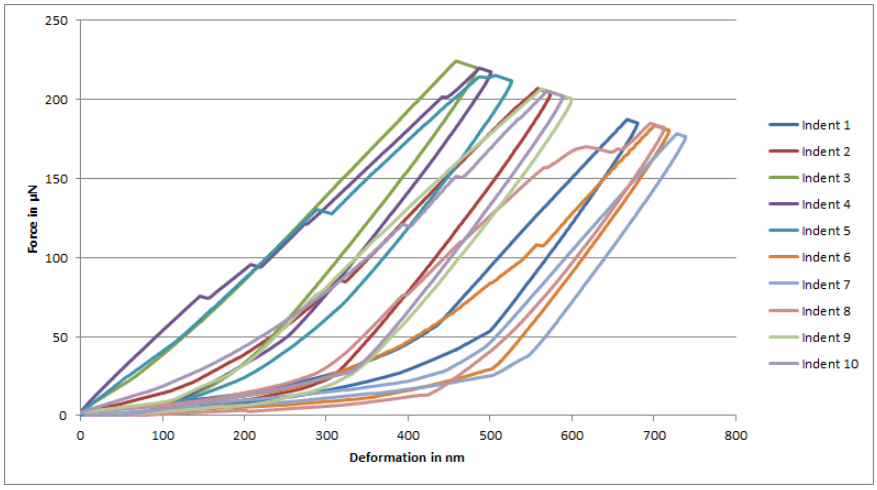

Figure 17: The force-displacement curves for nanoindentations in an H_2O_2-sample. The behavior is representative for all such samples.

The behavior of the SDS-cleaned frustules differed drastically from the H_2O_2-samples. The pivoting effect is much less pronounced, although there appears to be some tilting. The indents also gave a much greater permanent deformation which was not recovered. The force-displacement curves for a typical SDS-sample can be seen in Figure 18, and a comparison of the size of the indent-craters can be seen in Figure 19. Only a few indents are marked in Figure 19 and a full comparison of the force-displacement curves with indent-position can be found in Figures 37 and 40 in the Appendix A.1. Important observations are:

- The indentation depth (size of craters) seems rather consistent in the H_2O_2-sample although the total deformation-distance is different in Figure 17.
- The craters vary greatly in size for the SDS-sample (marked with arrows in Figure 19).
- The diatoms appear very different. This could be two different *Coscinodiscus* species.
- The two-sloped behavior is observed in both cases, but is more pronounced for the H_2O_2-samples.
- The force where the large pop-ins occur in the SDS-samples vary from 60-170 μN.

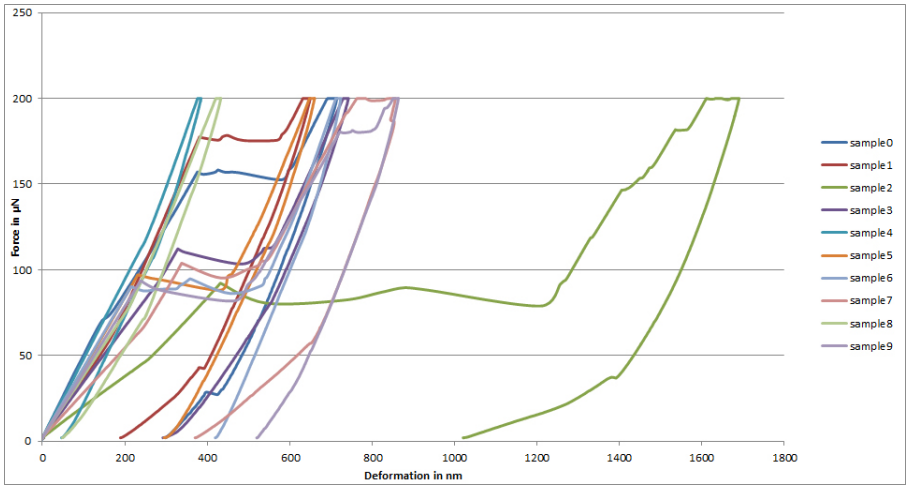

Figure 18: The force-displacement curve for typical indentations in an SDS-sample.

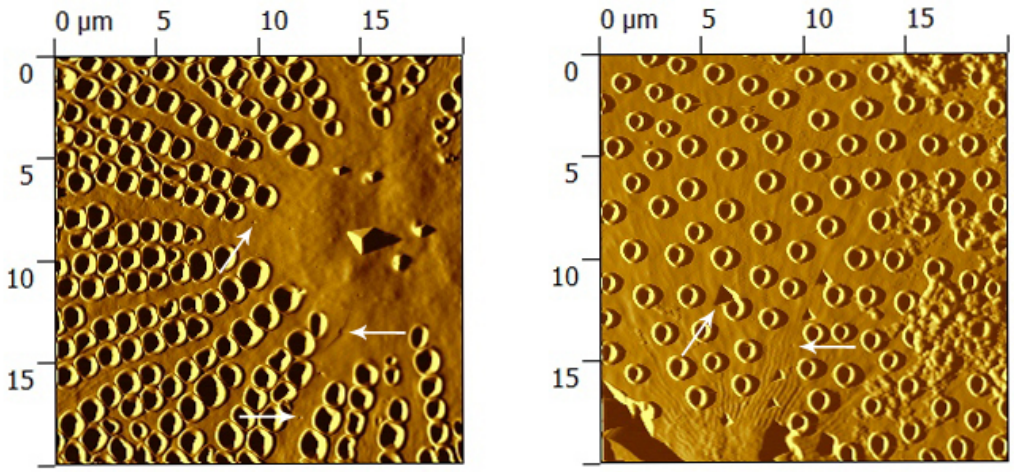

Figure 19: A comparison of the indentation-craters in the H_2O_2-sample (left) and SDS-sample (right). The craters are barely visible and rather consistent on the H_2O_2-sample, while the craters in the SDS-sample are much deeper and differ in size. Only a few craters are marked in each case.

4.2.2 Nanoindentation of steel substrate

The results from the 25 nanoindentations with loads ranging from 250-2500 μN resulted in somewhat scattered results as can be seen in Table 3. The average reduced E-modulus was calculated with the method described in Section 2.6 to be 163 $\pm$ 16.8 GPa. The hardness is found to be 5.73 $\pm$ 1.05 GPa. A typical force-displacement curve for the nanoindentations in steel is shown in Figure 20. The shape of this curve is consistent with the typical behavior of nanoindentations in metals. A before and after scan of the steel-substrate surface is shown in Figure 21.

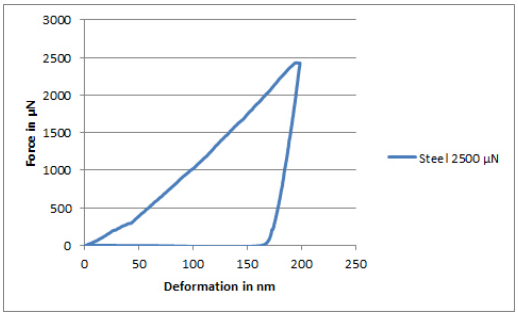

Figure 20: A typical fore-displacement curve for the nanoindentations in steel.

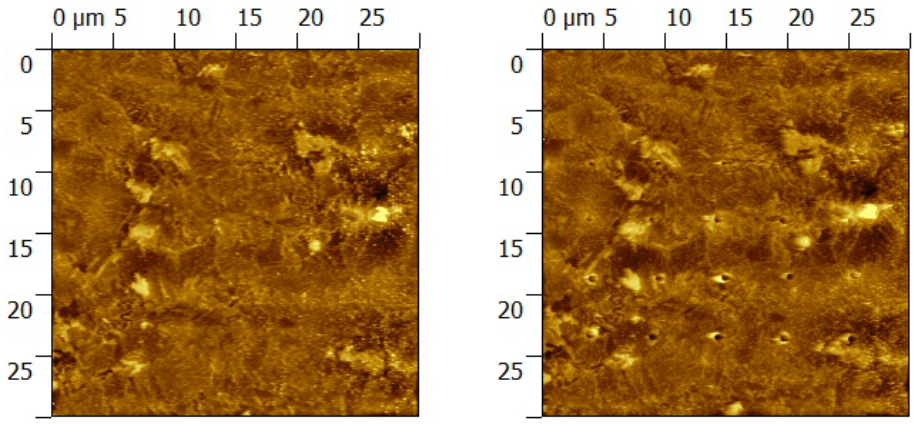

Figure 21: Before and after scanning of the steel surface. The indents are clearly visible in the right image.

4.3 Three point bending test

The force-displacement curves for all the H_2O_2-beams are shown in Figure 22 and the force-displacement curves for the all SDS-beams are shown in Figure 23. A full overview of the curves for each beam combined with before and after images can be found in Appendix B. These curves were converted into stress-strain curves via the calculations shown in Section 2.7, specifically Equations 10 and 14. The cross-section used for the conversion was based on the assumption that the average cross-section will vary between an I-beam and a hollow-rectangular beam. The calculations for the moment of area for these two structures were very similar. By assuming that the side walls of the hollow-beam were half the width of the middle truss in the I-beam, the calculations were exactly the same. The calculations do not take into account the holes in the foramen or cribrum layers and also do not take into account the domed structure on top of the areolas. The dimensions of each beam was measured from SEM-images except the internal height and width, marked as h_i and b_i in Figure 10. The thickness of the foramen and cribrum was assumed to be 500 nm, so the internal height was calculated as 1 μm less than the external height and the internal width was estimated to be 600 nm less than the external width. The values are slightly conservative and should not result in an overestimate of the stress values. These measurements were inserted into Equation 12, and the moment of area for the resulting I-beam was calculated. The stress in the beams were also calculated using the formulas for a massive rectangular cross-section. The analysis is done in order to obtain a first approximation of the fracture stresses for the beams, and are not believed to be entirely accurate. The results for the fracture stress can be found in Table 4 in Appendix B and in Figure 24, where the stress-strain

curves for the complete beams are shown.

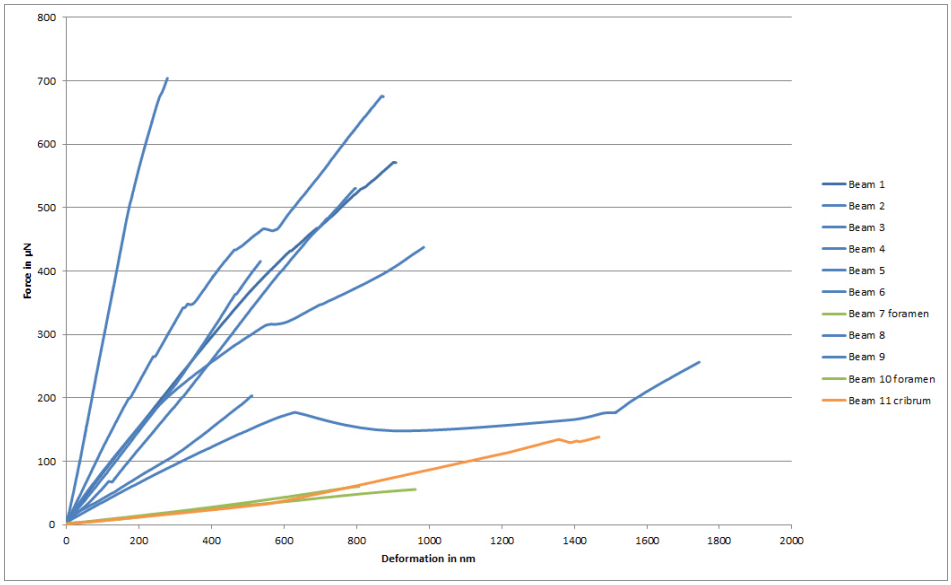

Figure 22: The force-displacement curves for the H_2O_2-beams.

Important observations are:

- The force required to break a complete beam varies from 350-1050 μN.
- The force required to break a complete beam is 4-10 times larger than the force required to break a beam made from either the cribrum and foramen.
- With one exception, the SDS-cleaned beams appear to be slightly stiffer than the H_2O_2-cleaned beams.
- The biosilica appears to be very brittle.
- The fracture stress calculated with I-beam cross-section is 2-4 times larger than for pure amorphous silica. For the rectangular cross-section the fracture stress is 1.5-3 times larger.
- The flexural modulus of the beams is found to be 5.72 $\pm$ 2.90 GPa.

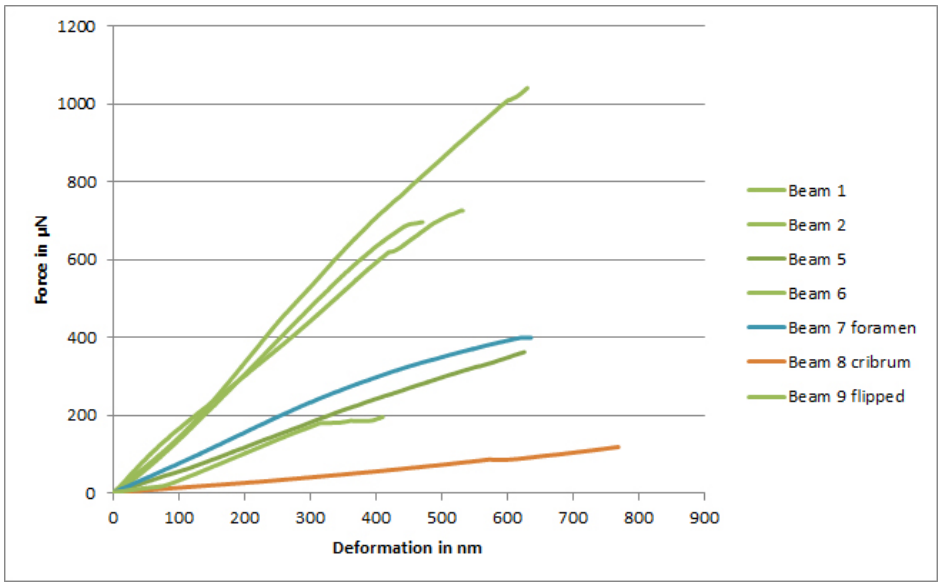

Figure 23: The force-displacement curves for the SDS-beams.

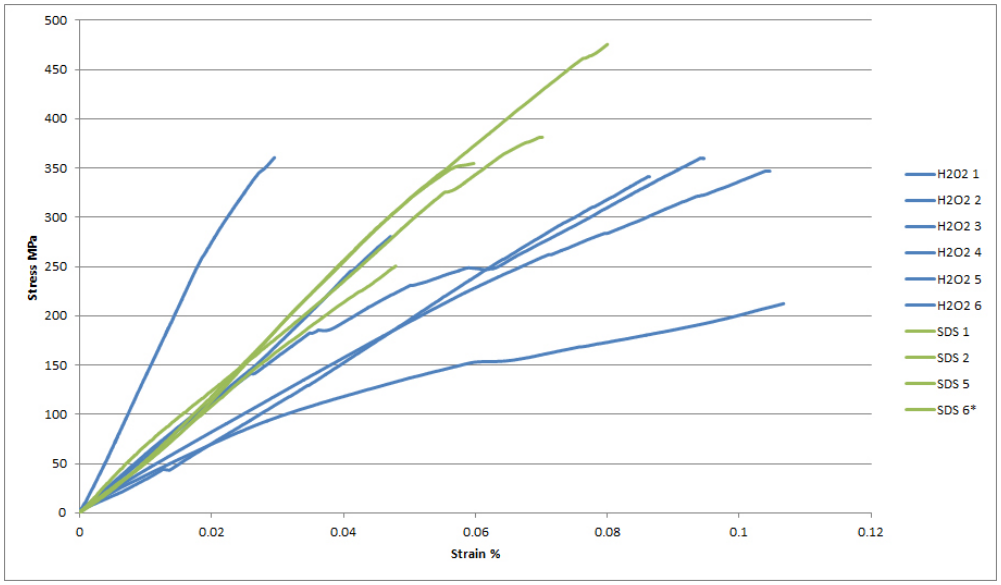

Figure 24: The stress-strain curves for the complete beams.

5 Discussion

In the this section the results will be interpreted and important observations and challenges will be addressed. The different analysis-methods will be presented and evaluated. A comparison between the experiments performed in this work and the modeling of biosilica performed at MiT will also be presented along with a discussion of further development. Finally, the results and a discussion of some initial FEM-modeling of diatom-beams will be presented in this section, as these are in a very early stage and were not performed by the author.

5.1 AFM-imaging

The AFM-study turned out to be a smaller part of the work than first expected. The frustules proved to be quite challenging to image with the AFM, and a lot of time went into placing the AFM-tip at a suited part of the frustule. When imaging the inside of frustules, i.e. a frustule in the concave position on the substrate, tip placement away from the center can result in pivoting of the frustule. If care is not taken with tip placement, the results may be noisy images or even loss of contact between the tip and the sample, resulting in no image at all. Only H_2O_2-cleaned frustules were used in the AFM-study. They were chosen because it was believed that the lower degree of organic matter would make these frustules easier to image with the AFM. Soft organic matter could lead to sticking of the AFM-tip and cover small features on the surface. The organic matter that could ruin the AFM-study comes from the cell, which used to be inside the frustule, and should not be confused with the organic constituents of the biosilica.

Initially, the plan for the AFM-study was to complement the SEM-images of the frustules with more accurate measurements of the surface of the diatoms. AFM-images are generally much more accurate in the z-direction, as SEM-images are generated from an interaction volume dependent on the initial energy of the electrons in the beam. The electrons penetrate the sample and generates secondary electrons from a certain distance from within the sample, normally ranging from 5-20 nm. This might not sound like much, but when the features of interest are at the same scale, the SEM does not give accurate information about the topography of the sample. The ultimate goal of the AFM-study was to visualize the smallest components of the biosilica, the smallest silicaspheres, and perhaps even the organic phase. Atomic force microscopy is a technique which requires a good deal of experience in order to obtain high resolution images, especially on rough surfaces, such as the frustules. Due to time-limitations and the decision to focus the work on the mechanical testing, the AFM-study were abandoned after just a few sessions. The images obtained during these sessions were of lower resolution than the SEM-images, and further improvement would have taken too much time to justify the continuation. A comparison between AFM-images and SEM-images of similar regions are shown in Figure 25.

Although the AFM-study was not performed as extensively as planned (a slight understatement), some important information can be extracted. It re-

veals that the cribellum layer really is at the outermost surface of the frustule. Although it appears clearly in the SEM-image, due to the nature of the signal in such images, we cannot trust that what is interpreted as the surface on such an image, really is the surface. Since the same pore-structure is observed in the AFM-image, we can conclude that this really is the surface of the frustule. This is important to confirm, as there has been reported diatom-species with the cribellum as the innermost layer.[11] The other vital information that can be extracted is the height of the lip on the foramen layer. The dimensions of these elevated edges might prove an important parameter for the mechanical properties, and correct measurements of these will be important when a model is developed.

The AFM should be used extensively in further work in order to measure the height of the foramen-lip and other key features important for the modeling of the diatom structure. Although the heights of a few lips were measured here, a larger number of measurements are needed to give a statistically sound value.

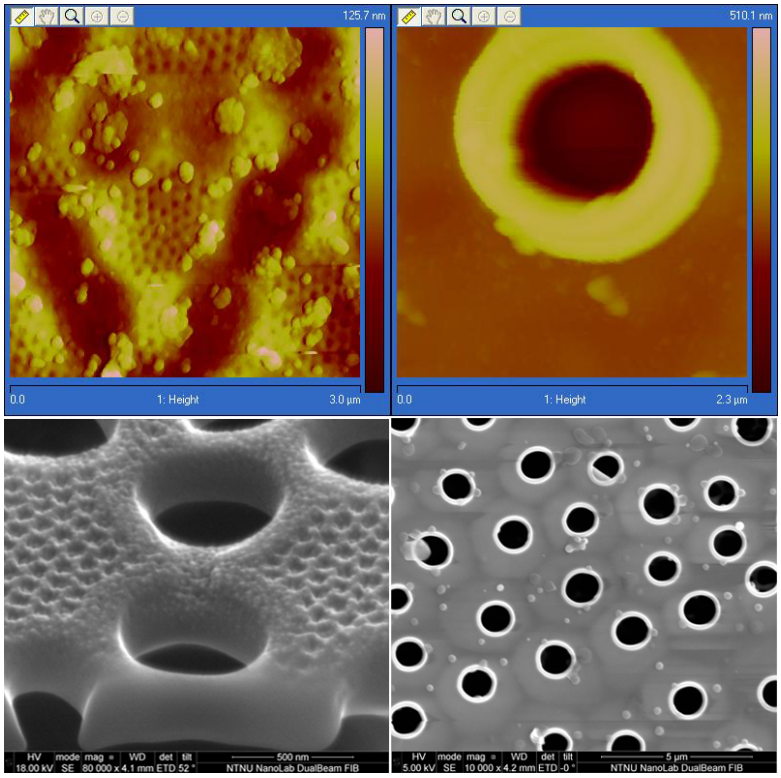

Figure 25: A comparison between topographical AFM-images (top) and SEM-images (bottom). To the left is the cribellum-layer and to the right is the foramen-layer in both cases.

5.2 Nanoindentation hardness testing

AFM-nanoindentation was considered, but this would require expensive non-standard tips, and more time for specialty training. Nanoindentation using the Hysitron was chosen as the author already had some experience with the equipment and because it is designed to perform the task. The cube-cornered tip was chosen as this was the closest match to the shape of the tip used by Losic et al. in their AFM nanoindentation study of a *Coscinodiscus* diatom, and would therefore lead to a better comparison of the results.[31]

The frustules were placed on an ordinary, uncoated glass slide. It was believed that the van der Waals forces between the frustule and the glass slide would be enough to keep them in place during scanning and indentation. However, it proved to be a challenge to find frustules that kept still during imaging with the indenter-tip. As with the AFM-imaging, a great deal of time was spent locating frustules that were in the concave position with the internal part of the frustule facing upwards. When such a frustule was found, it was scanned with the indenter-tip to make sure that there were no pivoting or movement induced by the tip. As often as not, the frustules that had a suitable configuration, still proved useless when they were scanned. The images showed clues that the frustule was moving along with the tip and the process had be done all over again with a different diatom. When a frustule in the concave position, which did not move during scanning, was found, several indents were made on the internal part of the frustule. As the Hysitron nanoindenter is not reliable at very low loads (below 50 μn), the indents were done with a set load of 200 μN. This turned out to be a little too high load as the sharp cubic tip caused cracking in the frustule, and even penetration through the foramen layer, which leads to inaccuracies in interpreting the results. As we can see from Figure 18 and 39, the apparent permanent deformation on the SDS-samples ranges from 200-1100 nm. The thickness of the layer the indents are performed on is about 300-500 nm. Any deformation above this suggests that the indenter has penetrated through the layer.

Looking at Figure 19, the frustules appear very different. The foramen holes are placed closer together for the H_2O_2-sample and the ridges between the holes are only observed in the SDS-sample. This indicates that we are dealing with different species of *Coscinodiscus*. The structure of the H_2O_2-sample has not been observed in the SEM and it appears that this particular frustule was chosen at chance with the nanoindenter. The diatom-sample provided from the Biological institute might include different types of *Coscinodiscus* species. The size of the indents seem very consistent for this H_2O_2-samples, while for the SDS-cleaned samples, the craters differ in size. No correlation with distance from the center or distance from holes are found, and a possible explanation for this behavior is that the indenter-tip is hitting just on top of the areola walls where the foramen has extra support, while fracturing the foramen whenever it is unsupported.

In addition to the cracking, a rather unusual and unexpected behavior was observed during nanoindentation of the frustules: The frustules undergo a rather

large deformation at low force, before what appears to be a strengthening mechanism occurs, and more force is required for further deformation. A peculiar feature with the strengthening behavior is that it appears to be reversible, and the opposite effect is seen on the unloading curve (see Figure 26). Such two-sloped behavior is often linked to strengthening effects, phase-transformation in crystalline behavior or probing of the substrate below when thin-films are tested. It is hard to say exactly what the cause is in this case, as we are dealing with an unpredictive, biological system. The most probable cause is believed to be the fact that the diatom is not flat. The side which is lying down against the substrate is curved (see Figure 27). The frustule might tilt slightly during testing, or an area of the frustule can be pushed down until it is in contact with the substrate. This suspicion is supported by the comparison of indent position and displacement shown in Figure 40 in Appendix A.1. Here it is seen that indents farther from the center of the frustule lead to a larger displacement than those located near the center. The two-slope behavior can also be a result of the structuring of the frustules. Losic et al. observed a similar type of behavior in their nanoindentation experiments with similar diatoms. They observed a two-sloped behavior when indenting on the cribellum layer and proposed that the behavior was caused by a collapse of the cribellum layer and that the second slope was due to probing of the underlying layer.[31] The onset of the second slope observed by Losic et al. was at a penetration depth of $\sim$ 50 nm and at a force of $\sim$ 0.5 μN, while the onset of the second slope observed in this case is at a penetration depth of 50-500 nm at force ranging from 20-70 μN. It is apparent that a closer investigation of the origin of this behavior is needed, but it is believed that tilting or pivoting of the frustule is the cause.

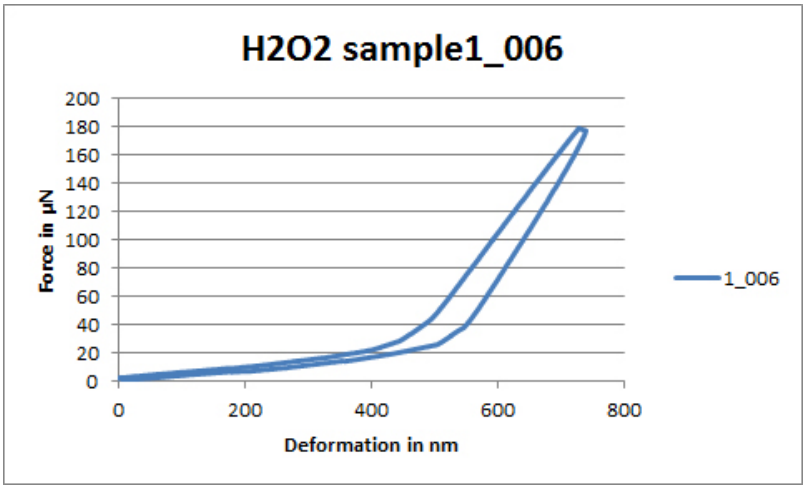

Figure 26: The force-displacement curve for a general H_2O_2-sample.

The two-sloped behavior lead to a problem with the analysis of the indentations. As mentioned in Section 2.6, the contact depth, h_c is used to calculate

Figure 27: A schematic cross-section of a *Coscinodiscus* sp. valve. The height difference of the inverted dome at the tip is exaggerated.

the contact area and thus the elastic modulus and hardness. The software on the Hysitron nanoindenter uses this theory, and estimates h_c from a fit of the unloading curve. For the example shown in Figure 26, the fit gave a contact depth of 574 nm. It appears from the force-displacement curve, that very little plastic deformation has occurred, and that the displacement is rather caused by tilting of the frustule (or whatever is causing the change in slope). As the software calculates the area of contact from the distance the tip has traveled into the sample, it is obvious that a contact depth of 574 nm will give an underestimate of the elastic modulus. The approach used here, to try to salvage some useful data from the results, is to choose a force larger than the force where the onset of the strengthening occurs and use the displacement difference between the loading and the unloading curve at this force as h_f, shown in Figure 9. This will give a slight overestimate of the elastic modulus, as it will result in a somewhat smaller contact area, but it is believed to be more accurate than the automatic calculations done by the software. The measured distance between the loading and the unloading curve at 30 μN, i.e. the plastic deformation, is 68.4 nm. Again from looking at Figure 9, it is clear that choosing h_f will give an overestimate of the elastic modulus, as the value is less than h_c. When estimating h_f from a set-force which is higher than zero, the value of h_f will be even smaller than it ideally would have been, without the two-sloped behavior. The results of the original and the corrected calculations for the H_2O_2-samples, where the two-sloped behavior was most pronounced, is shown Table 2. The real value for the elastic modulus will lie somewhere between the two extreme-values which is calculated with h_c, as fitted by the software, and h_f, as measured from a set-force. The correction method is more valid for the Young's modulus than the hardness value. As can be seen from Table 2 in the Appendix, the hardness values are artificially high. This is a result of an underestimate of the contact area, while the value for P_{max} is unchanged. The calculations of the Young's modulus is dependent on the square root of the contact area, so any error of the estimate of the contact area will be less for the Young's modulus than for the hardness. Additionally the Young's modulus is calculated with the stiffness of the material. This does not change with the correction method used. Therefore the corrections only apply to the Young's modulus, not the hardness. Although this method of interpreting the data is not trustworthy, it might give an indication of the correct value. Losic et al. found the Young's modulus to be 15.61 $\pm$ 5.13 GPa. The average Young's modulus for the H_2O_2-samples found here is 1.03 $\pm$ 0.3 GPa for the uncorrected data and 4.01 $\pm$ 1.48 GPa for the

corrected data. A lower value is expected as the indentations are performed with a much larger tip, but the uncorrected values seem improbably low. In a scientific context, however, the nanoindentation values for the Young's modulus and hardness found herein are not valid. There are too many uncertainties in the experiments. Due to these uncertainties, no conclusion can be drawn regarding the chemical treatments impact on the mechanical properties based on the nanoindentaion data. Improvements are suggested in Section 7.

Indentations with a Berkovich tip were also attempted, in order to avoid cracking or penetration of the foramen, but the high angle tip did not leave any visible marks in the diatom frustule. This is because the area of a high angle tip increases a lot with increasing indentation depth, and also due to the tilting of frustules. No results were obtained from these experiments.

The analysis method used in the Hysitron software is based on the multi-point unload method developed by Oliver and Pharr. A quick comparison with the single-point unload method developed by Field and Swain shows that the differences between the methods are negligible in this case. The single point unload method yields slightly smaller values for the h_c and subsequently slightly higher values for the hardness and E-modulus, but the variations are around 1 % for h_c (calculations are not shown).[29]

5.2.1 Nanoindentation hardness test of steel substrate

The reason for performing nanoindentations on the steel substrate was not to get a very accurate value of the E-modulus and hardness of the steel, but to ensure that the steel was stiff enough to not affect the results of beam-testing. Compared to the values gained from the nanoindentation of the frustules, it appears that the steel has an E-modulus 50-100 times larger than the frustules, which should be sufficient to ignore the contributions from the sample holders on the beam-bending results.

The actual loads ranged from 230-2400 μN and the maximum depths of the indents ranged from 29-219 nm. The deviation from the set load of 400-4000 μN is explained by the feed-back signal, or lack of such, of the indenter. The indents were performed as open-loop load control. This means that the system does not measure the load during the test, but instead guesses beforehand that the set load should be reached at a certain depth. A load-control system will continue to load a sample until the set-load is reached, while an open-loop system is not able to correct for differences between the guessed value and the actual value.

5.3 Three-point bending test

Motivations for the test scheme: The test performed is a micro-version of a three point bending test. This test is chosen as it is the most feasible test with the equipment available. The Omniprobe installed in the FIB does not allow for rotation of the sample, only movement in the xyz-directions. This makes the fabrication of sample for other testing than compression or bending very difficult. Also, the nanoindenter used to load the specimens can only apply force

by pushing, not by pulling. If sample were to be exposed to tension, they would have to be manufactured in such a fashion that the need for precise rotation is necessary. Bending test are also a quite common approach for sample testing on micro-scale. According to a review article by Pantano et al. bending tests are used in 29 % of nano- and micromechanical testing (this result does not include nanoindentation which is by far the most common test), only beaten by tensile tests, which are used in 33 % of the test. Tensile test, although preferable as they provide more information, are challenging at best at this scale. The alignment of sample-specimens are crucial for correct results. Just a small misalignment will result in a non-uniform stress distribution. With brittle materials there are also problems with fractures induced by the gripping mechanisms. [32]

The tip chosen for the bending tests, was a rather sharp conical tip with a radius of 0.6 μN and with a 90°angle. Ideally the tests should have been performed with a wedge-shaped tip in order to distribute the load uniformly across the width of the beam. However, with the need of a surface scan before each test, a sharp tip was chosen in order to accurately locate the beams. The spherical tip will cause point-stresses which will further complicate accurate analysis of the results. This can be avoided with an in-situ experimental set-up.

The three point bending test was chosen as the main part of the test scheme as it is believed that this test is capable to capture the structural and hierarchical effects of the diatom frustule. The mechanical testing of diatoms that has been reported in literature has been nanoindentation of the biosilica itself or mechanical tests of the entire frustule.[4, 31, 33] The capabilities of the FIB to remove matter very accurately makes it possible to fabricate samples for bending tests from the different layers in the frustule-structure, and it was believed that it would be possible to observe the mechanical contributions from each layer by testing them individually as well as together. To the authors knowledge, no similar experiments have been performed on diatoms.

Initial testing and challenges: The initial loading of beams were performed and the load-displacement curve showed what appeared to be cracking behavior, see Figure 28. This suspicion was further supported by the image taken by the indenter probe, see Figure 29. The sample holder is visible and the beam appears to have fractured completely with only half the length remaining in the holder. A further investigation in the SEM showed that this was not the case. The beam had merely been pushed further into the sample holder, and out of reach for the scanning tip. A closer examination of the load-displacement curve also shows that the forces involved in displacing the beam a rather large distance are low. In addition, the unloading curve is showing a large degree of elastic behavior despite a displacement of almost 1 μm. This experience was used in later experiments where a few loading cycles at low loads were performed in order to ensure that the beam was situated at the bottom of the sample holder, and that the correct deflection was measured.

The travel-height of the transducer in z-direction is limited to 4 μm. The first samples produced had beams that were not level with the surrounding

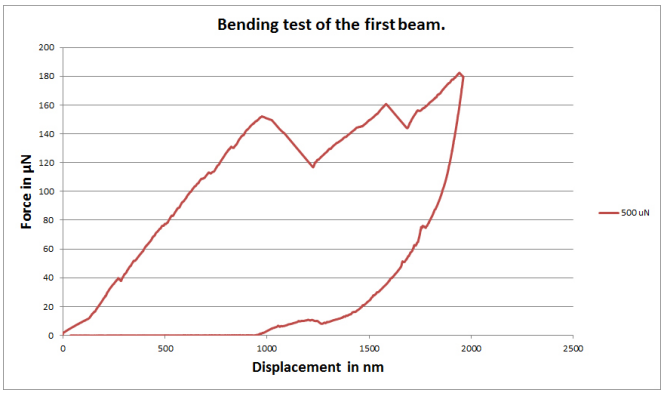

Figure 28: The force-displacement curve for the very first test in the steel-sample holder.

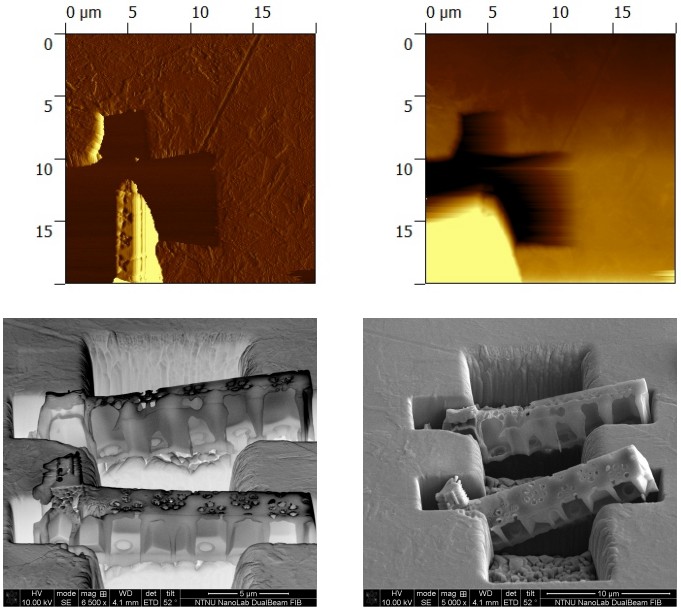

Figure 29: **Top left:** Gradient image of the beam after loading. **Top right:** Topographic image scanned with the indenter tip after loading. The frustule beam appears to be broken. **Bottom left:** SEM image of the beam before loading. **Bottom right:** SEM image of the beam after loading.

surface, but were 1-3 μm higher. This gave two challenges, the first being that this was on the limit of what the nanoindenter could handle in terms of height difference. The second challenge is that the three point bending test should be performed on free hanging samples. If the edges of the beam were to be fastened to the sample holder, the specimen would act much stiffer than compared to a free hanging sample and the stress distribution would be altered. The frustule beams were placed inside the sample holders and held in place by nothing but van der Waals forces. When the tip is scanned along the surface, the beams can be shifted or even removed from the sample holder. Both these problems could be avoided at a large degree, if there had been indentation equipment inside an SEM. With in situ observation of the test, the tip could be placed accurately on the sample without the need for scanning.

It turned out that with the need for scanning before testing, almost 50 % of the beams were lost, To combat this, the sample holders were made deeper and the beams were at a late stage of the testing attached to their holders with a small deposition of platinum.

Bending of complete beams: The force-displacement curves and the calculated stress-strain curves show that the biosilica the frustules are made from is a very brittle material. When testing brittle materials there will always be a certain spread in the results, as brittle materials are vulnerable to local defects in the structure. However, when looking at the stress-strain curves in Figure 24 there are especially two curves that show significantly deviating behavior from the rest of the group, namely the very stiff H_2O_2-beam 4 and the more compliant H_2O_2-beam 5. The high stiffness of H_2O_2-beam 4 is believed to be caused by a thicker foramen and areola than what is seen on the other samples, see Figure 30. The foramen is thicker close to the center of the diatom, as this is where the silica deposition vesicle initiates the valve production, and it is possible that this beam was fabricated from an area close to the center of the diatom. Unfortunately, no record of exact beam position were kept during this work. Every beam was fabricated within a certain distance from the center, but the exact position for the beams is not known. The calculated fracture stress was similar to the other beams, so it was only the stiffness that was affected by the increased thickness.

The explanation for the behavior of H_2O_2-beam 5 was more unclear, but it could be explained by the material that was stuck on the lower side of the foramen. Intuitively this would make the beam stiffer, but as can be seen in Figure 31 the piece of material seems to be attached loosely. In the same image it can be seen that the fracture in the foramen was at the end of the attached material and not directly underneath the indent-position. This suggests that the attached material has altered the stress-distribution for the beam allowing it to deform further. The fracture stress for this sample was also lower than the others. This could be caused by a local stress-enhancement caused by the attachment.

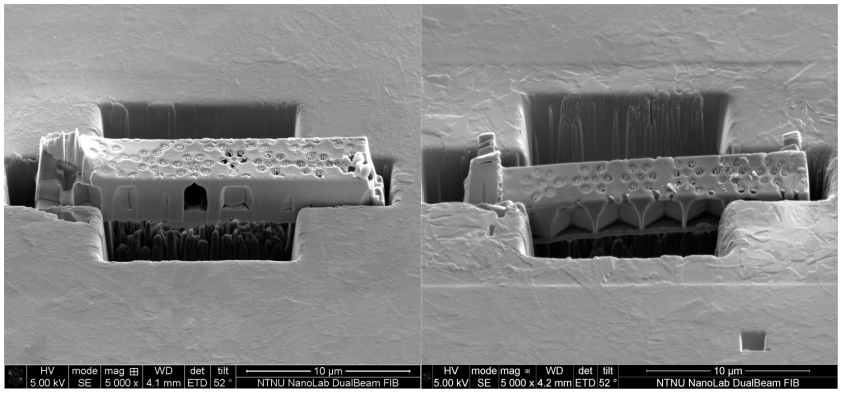

Figure 30: Two SEM-images comparing the thickness of the foramen layer between H_2O_2-beam 4 (left) and H_2O_2-beam 6 (right).

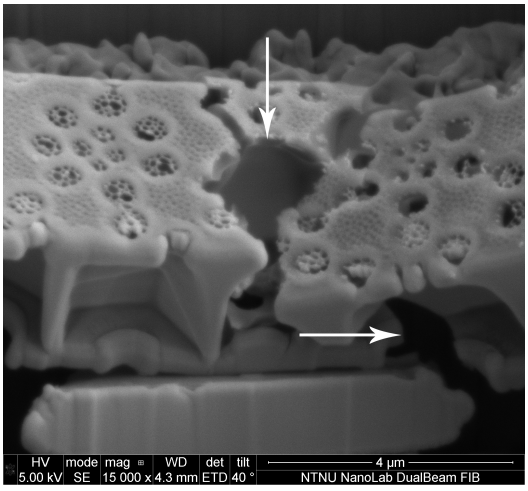

Figure 31: An SEM-image of H_2O_2-beam 5 after fracture. Note the position of the indenter tip and the fracture of the foramen marked with arrows.

Size of specimens: The specimen size was kept as similar as possible in order to obtain comparable results. An increase in specimen size would lead to a large increase in specimen preparation time, while a decrease in specimen size would lead to further challenges with the nanoindenter equipment. The effort were put into getting comparable results, and also compare the mechanical properties of the different layers, rather than to change the size of the specimens. This seemed to have payed off, when comparing the force-displacement curves to the stress-strain curves. The curves look rather similar, due to the similarity in size of the test specimens. Some difference in width of the samples occurred due to drift of the sample during fabrication. The similarity of the stress-strain curves and the force-displacement curves is an indication that although the calculated stress-strain curves may be wrong due to the simplifications in the analysis, the force-displacement curves can be used to some extent to compare the behavior of the different beams.

Bending of beams from the different layers: Only a few test of foramen- and cribrum-beams were successfully tested, as they too suffered from the problems with the indenter-scan. As can be seen from Figures 22 and 23 the force needed to fracture these beams are much lower than the complete beams (with one exception which will be explained later). It was considered to calculate the stress for these beams as well, but due to large uncertainties of the cross-sections this could not be done with trustworthy results. The sample stage in the FIB can only be tilted to 52°. This means that the samples made from the foramen layer will have a triangular shaped areola-structure with a height of more than 1 μm for a 3 μm wide sample. An image of the shape of such a beam can be seen in Figure 32. A different test scheme in order to calculate the fracture stress for the foramen layer is presented in Section 7.

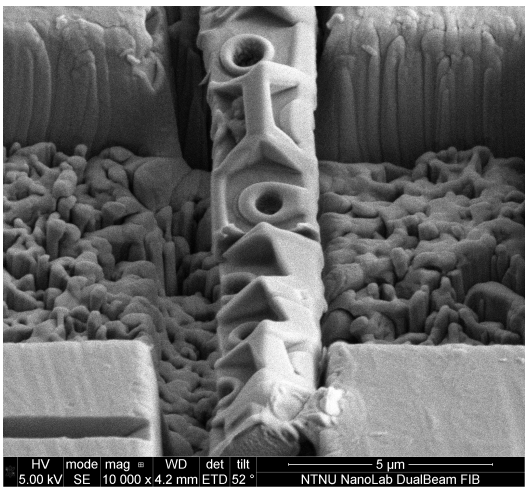

Figure 32: H_2O_2-beam 7 viewed from the side.

As mentioned, one of the foramen beams, SDS-beam 7, required a load of $\sim$ 400 μN in order to fracture. The other specimens from foramen or cribrum layers required forces below 150 μN. The reason for this is apparent in Figure 56 in Appendix B.2. It appears that the valve the sample was taken from, had collapsed onto a second valve, and these two were fused together during the FIB-milling. This was discovered when the beam was lifted out of the frustule, and as the sample preparation time was about 3 hours per sample, it was decided to test the beam even if the results would be hard to analyze. SDS-beam 6 was taken from the same frustule, and the same thing happened here, but the results seemed to be less affected for the complete beam.

Platinum fastened beams: To combat the problems with the beams being removed from the holders, the beams were attached to the holders with a deposition of platinum. These attachments can be seen in Figures 46-51 and Figures 54-58 in the Appendix. The implications of these attachments on the mechanical properties or on the test itself is not known as some of the tests with platinum depositions show very similar results as the tests without (for example H_2O_2-beam 6), while some show results which are hard to interpret (H_2O_2-beam 8). A further investigation, preferably with an in-situ experimental set-up must be performed in order to evaluate the effects of these attachments.

Comparison of the cleaning methods: Surprisingly, it appears as if the SDS-cleaned samples are stiffer than the harsher H_2O_2-cleaned samples. The biosilica appears very brittle for both the treatments, but the SDS-cleaned frustules fracture at lower strains. This was the opposite result than what was expected as it is the H_2O_2-cleaned samples which are disassembled and fractured when observed after the treatment. It is clear that the number of samples tested here is too low in order to be sure of this trend and a lot more testing is required, but the difference in the number of broken frustules between the two cleaning-methods were so large that it was expected a very clear trend. The reason for the increased brittleness of the SDS-cleaned frustules needs further investigations.

A possible explanation for the disassembled H_2O_2-frustules is that the organic matter which is removed in the cleaning treatment is located externally in the connections between the valves and the girdle bands, and not as a part of the biosilica itself. The girdle bands are much softer than the valves and may act as a kind of shock absorber. When the organic "glue" between the valve and girdle-band is removed the frustules are disassembled and the softer girdle-bands can no longer protect the valves, which fracture more easily on impact due to their brittle nature. The fracture strength for the two cleaning methods are found to be similar with an average value of 365 $\pm$ 92 MPa for the SDS-samples and 316 $\pm$ 59 MPa for the H_2O_2-samples. The variations show that a larger number of samples are needed to tell whether the fracture stress for SDS-samples really is higher, or if the difference is just a result of the scatter of brittle materials. In both cases, the fracture stress is well above the fracture

stress for fused silica which is reported to be 110 MPa.[34, Ch.8] This in itself is quite remarkable and a strong indication that the diatom has found a clever way to create structures from silica. Whether this increased strength is a result of the hierarchical structure or a feature of the composite between silica and organic constituents is not yet known.

5.4 Comparison of experiments and modeling

The experimental part of the mechanical characterization is the main part of this work. However, the evaluation of the results from this part can be quite difficult as the material considered is highly inhomogeneous. The evaluation of Young's modulus of diatom frustules has been done by imitating experimental results with FEM-simulations. Hamm et al. found the E-modulus of the girdle band from a *T. punctigera* diatom by compressing the girdle band with a calibrated glass needle. The same experiment was then modeled with the finite element method (FEM) using plate elements. The model was subjected to the same load as the actual experiment and the E-modulus was modified until the deformation as a function of load were identical with the observations done in the experiment. [4]

Atomistic modeling: For atomistic modeling there is a need for a potential function to calculate the inter-atomic behavior. This potential function is a mathematical description of the different forces that act on the atoms in the model. These potentials are based on quantum mechanical calculations and experimental measurements, if such are available. Potentials with very good results exists for pure materials such as iron, copper, gold, silicon and more. The development of potentials become far more difficult when we are considering alloys or mix of different materials. As the systems described become more advanced, the computer-power required for the calculations also increase drastically. With pure materials it is easier to simplify the calculations in order to make them more time-efficient. However, there exist potentials for more complex materials such as SiO_2. Leon Dimas and Marcus Buehler at MiT in Boston are exploring models based on composites of bulk and nanoporous silica. They are continuing the work based on the previous work of Buehler, Garcia and Sen as described in Section 2.2.[19, 21, 35] They have created honeycomb-like structures of crystalline silica with pore and wall-sizes in the range of 1-7 nm. The small scale is partly to study the effect of pores on the mechanical properties and partly due to practical issues concerning computer-time: Any larger system would require immense computer-power to simulate. The results showed that wall-sizes under 4 nm gave rise to an increased ductility in the silica, at the expense of stiffness.

The observant reader will already have marked two important differences between these models, and the biological silica considered in this work. First, the biosilica is amorphous, not crystalline, and second the smallest wall-size found in the diatoms are on the order of tens of nm. It is apparent that the models of Buehler were never intended to be an exact replication of the actual biosilica,

but rather to investigate principles that might be valid at other size-scales as well. However, it might be possible to perform direct atomistic simulation of the area where the crack is initiated. This is a way to limit the model-size in order to carry out detailed atomistic simulations of crack propagation. In order to compare the results from the experimental testing performed in this work with computational simulations, and to capture the hierarchical effects of the entire structure, a different approach must be taken. The complexity of the structure makes simplifications on the geometry difficult. The experimental testing shows that the different layers greatly influence the mechanical properties. The approach used by Hamm et al. seems like a promising way to obtain a 1:1 ratio of experiments and simulations, where the properties of the model can be tuned to fit the experimental result. Testing of geometries which are easier to analyze would ease this work, and will be discussed further in Section 7.

Initial FEM-simulations: Are Moa Gausen, a fellow master-student, has performed some initial FEM-simulations of a dimensionless, generic brittle material with the same shape as the diatom-beams, both with and without the porous structure of the top and bottom layer, see Figure 33. The simulations were done to investigate the effects of the pores on the overall mechanical properties of the beam. The model was made as a representation of the three-point bending tests performed in the experiments, with some simplifications: half the length of the beam were modeled with the same relative dimensions of the features as observed from the *Coscinodiscus* sp. The beam were fastened in one end and a load was applied at the other end. This is equivalent to half of a three-point bending test and, assuming such a test is symmetric, it is a good approximation.

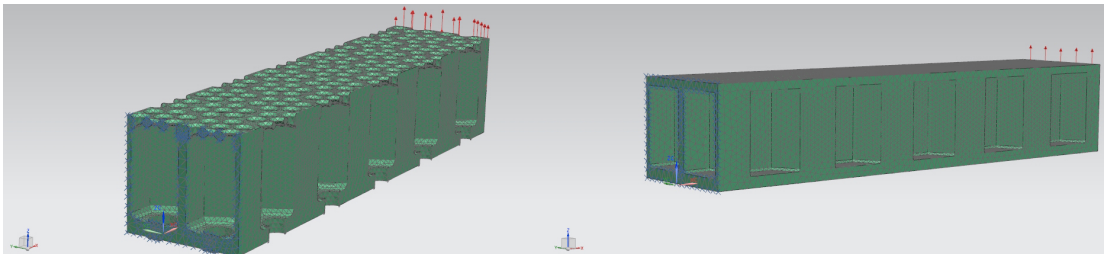

Figure 33: The mesh for the beam-structure with holes (left) and without (right).

The results show that the beam without the holes is a lot stiffer than the beam with the holes. The beam with the holes where deformed close to 50 % more at the same force. This is an important result as it shows that the porous structure enables the frustule to deform more without increase in stress, similar to the observations by Buehler et al. Although there is no ductility observed in these experiments, the pores clearly influence the mechanical properties of the material. The reduction in stiffness is consistent with the experimental results,

where the flexural modulus for the complete beams were found to be 5.72 $\pm$ 2.90 GPa, which is relatively low. It is also seen in the simulations that the point of impact for a load greatly effects the results. If the load is placed on top of a pore of the top layer, without hitting a hexagon it will lead to large local stresses and most likely lead to a fracture. However, if the load is placed on top of a honeycomb, the stress will be spread over a much larger part of the beam, and even to neighboring hexagons, see Figure 34 for a comparison. This result is supporting the explanation for the large differences in the nanoindentation test-results of the SDS-cleaned frustules.

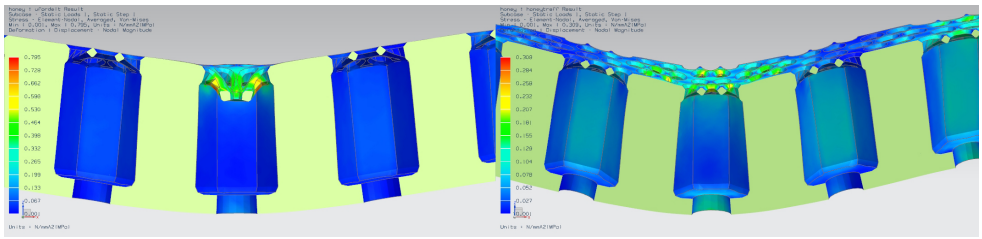

Figure 34: A comparison of a loading on the pore area (left) and the honeycomb (right). Notice the large local deformation in the left image, while the stress is spread over a much larger area in the right image.

Finally, the stress-distribution for the bending simulation show very little stress-enhancement for the holes in the foramen, normal to the width of the beam, see Figure 35. This is consistent with the testing, where fracture seems to have initiated from both the holes and through the width of the beam where no holes are situated. The circular shape of this pores minimizes the stress-enhancement and reduces the chance of fractures initiating from them. The effects of the raised edge around them needs to be further investigated. From the testing, the large stress just below the indenter-tip seems to be the cause of fracture, rather than stress enhancements at the foramen holes.

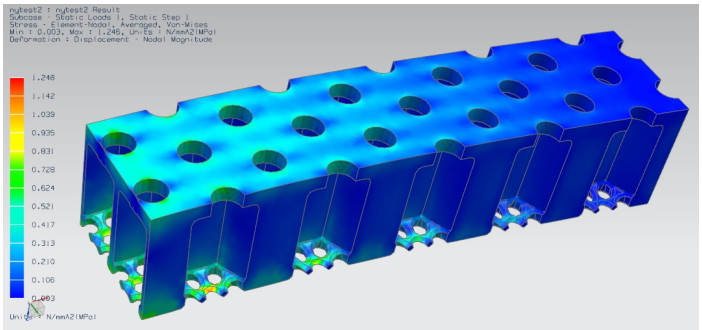

Figure 35: The stress-distribution for the foramen-layer during a bending test. Small stress-enhancements beside the holes are seen.

6 Conclusion

A method to test the mechanical properties of diatoms has been developed. The method is a three-point bending test with a custom-made steel sample holder. The sample holders had an unsupported span of 12 μm. The bending-specimens are beams fabricated out of selected parts of the frustule with a focused ion beam and subsequently tested in a nanoindenter. The fabricated beams had lengths of 20-22 μm, widths of 3-3.5 μm and heights depending on the specific diatom it was fabricated from. The FIB was also capable of fabricating test specimens from the individual layers of the frustule. The method can capture both the mechanical properties of the individual layers, and the mechanical properties of the combined structure, a capability which, to the authors knowledge, has not been reported before. Single beams fabricated from the whole frustule was subjected to loads as high as 1040 μN before fracturing, while beams from the foramen layer fractured at loads below 150 μN.

A comparison between the mechanical properties of frustules cleaned with a soft and harsh chemical treatment has been done. The SDS-cleaned frustules appeared to fracture at lower strains, which was in stark contrast to what was expected. The number of samples tested was too low for the result to be conclusive, and further investigation is needed. It has been shown that the force required to break a beam made from the entire frustule was 4-10 times larger than a beam from the foramen layer. Initial stress-calculations shows that the fracture stress of the biosilica regardless of cleaning treatment is 336 ± 73 MPa and the flexural modulus is 5.72 ± 2.9 GPa. This is 3 times the fracture stress for amorphous fused silica.

Early stage FEM-simulations of frustule beams under load has been performed and the contributions of the porous structure to the mechanical properties has been investigated. This initial modeling has shown that the pores greatly reduce the stiffness of the frustules, but do not cause any major stress-enhancements. It also supports the experimental findings that the areola is a main load-bearing part of the structure.

It is clear that the diatom has developed a clever way to create its glass-armor. The honeycomb structure of the areola provides increased stiffness and a large increase in the load-carrying capabilities of the frustule, at the cost of very little material. The biosilica is shown to be less stiff, yet stronger than ordinary silica, but the ductile aspect, which has been observed in atomistic modeling of nanoporous silica, is not present in the diatom biosilica.

7 Further work

This section will address improvements and new strategies for the work described herein. The main focus will be on the cooperative development of computational models and experimental methodology.

7.1 AFM-study

As the AFM-study during this work turned out to be less extensive than expected, a more detailed study of the dimensions of important features should be conducted. As mentioned in Section 5, the AFM is far more accurate in the z-dimension most known characterization-techniques. The dimensions of the lip around the foramen holes should be measured for a large number of different diatoms, so the measurements are statistically valid. Imaging of fabricated beams, both complete and from the different layers could give accurate and valuable information about the dimensions which are used to calculate the cross-section of the beams. The more accurate the dimension-data is, the more accurate the analysis of the stress-values will be. In addition, high-resolution AFM-imaging of crack-surfaces could lead to information about the composite nature of the biosilica, but might prove very challenging to achieve.

7.2 Nanoindentation hardness test

The nanoindentation test should still be performed in order to obtain values that are comparable to literature values. In order to combat the problems with the frustules tilting and moving during testing, the substrate should be coated with a positively charged film, for example polylysine. This will passivate the frustules and make the experimental procedure easier. AFM-nanoindentation should be considered as the forces involved are much lower, reducing the risk of tilting, cracking and penetration through the layers. As the literature values found for diatoms are results of AFM-nanoindentations, it will also be beneficial to have equal testing procedures to obtain comparable values.

7.3 Experimental methodology and model development

It has been shown that the three point bending test can, in principle, be used successfully for diatom-testing. The analysis of the results are, however, challenging. This is partly due to the complexity of the structure, and partly due to uncertainties in the material properties itself. The analysis done herein is based on very simplified calculations and rough estimates of the dimensions of the cross-sections. The analysis of the intricate structure could be easier with the help of an finite element model, but such a model would need accurate inputs for the material properties. With an experimental set-up with a nanoindenter placed inside the FIB or an SEM, the need for scanning would be eliminated and the need for the groove in the sample-holders would disappear. Such a set-up would grant a much better positioning of the load, and a wedge-tip, rather

than a spherical tip could be used to apply the load, ensuring a more uniform stress-distribution. The following paragraphs describes a possible approach to get more accurate measures for the dimensions of the beams, and to make beams with cross-sections more suited for analysis.

Smaller test specimen: In order to obtain more accurate material properties, it is here proposed to make a beam with massive rectangular cross-section from a part of the frustule which does not contain any pores. The sample will be significantly smaller than the beams used earlier in this work, but should be possible to produce. The limiting factors so far has not been the sample-preparation part, but rather the positioning and testing with the nanoindenter. With an in-situ set-up with a high-aspect ratio tip the loading of such a sample should be straightforward to perform. The beams made from the foramen layer did also suffer from the angle of the ion beam, which left parts of the areola on the beam. This made the analysis difficult as the cross-section is unknown. With a smaller beam, this effect can be greatly reduced, and with clever choice of positioning, the areola parts can be minimized.

A tentative schematic of such a sample is shown in Figure 36. Such a beam could be produced with a smooth, curved transition to a larger area of the frustule in order to avoid stress-enhancement. This larger part of the frustule can easily be attached to the tungsten needle in the FIB and attached to a substrate. The loading can either be performed as a three-point bending test or as a beam-deflection test. The analysis of a rectangular massive beam is much simpler than the complex structures of the complete beam and the foramen with triangular areola parts attached. The beam can even be used in combination with pre-fabricated notch in order to get information about the toughness. With more accurate measurements of the actual material properties, more accurate models can be made. Atomistic models with potentials for crystalline or amorphous SiO_2 can be used in small volumes around crack-tips and compared with the biosilica. FEM-modeling of the beam-bending can be performed and adjusted so the deflection as a function of load fits the experiments, or with inputs from the results of the atomistic simulations. If the beams can be made small enough, and perhaps tested with an AFM-tip it might be possible to reach a 1:1 relationship between the experiments and pure atomistic modeling.

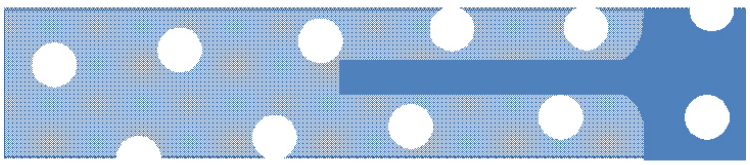

Figure 36: A schematic drawing of a proposed beam-structure for testing. A comparison with a beam used in this work is shown.

Improved analysis: The values for the fracture stress found in this work is based on very simplified analysis of the diatom structure. If the testing and modeling of the smaller specimens turn out to be successful, the values for the fracture stress found for these samples can be used to correct the analysis for the entire beams. As it is the foramen part of the beam which is put in tensions during a bending test, the fracture stress for the complete beam should be the similar to the fracture stress for a foramen beam. With accurate information of the intrinsic material properties of the biosilica, based on these new experiments, the further analysis, either with atomistic modeling or FEM-modeling can be fitted to match the experiments. This would ease the investigations of the effects of the hierarchical structure on mechanical properties. As the initial modeling has shown, the apparent properties of the material is greatly influenced by the porous structure, and as experimental results of simple structures are scarce the test described above would provide valuable data for further investigations of biosilica. A further comparison of the effects of chemical treatment should also be conducted, as a large number of tests are required to separate the inherent scatter of brittle materials from actual differences of the mechanical properties.

References

[1] S. Weiner and H. D. Wagner. The material bone: Structure mechanical function relations. *Annual Review of Materials Science*, 28:271–298, 1998.

[2] Z. H. Xu and X. D. Li. Deformation strengthening of biopolymer in nacre. *Advanced Functional Materials*, 21(20):3883–3888, 2011.

[3] S. Keten, Z. P. Xu, B. Ihle, and M. J. Buehler. Nanoconfinement controls stiffness, strength and mechanical toughness of beta-sheet crystals in silk. *Nature Materials*, 9(4):359–367, 2010.

[4] C. E. Hamm, R. Merkel, O. Springer, P. Jurkojc, C. Maier, K. Prechtel, and V. Smetacek. Architecture and material properties of diatom shells provide effective mechanical protection. *Nature*, 421(6925):841–843, 2003.

[5] J. D. Currey. Materials science - hierarchies in biomineral structures. *Science*, 309(5732):253–254, 2005.

[6] Sindre H. Bjørnøy. *Diatom Nanocomposites, The mechanical properties of silica shells from diatoms.* Project work, Norwegian University of Science and Technology, 2011.

[7] Solbiopta. http://www.ntnu.edu/biotechnology/envbiotek/projects.

[8] T. Fuhrmann, S. Landwehr, M. El Rharbi-Kucki, and M. Sumper. Diatoms as living photonic crystals. *Applied Physics B-Lasers and Optics*, 78(3-4):257–260, 2004.

[9] D. Losic, J. G. Mitchell, and N. H. Voelcker. Diatomaceous lessons in nanotechnology and advanced materials. *Advanced Materials*, 21(29):2947–2958, 2009.

[10] D. Losic, R. J. Pillar, T. Dilger, J. G. Mitchell, and N. H. Voelcker. Atomic force microscopy (afm) characterisation of the porous silica nanostructure of two centric diatoms. *Journal of Porous Materials*, 14(1):61–69, 2007.

[11] M. S. Hale and J. G. Mitchell. Functional morphology of diatom frustule microstructures: hydrodynamic control of brownian particle diffusion and advection. *Aquatic Microbial Ecology*, 24(3):287–295, 2001.

[12] Nils Kroeger and Manfred Sumper. Diatom cell wall proteins and the cell biology of silica biomineralization. *Protist*, 149(3):213–219, 1998.

[13] Tadashi Nakajima and B. E. Volcani. 3,4-dihydroxyproline: A new amino acid in diatom cell walls. *Science*, 164(3886):1400–1401, 1969.

[14] M. Sumper and E. Brunner. Learning from diatoms: Nature's tools for the production of nanostructured silica. *Advanced Functional Materials*, 16(1):17–26, 2006.

[15] N. Poulsen and N. Kroger. Silica morphogenesis by alternative processing of silaffins in the diatom thalassiosira pseudonana. *Journal of Biological Chemistry*, 279(41):42993–42999, 2004.

[16] N. Kroger, R. Deutzmann, and M. Sumper. Polycationic peptides from diatom biosilica that direct silica nanosphere formation. *Science*, 286(5442):1129–1132, 1999.

[17] A. M. M. Schmid and D. Schulz. Wall morphogenesis in diatoms - deposition of silica by cytoplasmic vesicles. *Protoplasma*, 100(3-4):267–288, 1979.

[18] M. Sumper. A phase separation model for the nanopatterning of diatom biosilica. *Science*, 295(5564):2430–2433, 2002.

[19] A. P. Garcia, D. Sen, and M. J. Buehler. Hierarchical silica nanostructures inspired by diatom algae yield superior deformability, toughness, and strength. *Metallurgical and Materials Transactions a-Physical Metallurgy and Materials Science*, 42A(13):3889–3897, 2011.

[20] Adri C. T. van Duin, Siddharth Dasgupta, Francois Lorant, and William A. Goddard. Reaxff: A reactive force field for hydrocarbons. *The Journal of Physical Chemistry A*, 105(41):9396–9409, 2001.

[21] A. P. Garcia, D. Sen, and M. J. Buehler. Mechanics of nano-honeycomb silica structures: A size-dependent brittle-to-ductile transition. *Journal of Nanomechanics and Micromechanics*, 1(4), 2011.

[22] D. Sen and M. J. Buehler. Atomistically-informed mesoscale model of deformation and failure of bioinspired hierarchical silica nanocomposites. *International Journal of Applied Mechanics*, 2(4):699–717, 2010.

[23] M. H. F. Overwijk and F. C. Vandenheuvel. A macroscopic model for focused-ion-beam-induced deposition. *J. Appl. Phys.*, 74(3), 1993.

[24] Nan Yao. *Focused Ion Beam Systems: Basics and Applications*. Cambridge University Press, Cambridge, 2007.

[25] L.A. Giannuzzi and F.A. Stevie. *Introduction to focused ion beams: instrumentation, theory, techniques, and practice*. Springer, 2005.

[26] Nader Jalili and Karthik Laxminarayana. A review of atomic force microscopy imaging systems: application to molecular metrology and biological sciences. *Mechatronics*, 14(8):907–945, 2004.

[27] D. Brandon and W.D. Kaplan. *Microstructural Characterization of Materials*. John Wiley & Sons, 2008.

[28] W. C. Oliver and G. M. Pharr. An improved technique for determining hardness and elastic-modulus using load and displacement sensing indentation experiments. *Journal of Materials Research*, 7(6):1564–1583, 1992.

[29] Anthony C. Fischer-Cripps. *Nanoindentation*, volume 1. Springer New York, 2011.

[30] R. C. Hibbeler and S. C. Fan. *Mechanics of materials*. Prentice Hall, Singapore, 2011. 8th ed. in SI Units.

[31] D. Losic, K. Short, J. G. Mitchell, R. Lal, and N. H. Voelcker. Afm nanoindentations of diatom biosilica surfaces. *Langmuir*, 23(9):5014–5021, 2007.

[32] M. F. Pantano, H. D. Espinosa, and L. Pagnotta. Mechanical characterization of materials at small length scales. *Journal of Mechanical Science and Technology*, 26(2):545–561, 2012.

[33] N. Almqvist, Y. Delamo, B. L. Smith, N. H. Thomson, A. Bartholdson, R. Lal, M. Brzezinski, and P. K. Hansma. Micromechanical and structural properties of a pennate diatom investigated by atomic force microscopy. *Journal of Microscopy*, 202:518–532, 2001.

[34] D.W. Richerson. *Modern ceramic engineering: properties, processing, and use in design*. CRC Taylor & Francis, 2006.

[35] A. P. Garcia and M. J. Buehler. Bioinspired nanoporous silicon provides great toughness at great deformability. *Computational Materials Science*, 48(2):303–309, 2010.

Appendix

A Nanoindentation

A.1 Nanoindentation of frustules

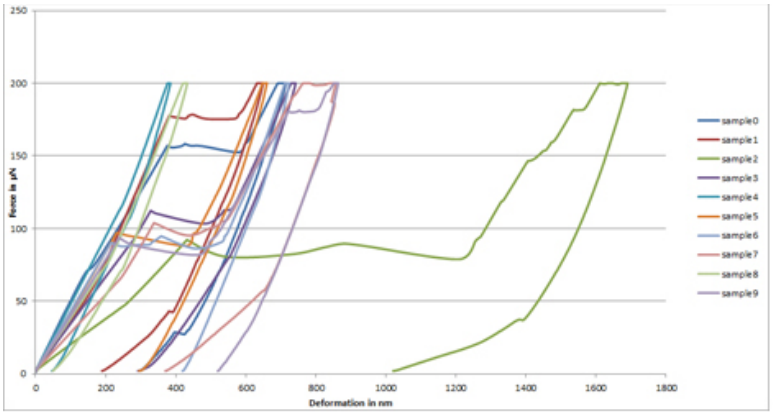

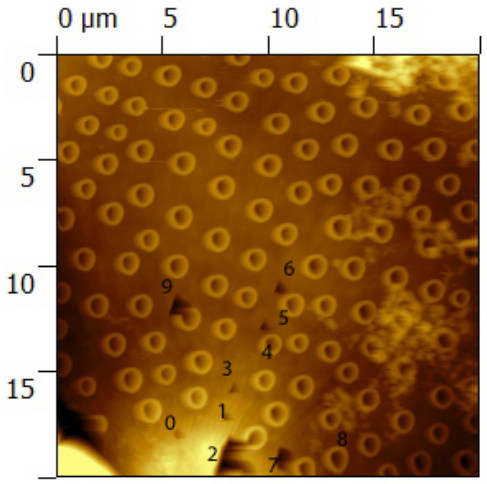

Figure 37: The force-displacement curves of SDS-sample 1 and the corresponding scan of the area after indentation.

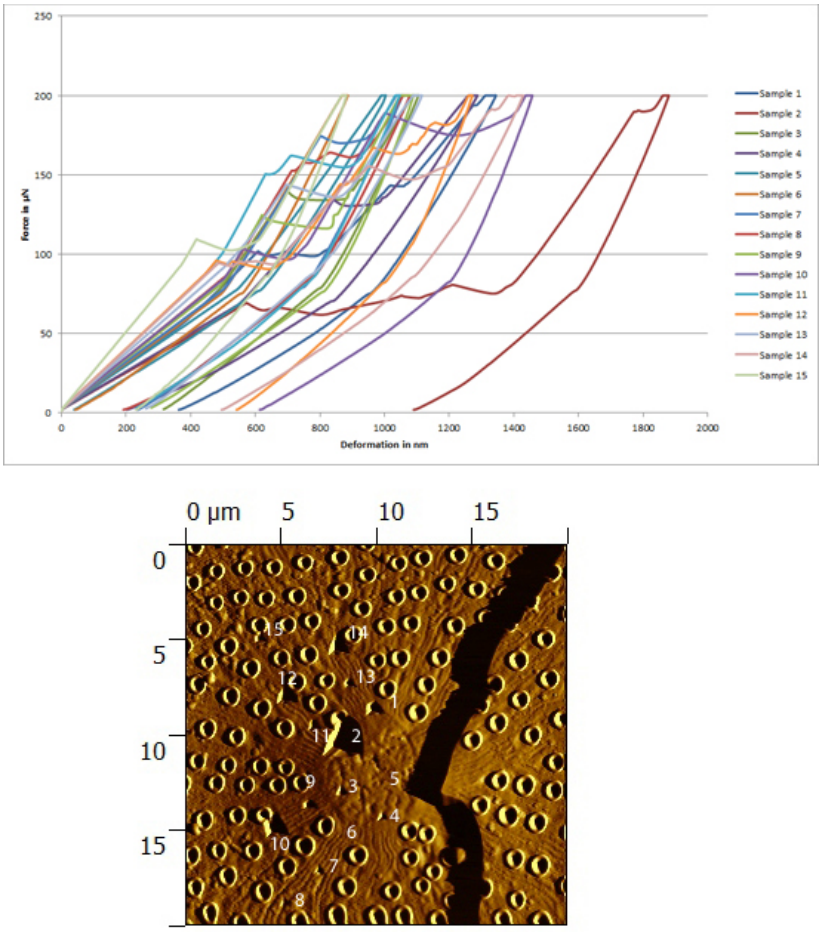

Figure 38: The force-displacement curves of SDS-sample 1 and the corresponding scan of the area after indentation.

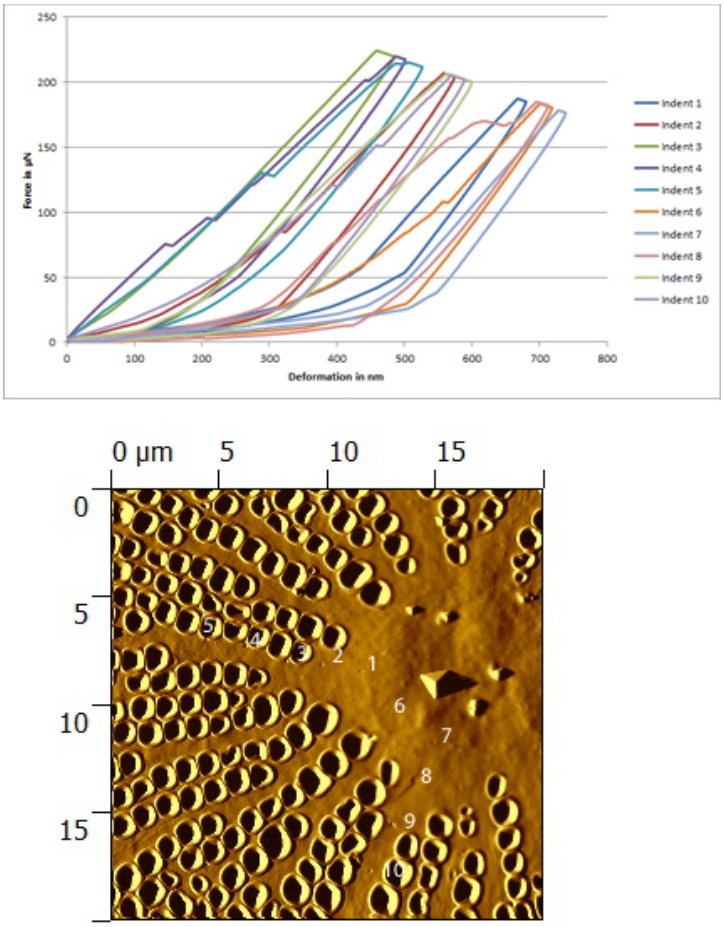

Figure 39: The force-displacement curves of H_2O_2-sample 1 and the corresponding scan of the area after indentation.

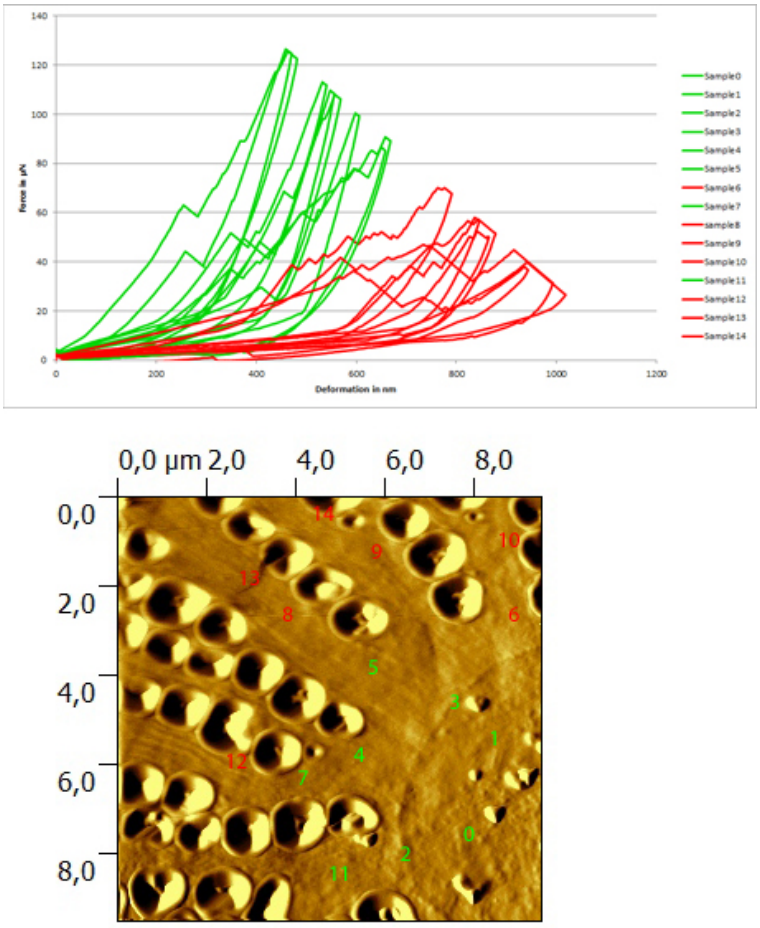

Figure 40: The force-displacement curves of H_2O_2-sample 4 and the corresponding scan of the area after indentation. The numbers and graphs are colored-coded related to their distance from the center of the frustule. Apparently, a larger distance from the center gives a larger displacement. This is an indication that the frustule is pivoting during loading.

Table 2: Table showing the results from the nanoindentation experiments of the H_2O_2-cleaned frustules. h_c refers to the values found by the software, h_f refers to the values found using the correction method described in Section 5.2

Sample	E_r h_c (GPa)	E_r h_f(GPa)	H h_c(GPa)	H h_f(GPa)	Base line (μN)
1_1	0.78	6.88	0.17	9.57	50
1_2	1.07	3.79	0.28	3.00	30
1_3	1.11	3.65	0.64	6.25	20
1_4	1.07	3.33	0.55	4.86	20
1_5	1.01	3.28	0.43	4.00	20
1_6	0.63	2.51	0.15	2.03	30
1_7	0.61	6.31	0.14	12.05	30
1_8	0.67	2.60	0.15	1.91	30
1_9	0.80	2.83	0.29	3.02	30
1_10	0.82	2.24	0.31	1.91	30
4_1	1.07	3.72	0.21	2.12	20
4_2	0.78	2.80	0.09	0.94	20
4_3	0.93	2.39	0.20	1.28	20
4_4	0.95	4.33	0.12	1.98	20
4_5	0.81	3.38	0.14	1.97	20
4_6	0.83	4.07	0.11	2.18	20
6_1	1.88	6.23	0.93	8.88	20
6_2	1.33	7.84	0.45	11.13	40
6_3	1.61	3.27	0.67	2.40	20
6_4	1.14	4.67	0.25	3.60	20
6_5	0.82	5.24	0.17	5.80	20
6_6	1.27	5.56	0.37	6.05	22
6_7	1.53	3.45	0.56	2.45	20
6_8	1.07	3.74	0.26	1.62	65
6_9	1.55	4.29	0.61	4.01	20
6_10	0.80	1.94	0.20	1.05	20
6_11	1.09	5.43	0.44	9.88	20
6_12	0.81	3.82	0.19	3.83	20
6_13	1.84	5.79	1.45	13.16	20
6_14	0.79	4.12	0.17	4.12	20
6_15	0.81	1.93	0.21	1.07	20
6_16	0.92	2.78	0.24	1.99	20
6_17	1.06	2.52	0.31	1.60	20
6_18	1.41	5.42	0.78	10.63	20

A.2 Nanoindentation of steel substrate

Table 3: A table showing the results from the nanoindentations in the steel substrate.

Sample nr	Load	Er (GPa)	H (GPa)
1	230	178.26	5.69
2	320	155.83	4.67
3	412	169.69	5.25
4	503	158.25	6.00
5	594	159.63	5.29
6	685	157.89	5.28
7	776	160.62	5.26
8	868	156.34	6.03
9	959	170.64	5.77
10	1051	172.13	6.07
11	1140	154.66	5.07
12	1234	165.63	6.23
13	1323	153.09	5.09
14	1415	154.24	5.41
15	1510	179.82	6.77
16	1599	151.71	5.82
17	1691	162.68	5.72
18	1784	170.42	6.11
19	1875	159.17	6.03
20	1967	160.74	6.08
21	2057	163.38	5.71
22	2150	174.54	5.74
23	2242	170.89	5.90
24	2334	158.08	6.17
25	2426	156.78	5.94

B Three point bending test

Table 4: A table showing the results from the three-point bending tests including stress calculations for rectangular cross-section and I-beam cross-section.

Sample	Max load (μN)	Max z (μm)	σ_{max} I-beam (MPa)	E_{flex} I-beam (GPA)	σ_{max} ■-beam (MPa)	E_{flex} ■-beam (GPa)
SDS 1	697	0.47	355	6.34	226	4.05
SDS 2	1041	0.63	475	6.38	299	4.01
SDS 5	363	0.63	250	5.60	180	4.02
SDS 6	726	0.53	381	5.83	258	3.95
H_2O_2 1	572	0.90	347	3.64	250	2.63
H_2O_2 2	531	0.80	341	4.28	236	2.96
H_2O_2 3	673	0.89	359	4.05	243	2.75
H_2O_2 4	704	0.28	361	13.00	245	8.84
H_2O_2 5	438	0.98	212	2.17	143	1.46
H_2O_2 6	415	0.53	281	5.95	192	4.07
H_2O_2 8	256	0.86	139	1.58	94	1.07
H_2O_2 9	204	0.56	162	5.19	121	3.87

B.1 Bending tests of H_2O_2-beams

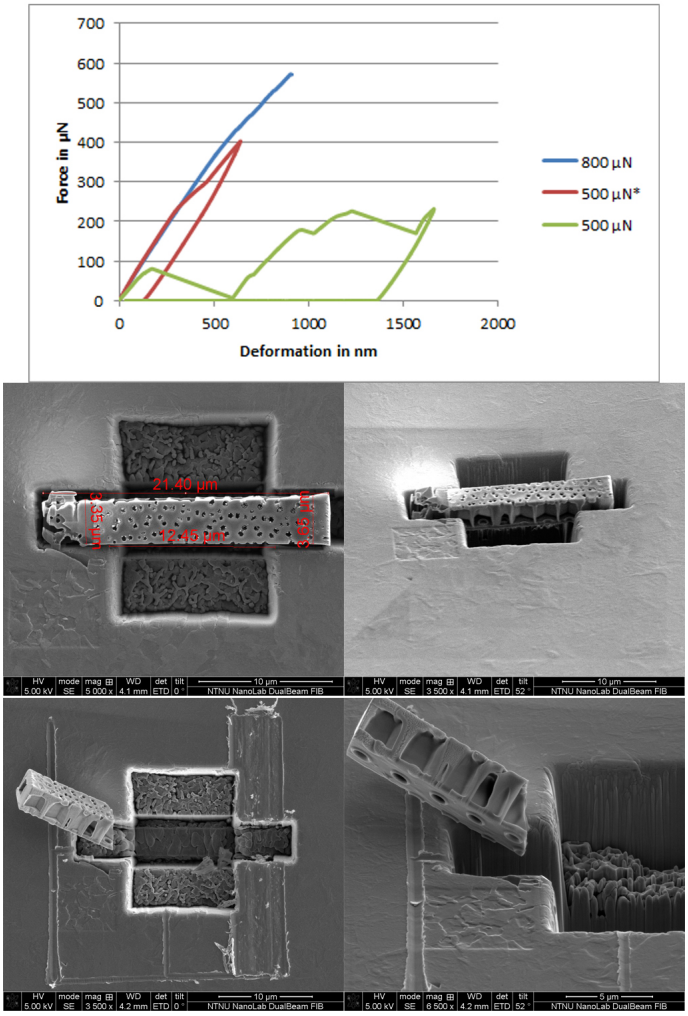

Figure 41: H_2O_2-beam1

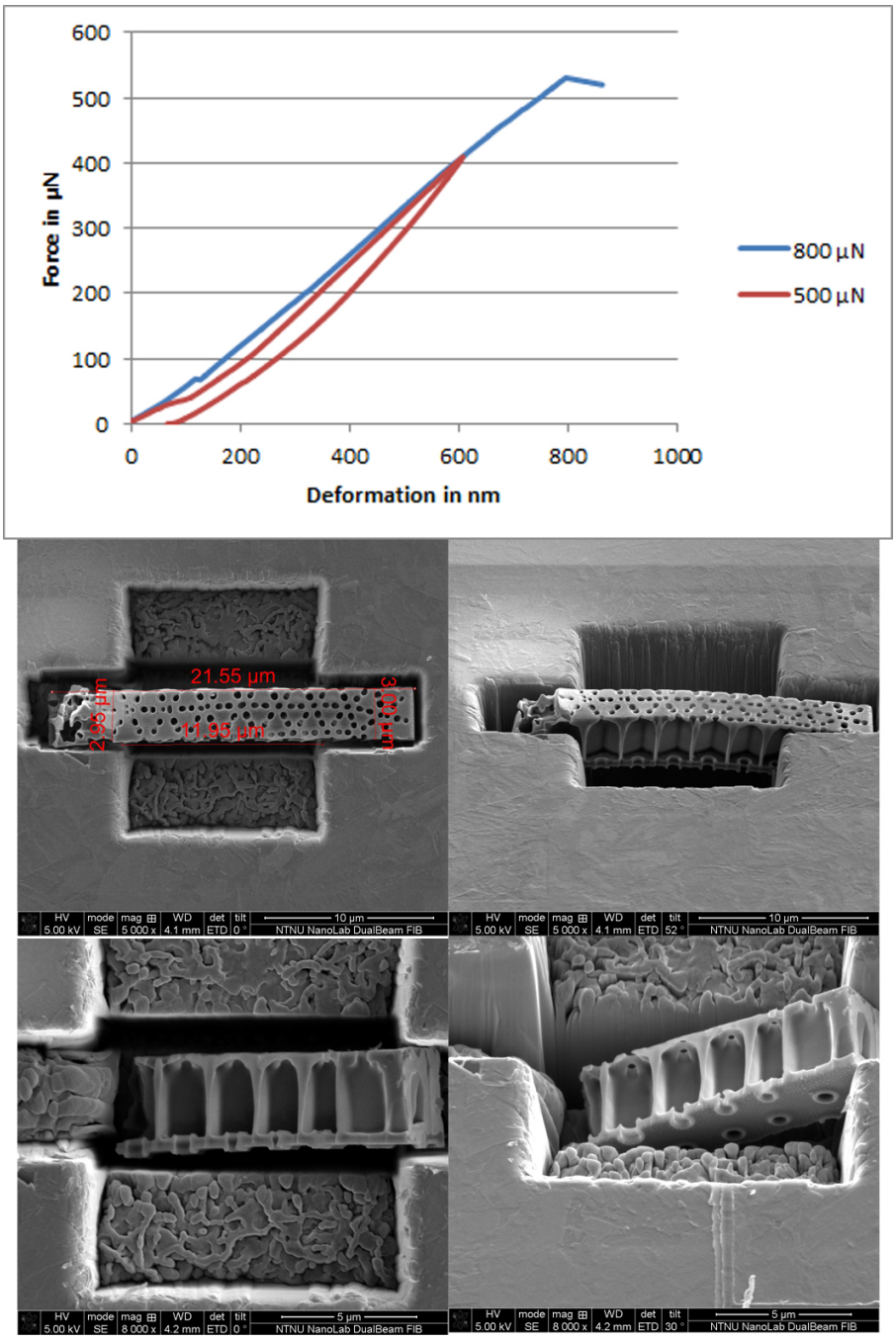

Figure 42: H_2O_2-beam2

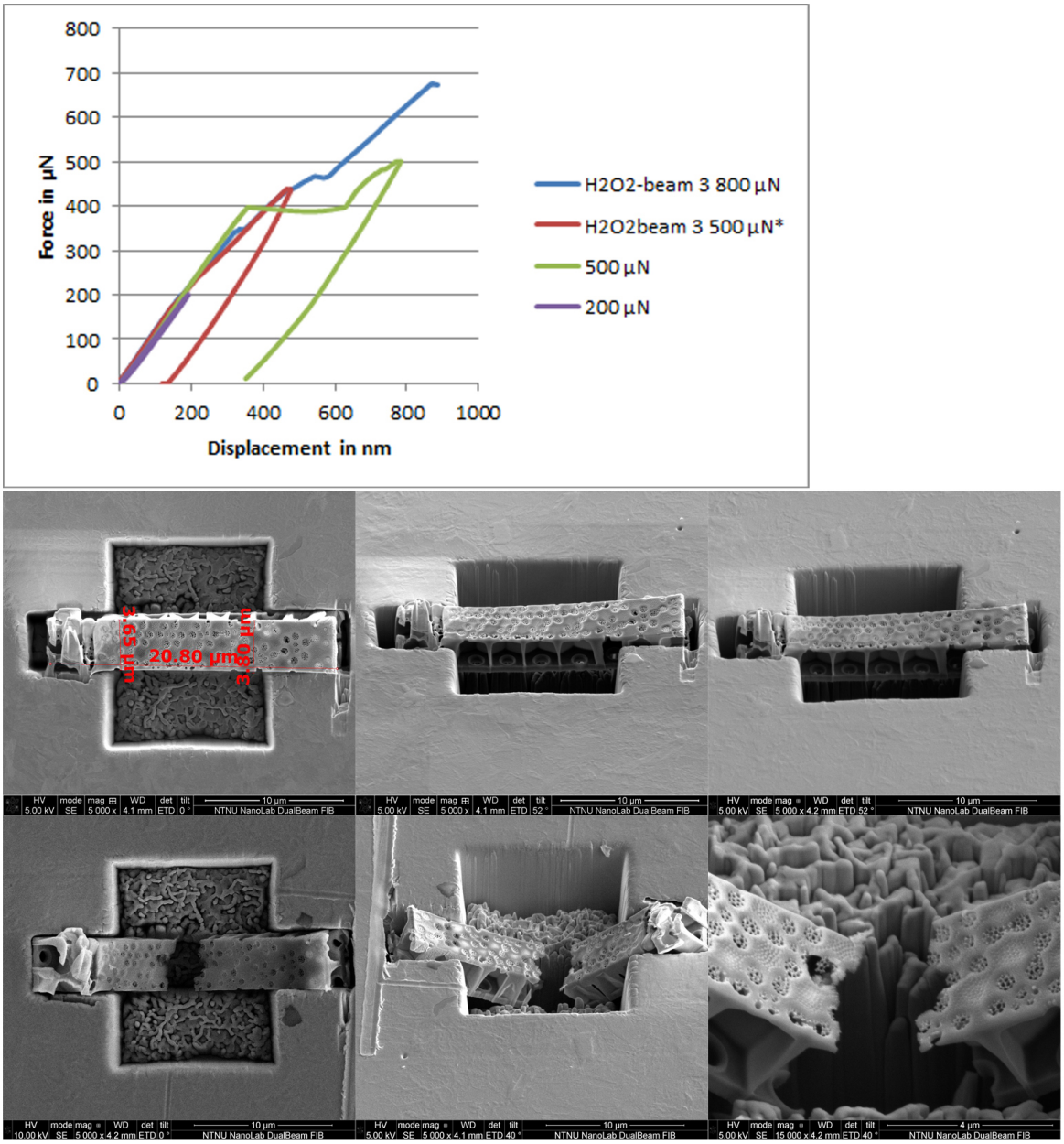

Figure 43: H_2O_2-beam3

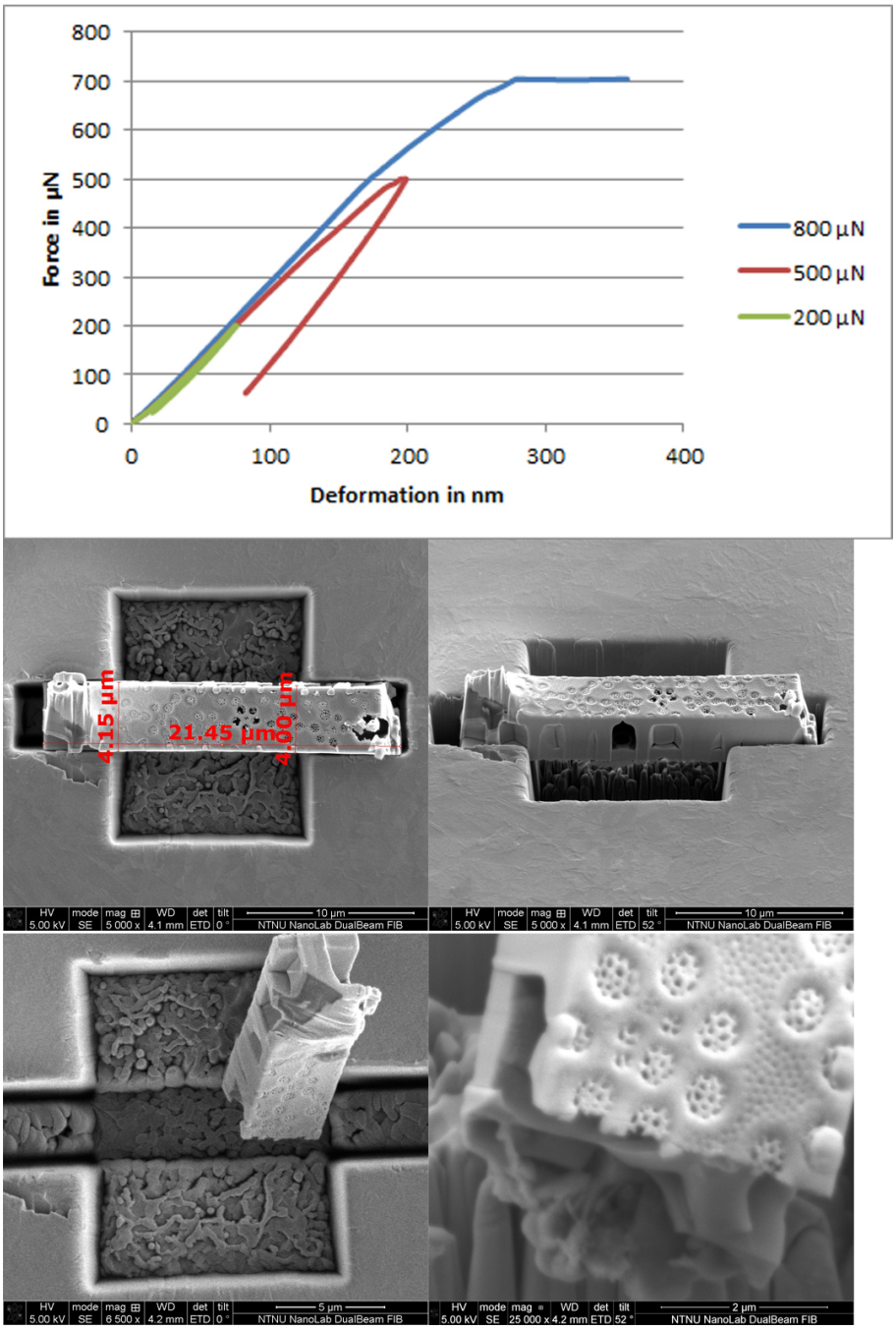

Figure 44: H_2O_2-beam4

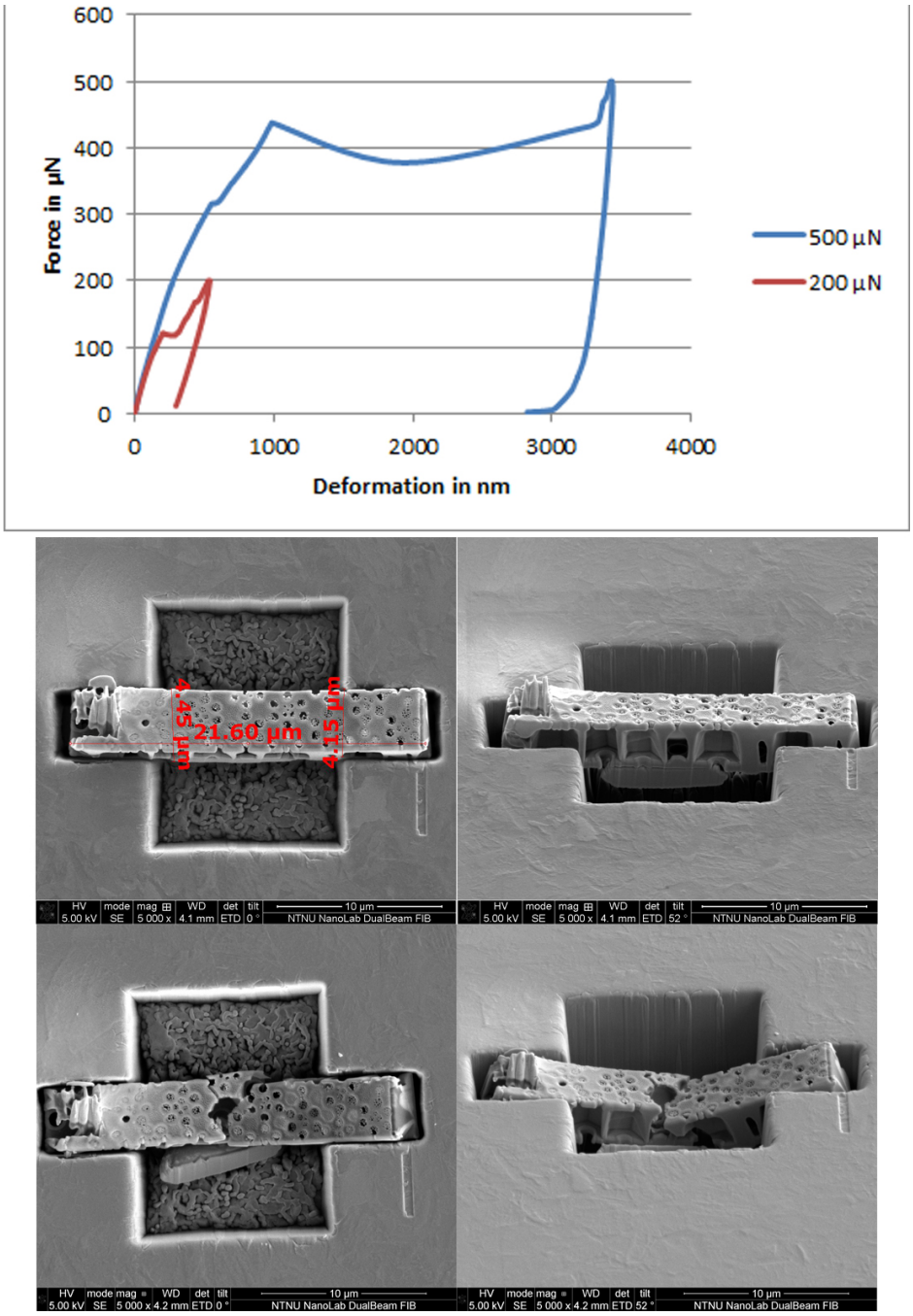

Figure 45: H_2O_2-beam5

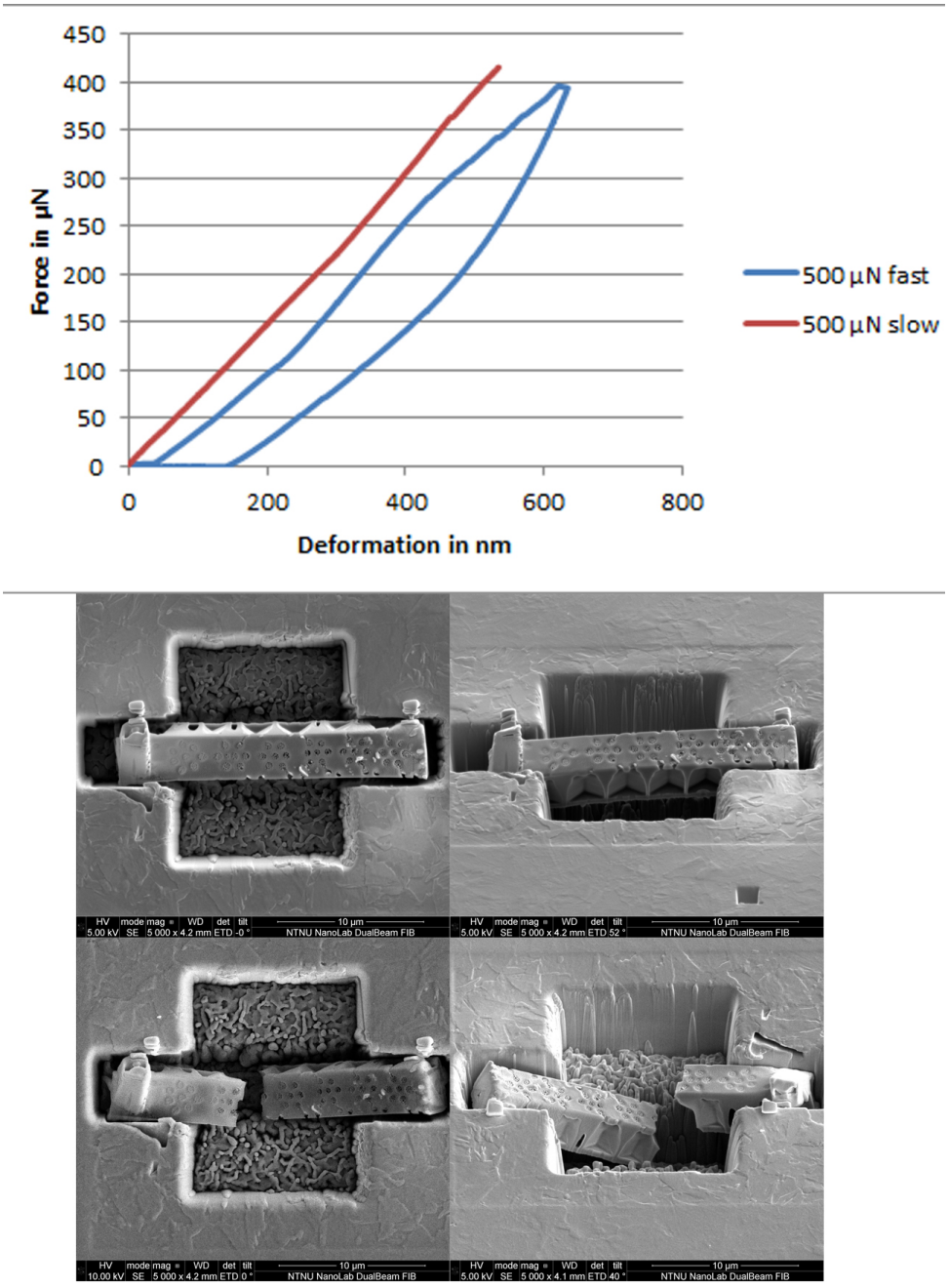

Figure 46: H_2O_2-beam6

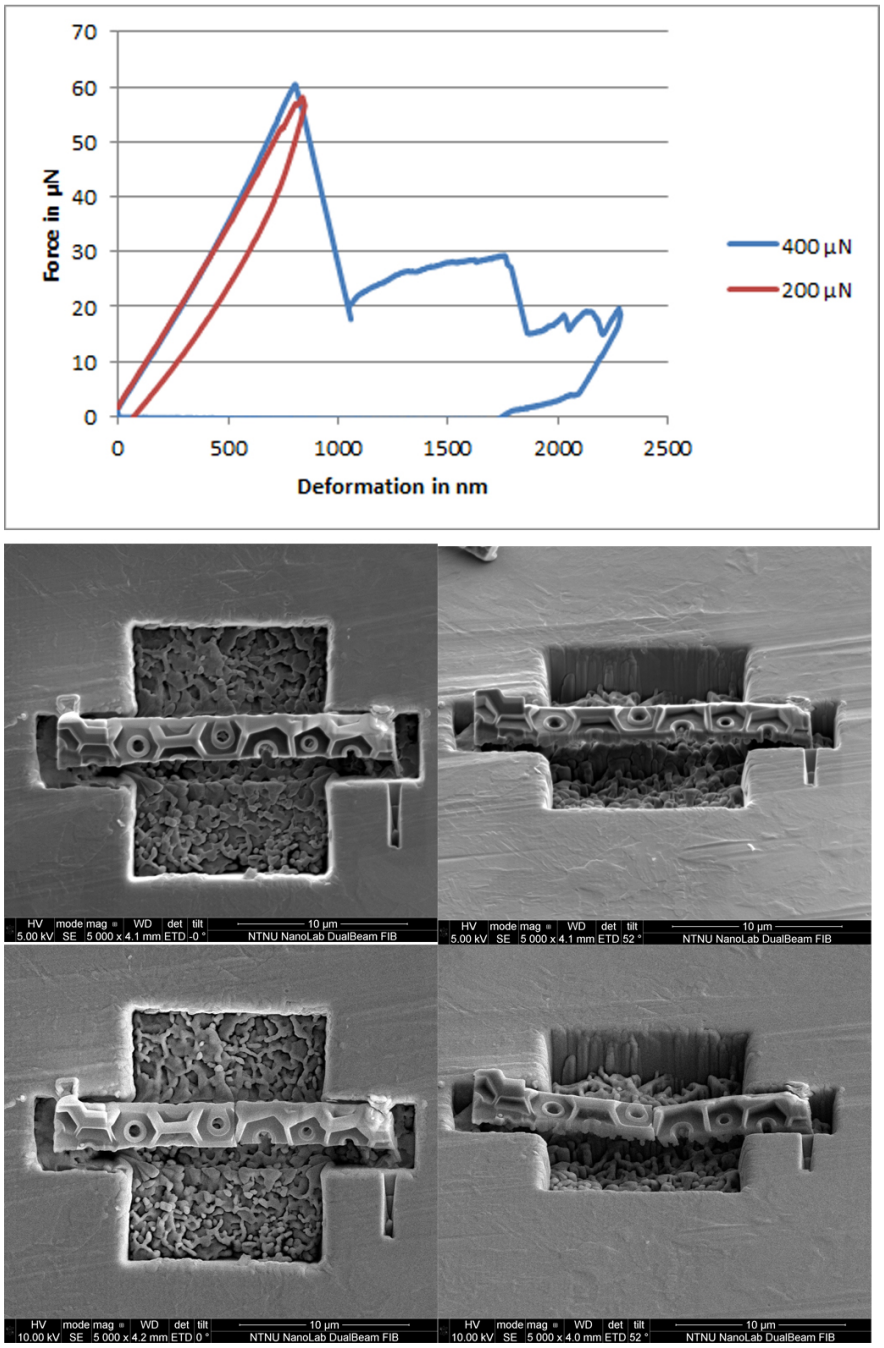

Figure 47: H_2O_2-beam7

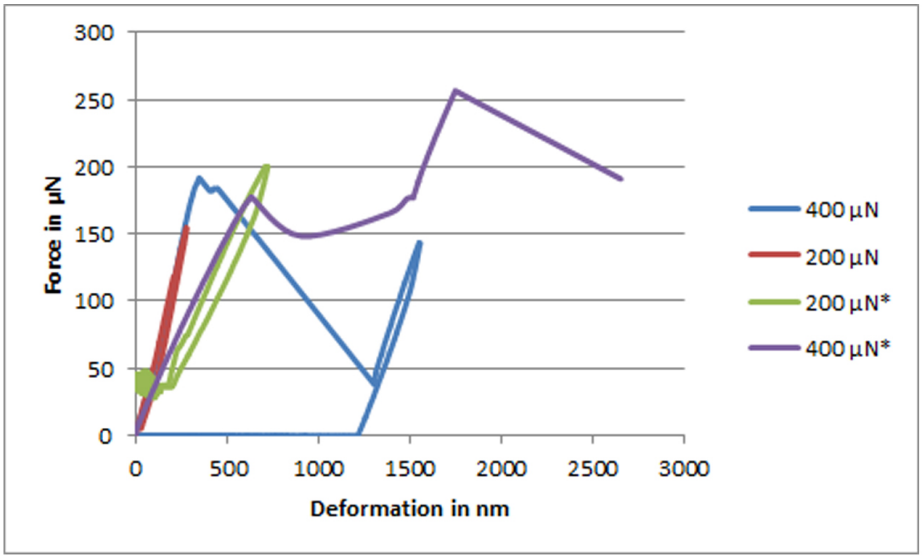

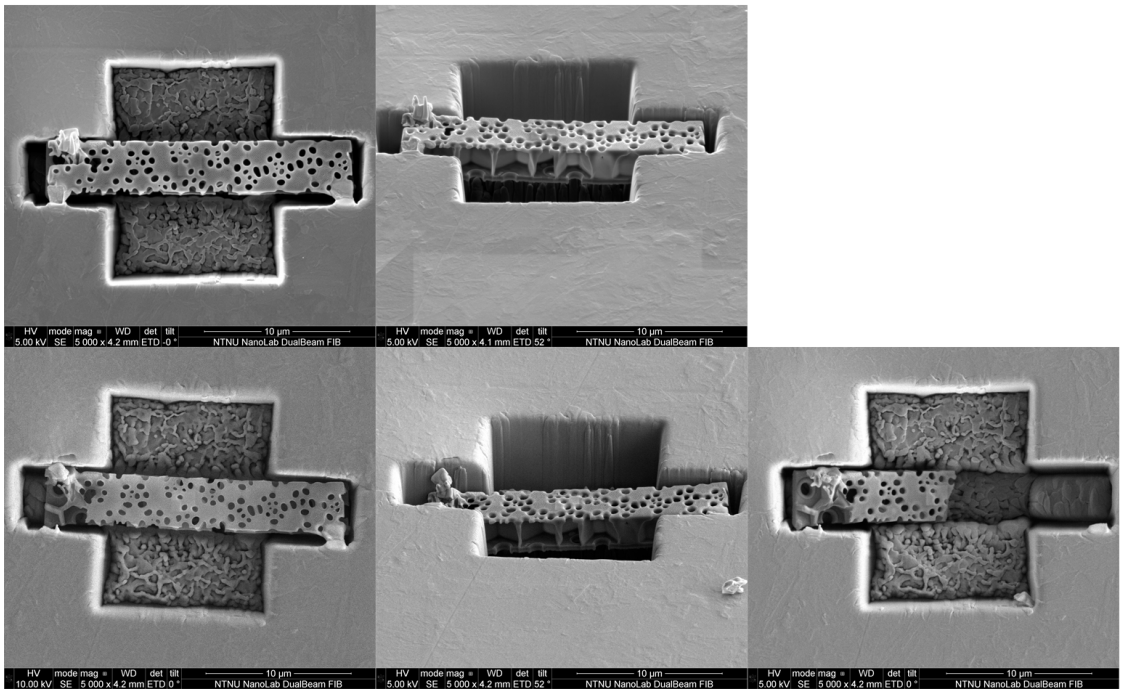

Figure 48: H_2O_2-beam8

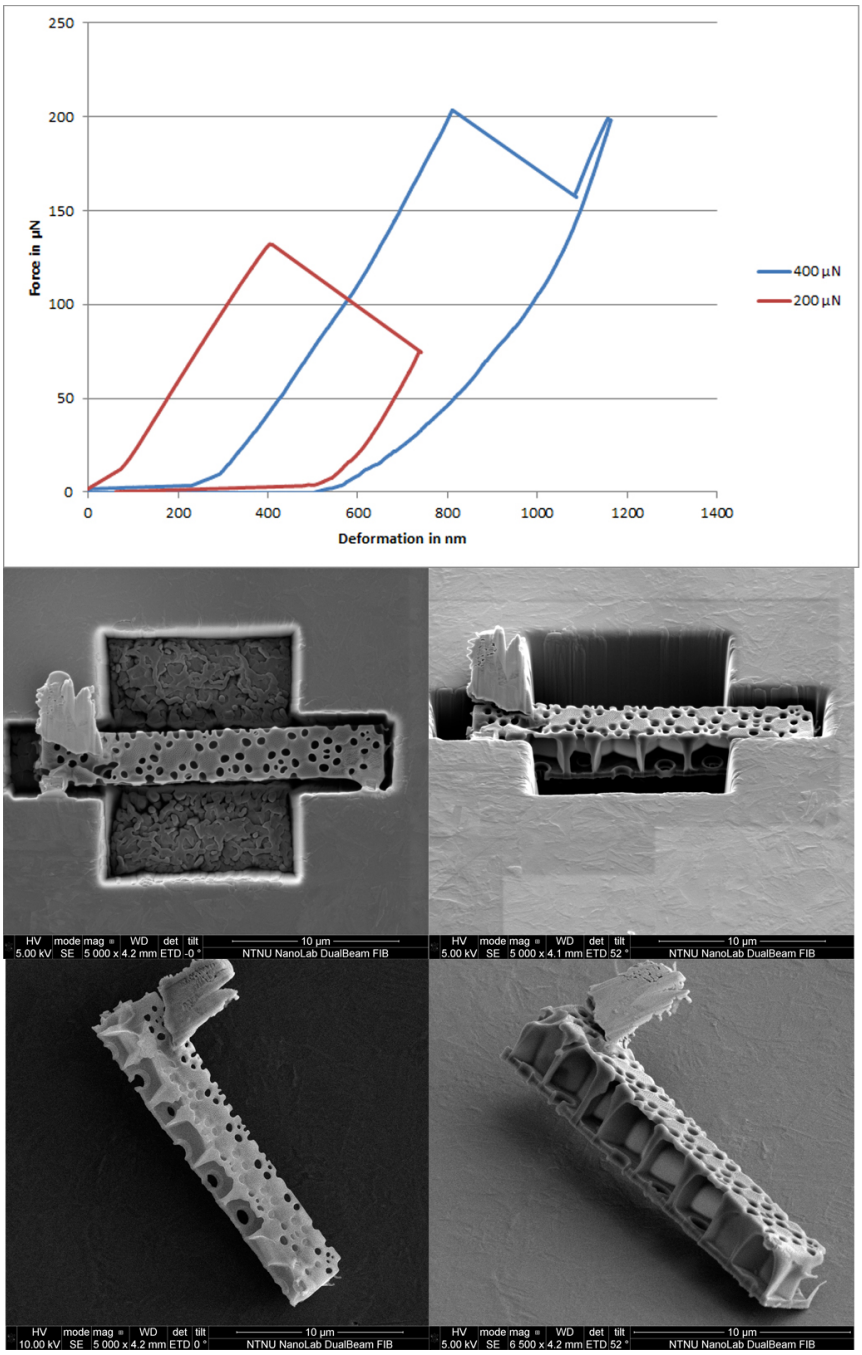

Figure 49: H_2O_2-beam9

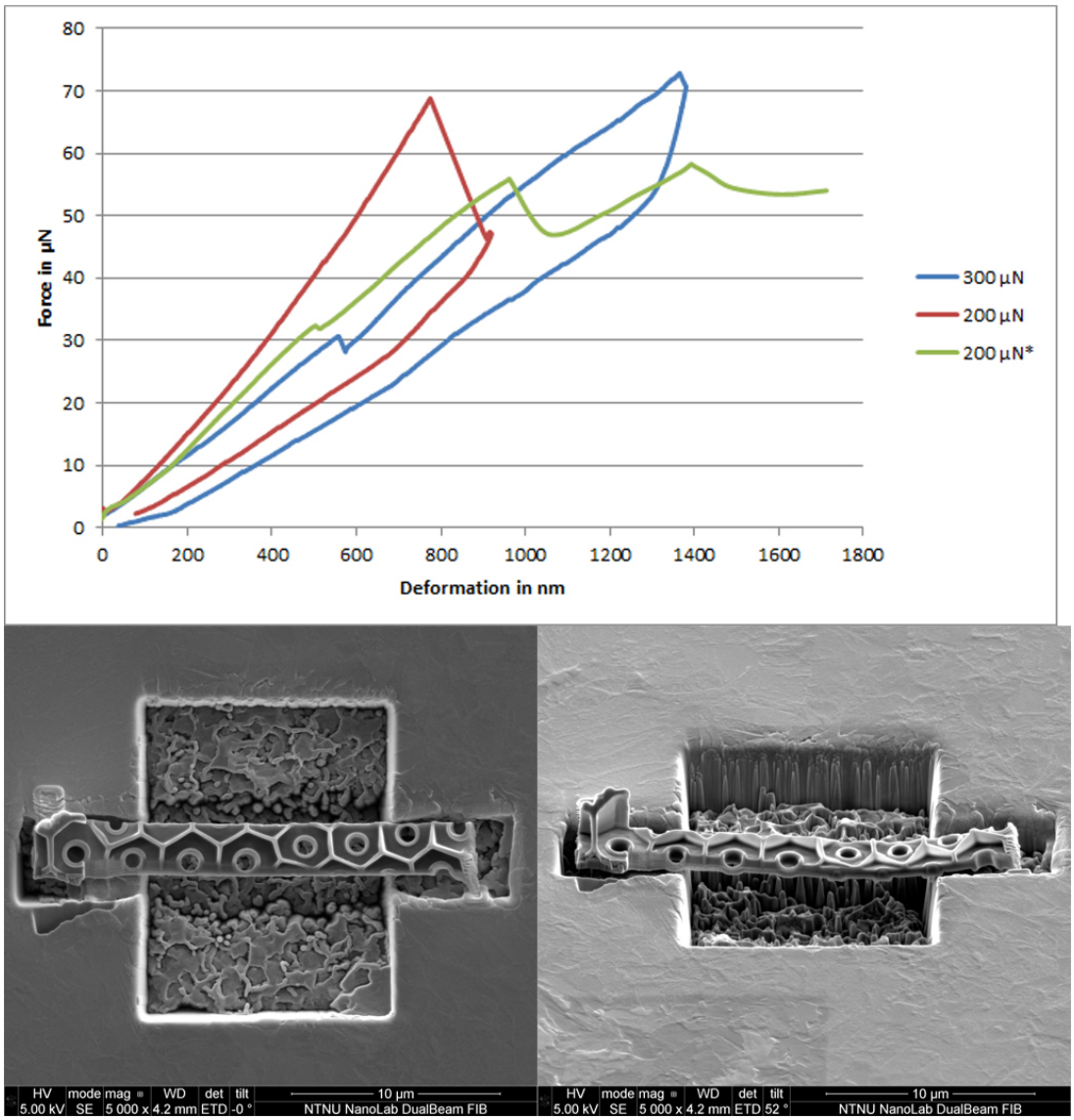

Figure 50: H_2O_2-beam10

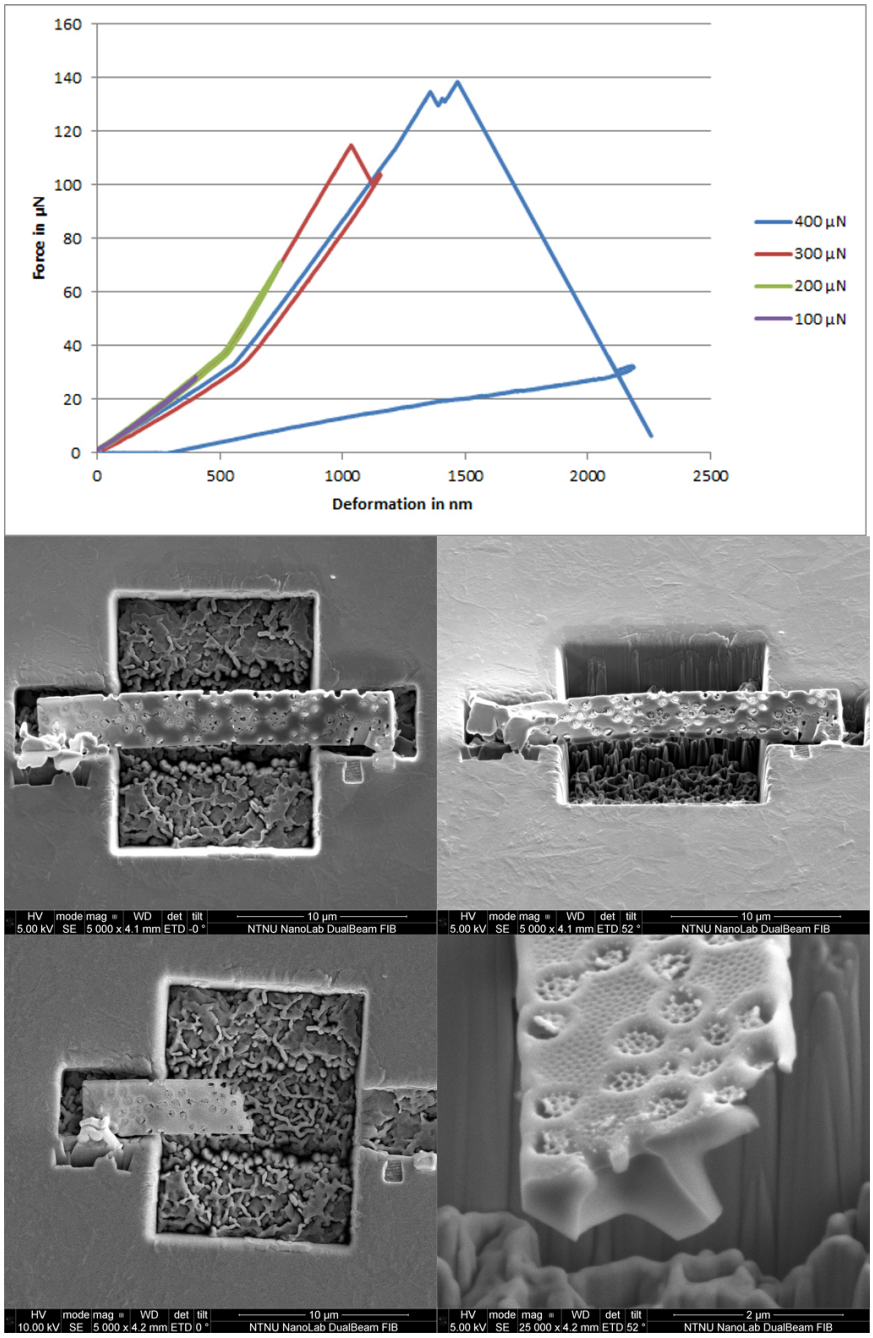

Figure 51: H_2O_2-beam11

B.2 Bending tests of SDS-beams

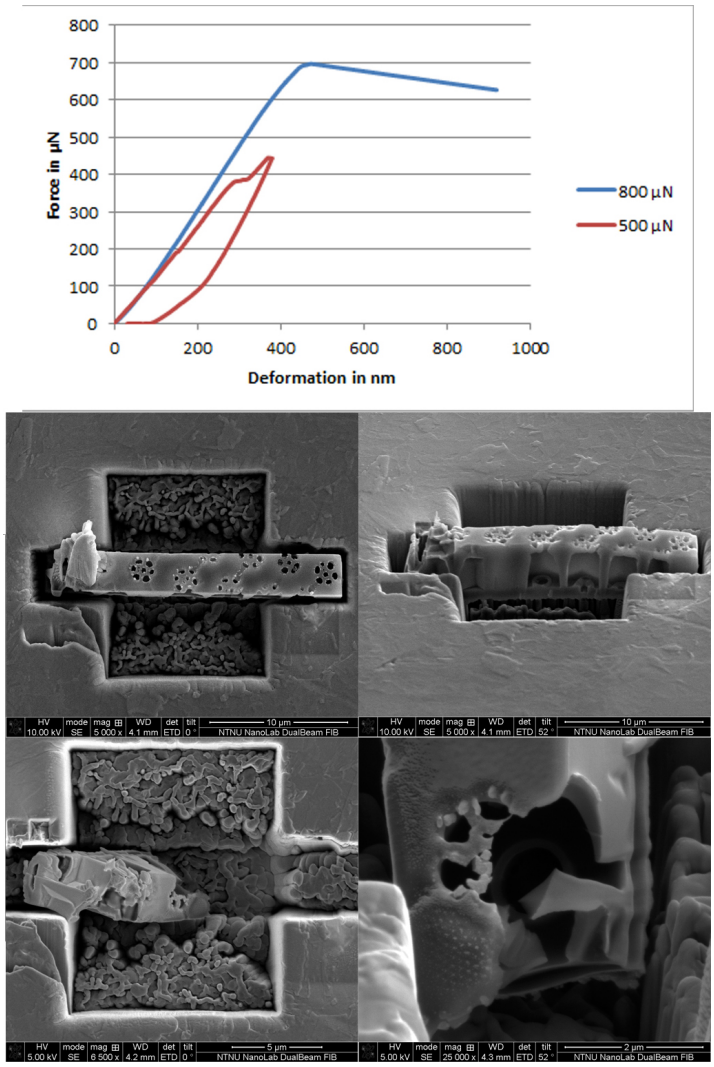

Figure 52: SDS-beam1

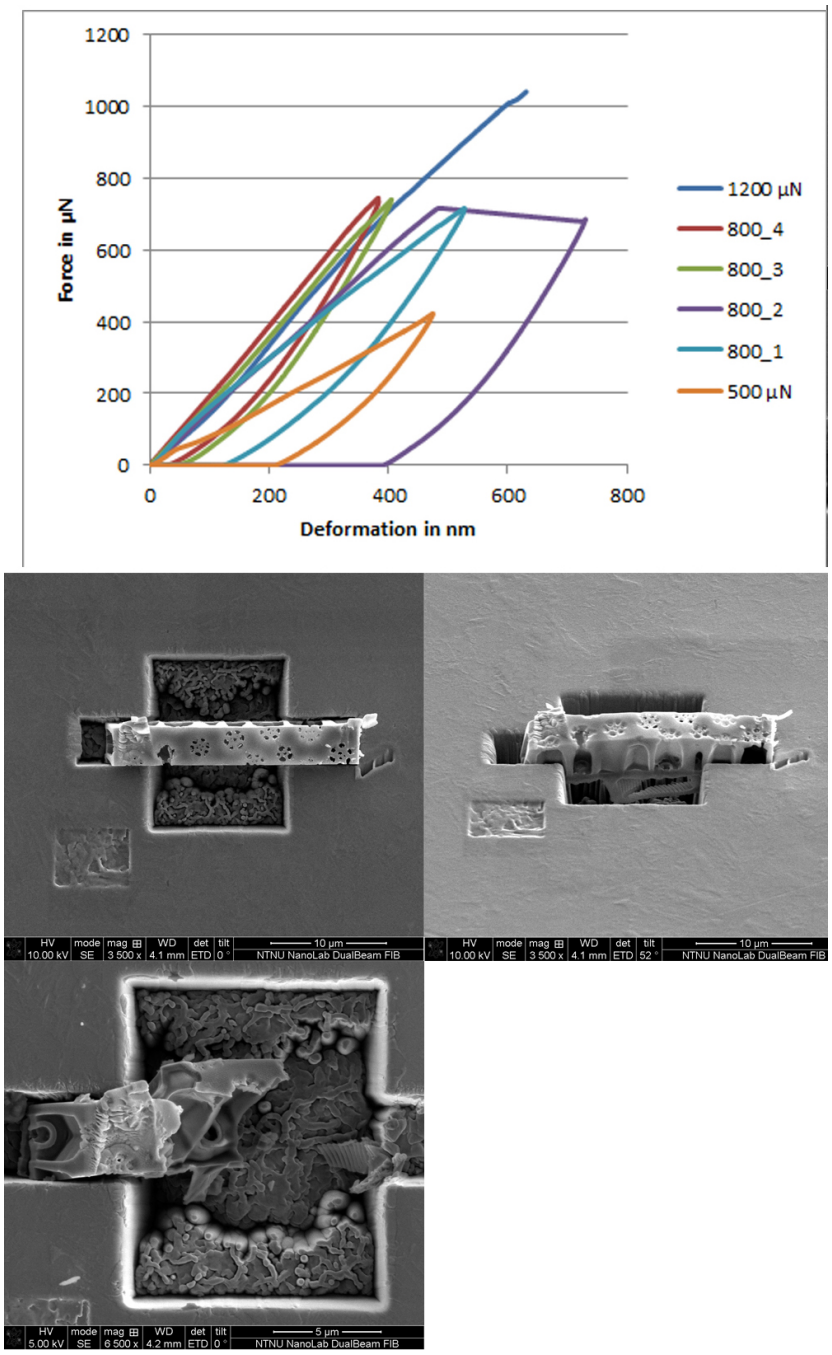

Figure 53: SDS-beam2

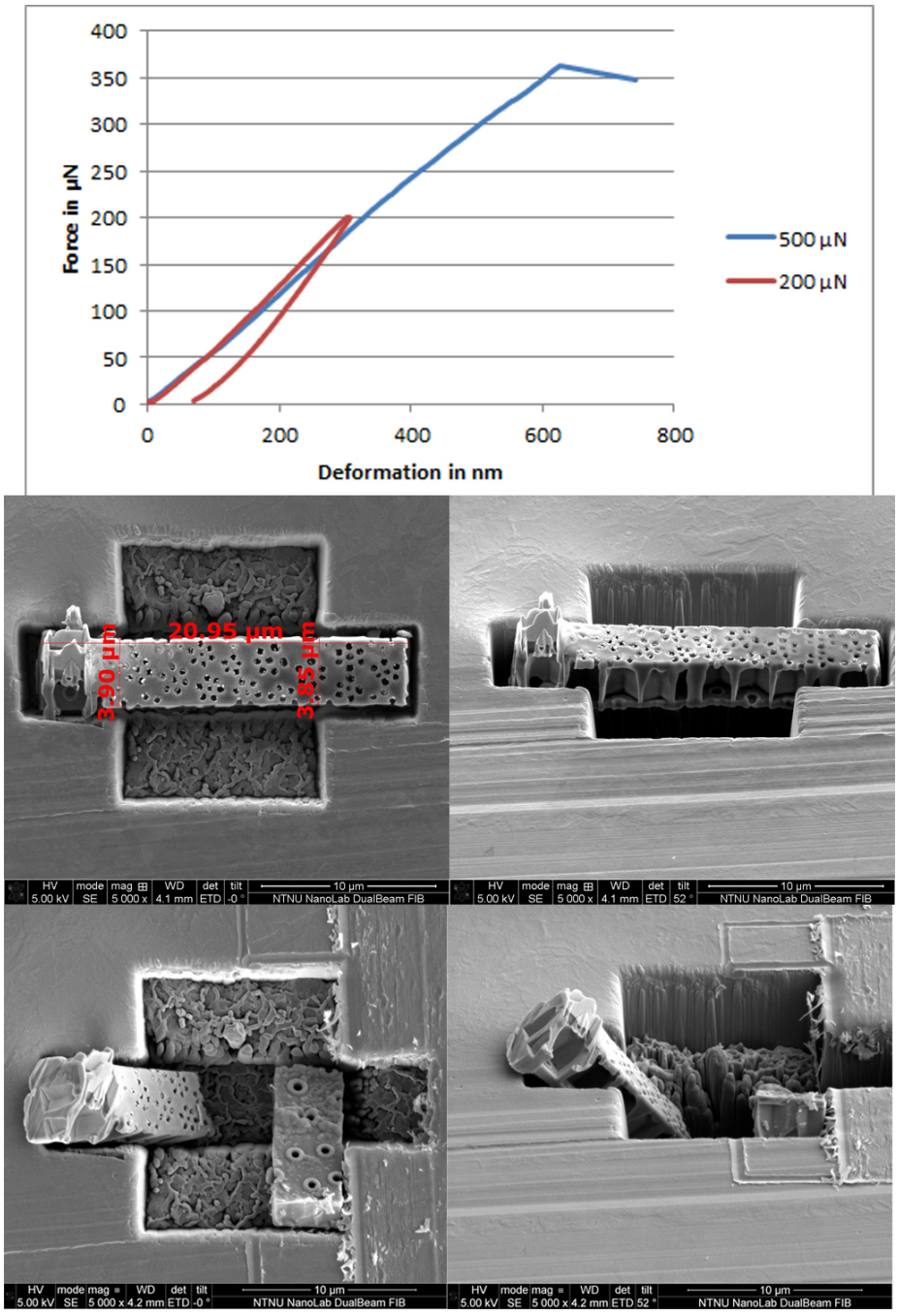

Figure 54: SDS-beam5

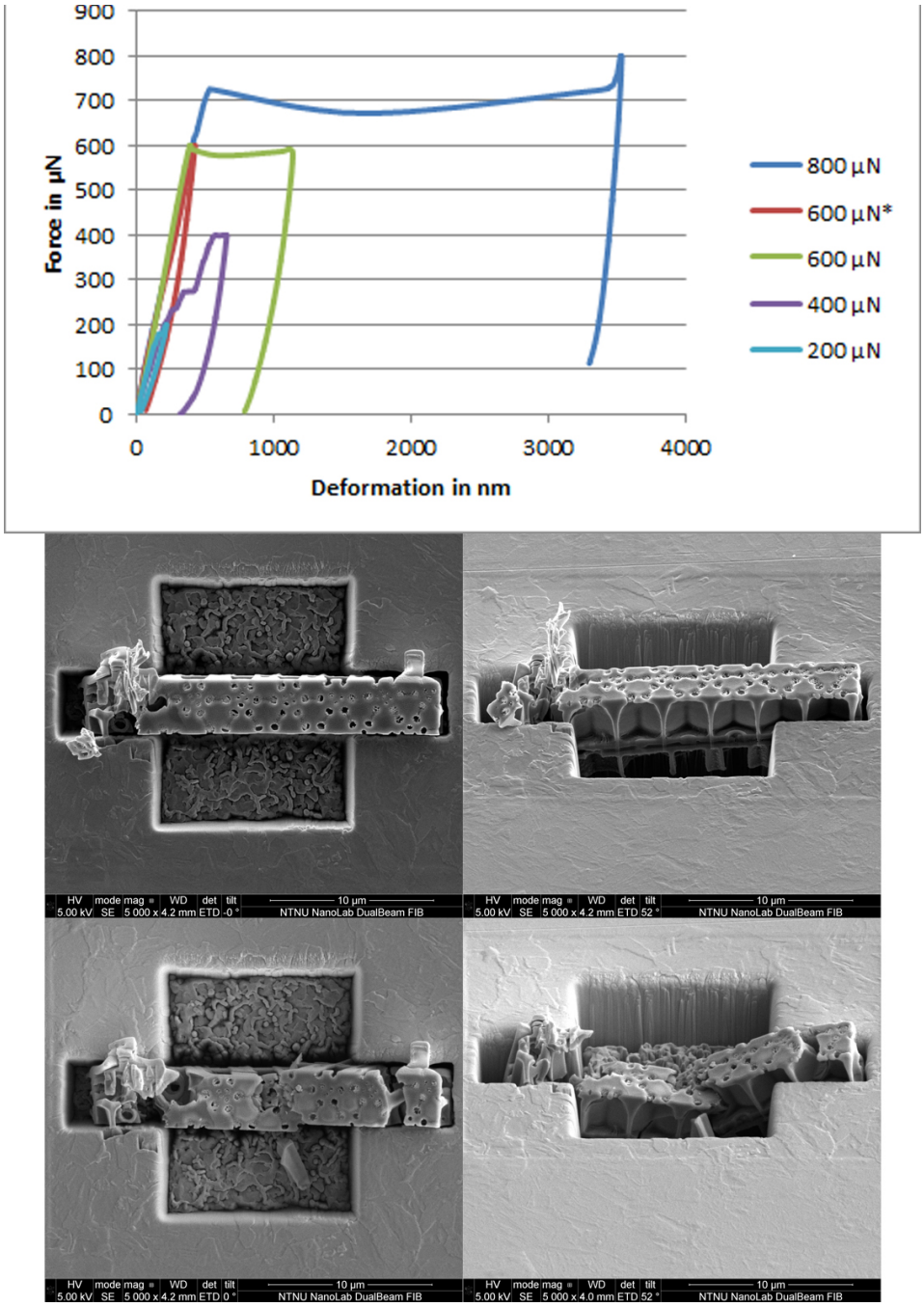

Figure 55: SDS-beam6

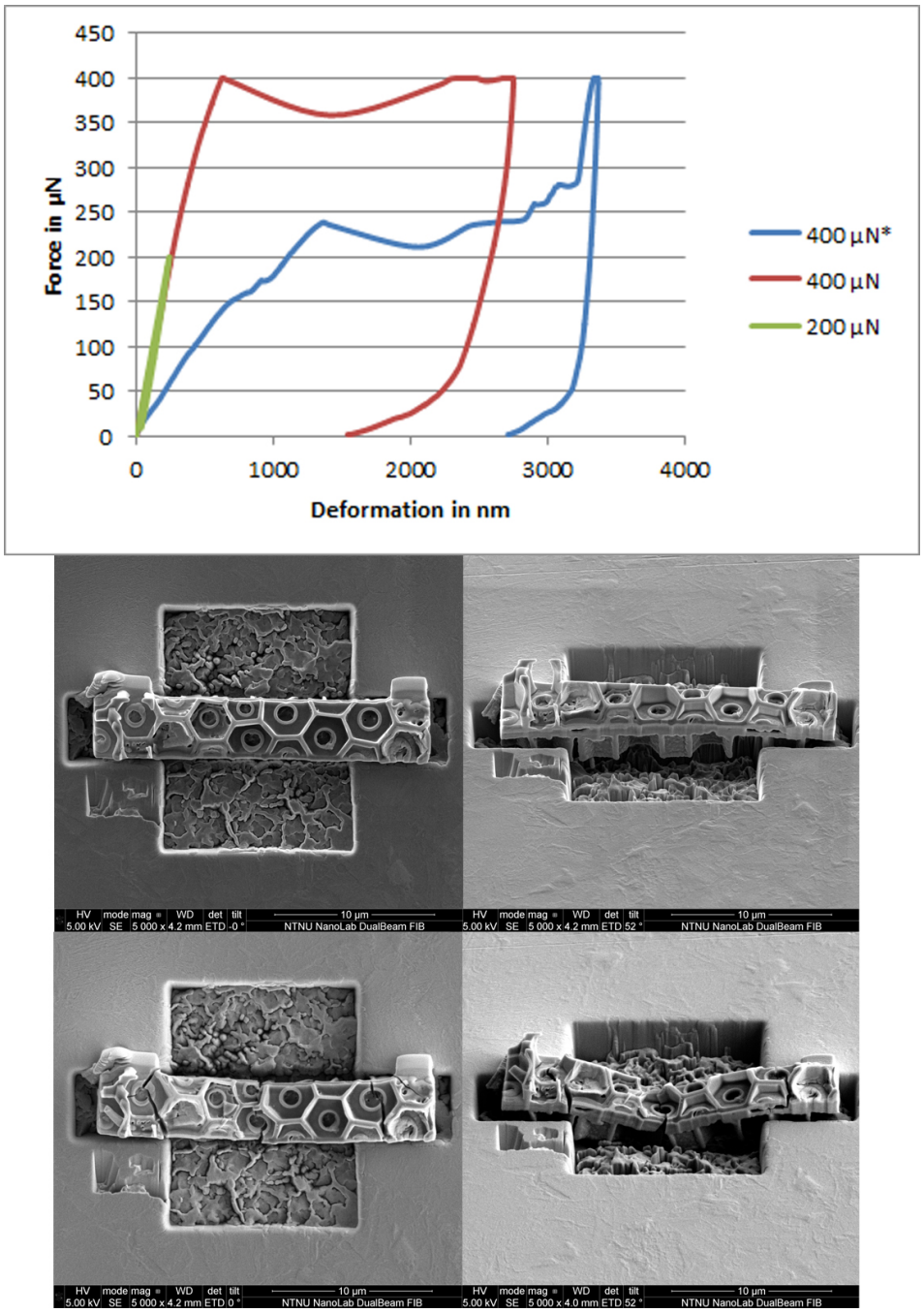

Figure 56: SDS-beam7

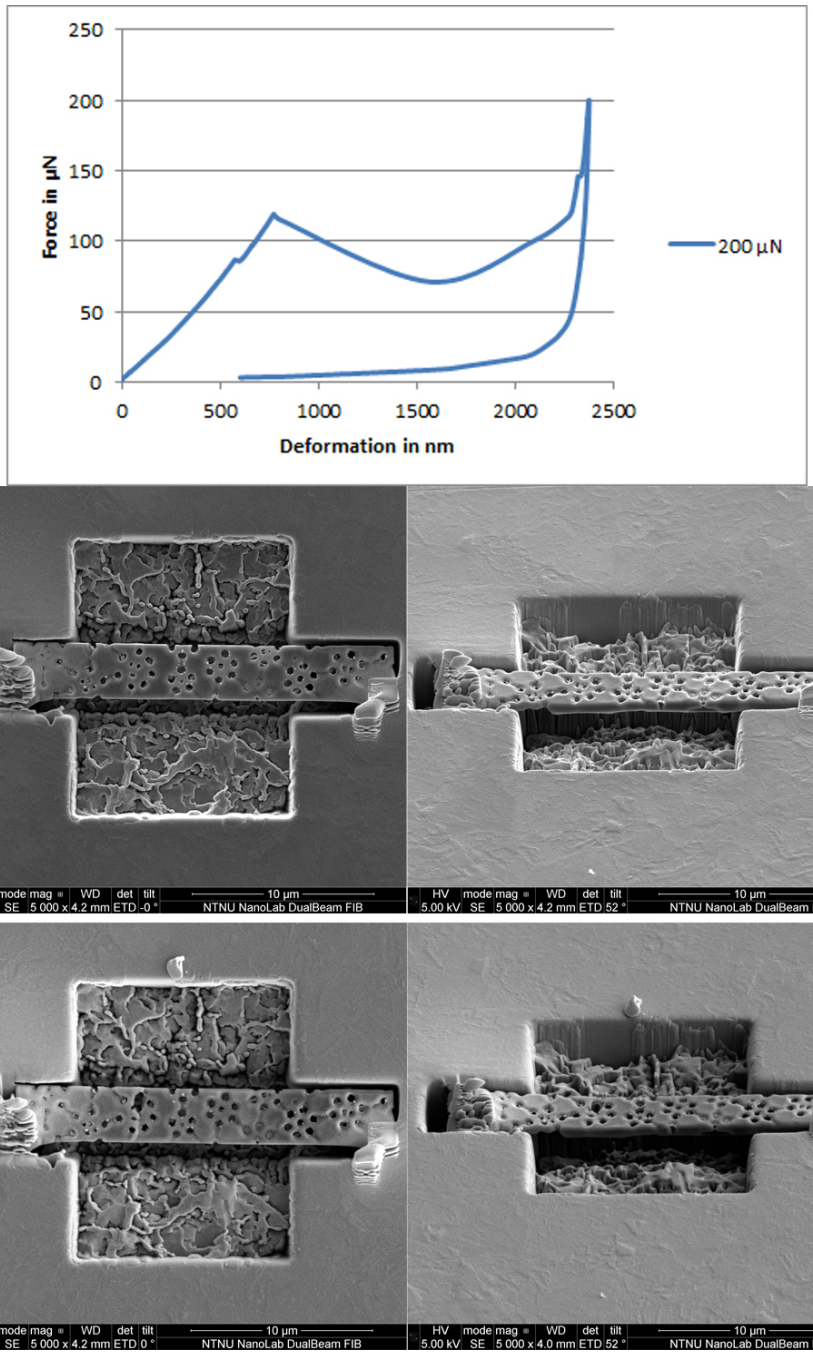

Figure 57: SDS-beam8

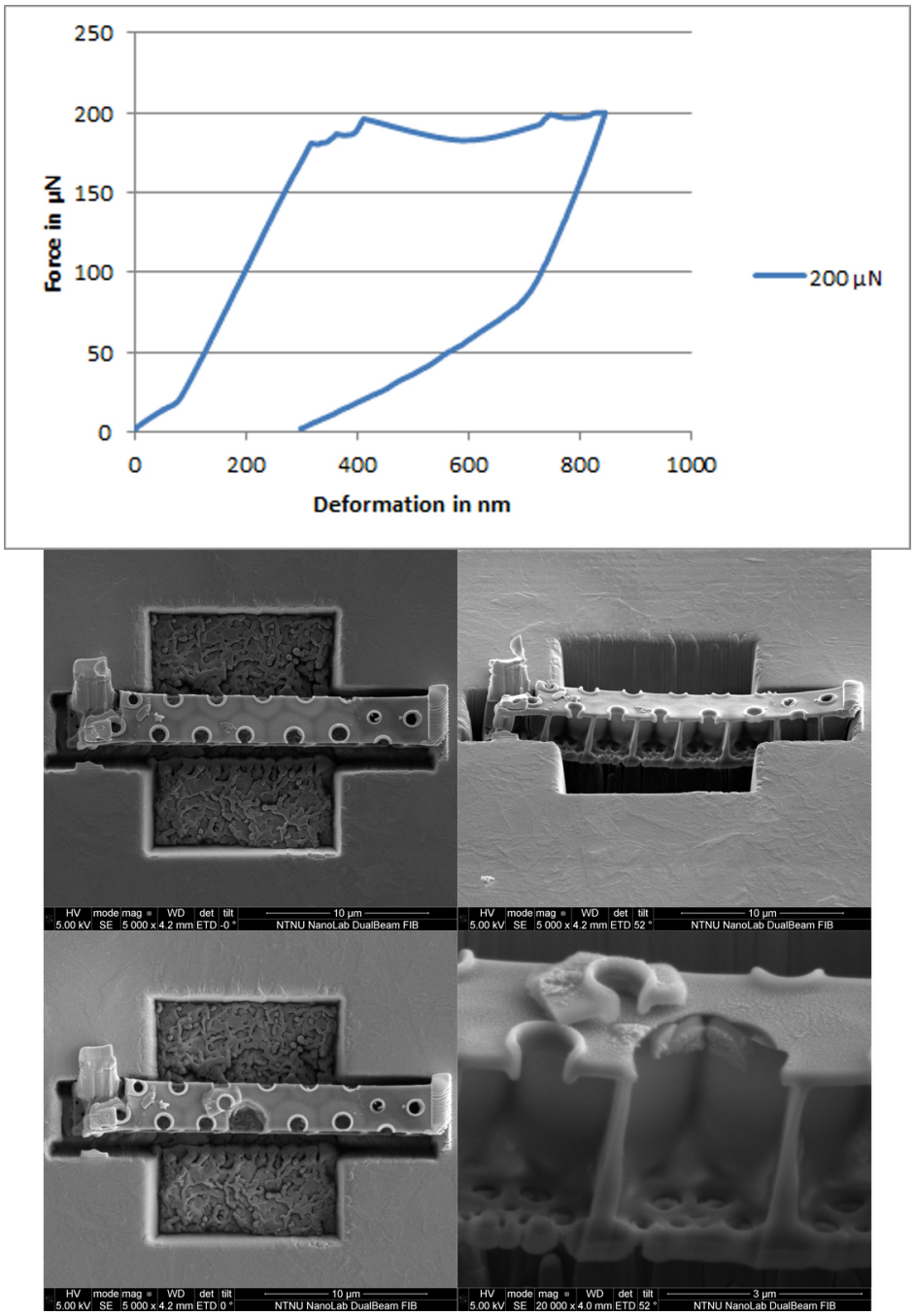

Figure 58: SDS-beam9

Hilde

DELTIOSSJOBB

Isolation and Bulk Metal Analysis of Frustule Biosilica.
Intact biosilica frustules of Pinnularia sp. cells were isolated by treatment with sodium dodecyl sulfate (SDS, JT Baker L050-07) and ethylene diamine tetraacetic acid (EDTA), as originally described by Schmid and Schulz,40 with modifications detailed below. Treatment of diatom cells with the detergent SDS separated organic cell matter from the frustule biosilica but did not remove the girdle band proteins, and so the upper and lower theca of the frustule remained attached. The EDTA removed calcium and other divalent salts from the seawater medium that adsorbed onto the frustule surface.

Duplicate 250 mL aliquots of culture suspension were centrifuged at 2500g for 20 min. The pellet was resuspended in 40 mL of distilled/deionized water, centrifuged, and washed again two more times. The washed diatom cell pellet was resuspended in 40 mL of 50 g/L SDS in 100 mM EDTA, vortexed for 1 min, and then allowed to react for 20 min at room temperature without mixing. The liquid in the suspension turned green. The SDS/EDTA treatment was repeated two more times. The treated cell mass was washed three times in distilled/deionized water to remove the SDS/EDTA and residual intracellular metal oxides, and then three times in methanol to dissolve the residual organic matter (40 mL, 2500g for 20 min). The final isolated frustules were resuspended in 5 mL of MeOH and stored at -20°C.

The silicon and titanium content in the isolated frustule solid was determined by ICP-ES as described above. The titanium content was expressed as g of Ti/100 g of SiO2, assuming that the Si in the frustule was in the form of SiO2. Isolation of diatom biosilica by aqueous hydrogen peroxide treatment of diatom cells was previously described.[30]

4t 40 min
= 5 t centrifuging

COOK BOOK: (scaled down to 25 ml culture volume)

1. Centrifuge duplicate 25 mL culture at 2500g for 20 min. 20
2. Resuspend pellet in 4.0 mL MilliQ water and centrifuge 20
3. Resuspend pellet in 4.0 mL MilliQ water and centrifuge 20
4. Resuspend pellet in 4.0 mL of 50 g/L SDS in 100 mM EDTA
5. Vortex for 1 min, and then allowed to react for 20 min at room temperature without mixing. The liquid in the suspension turned green. 20
6. Sentrifuge and repeat the SDS/EDTA treatment Twice times 20+20+20+20
7. Centrifuge and wash cell mass in MilliQ water three times 20
8. . 20
9. . 20
10. Centrifuge and wash cell mass in methanol three times (4.0 mL, 2500g for 20 min) 20
11. . 20
12. . 20
13. Resuspend in 1 mL of MeOH and store at -20°C.

Reference:
Metabolic Insertion of Nanostructured TiO2 into the Patterned Biosilica of the Diatom Pinnularia sp. by a Two-Stage Bioreactor Cultivation Process
Clayton Jeffryes, Timothy Gutu, Jun Jiao, and Gregory L. Rorrer
ACS Nano, 2008, 2 (10), 2103-2112
DOI: 10.1021/nn800470x • Publication Date (Web): 02 October 2008